Investigation of macroscopic nearcritical fluid phenomena by applying laser–induced thermal acoustics

A thesis accepted by the Faculty of Aerospace Engineering and Geodesy
of the University of Stuttgart and the Stuttgart Center for Simulation
Science in partial fulfilment of the requirements for the degree of
Doctor of Engineering Sciences (Dr.-Ing.)

by

Christoph Steinhausen, M. Sc.

born in Darmstadt

Main referee:	Prof. Dr.-Ing. habil. Bernhard Weigand
Co-referee:	Dr.-Ing. Grazia Lamanna
Co-referee:	Prof. Dr. rer. nat. habil. Andreas Dreizler
Date of defence:	December 2, 2022

Institute of Aerospace Thermodynamics
University of Stuttgart
2023

To my parents and my grandparents
Isolde & Lothar and Ingrid & Willibrord

Acknowledgements

This thesis originated from my work as a research associate at the Institute of Aerospace Thermodynamics (ITLR) at the University of Stuttgart. The research project has been conducted in the framework of the Collaborative Research Centre Transregio 75 (SFB-TRR 75) “Droplet Dynamics Under Extreme Ambient Conditions”, which is funded by the the Deutsche Forschungsgemeinschaft (DFG, German Research Foundation)—Project number 84292822.

First, I would like to express my sincere gratitude to Prof. Dr.-Ing. habil. Bernard Weigand for the opportunity to work on this exciting and challenging project. I benefited greatly from his support, professional advice and the positive working atmosphere at the ITLR. Furthermore, I would like to thank Prof. Dr. rer. nat. habil. Andreas Dreizler for the prosperous cooperation within our joint project, the many discussions, and the valuable advice. I would also like to thank Prof. Dr.-Ing. Joachim Groß for his co-advisory in the scope of the graduate academy “SimTech” and the interesting discussions. Moreover, I would like to give my most sincere gratitude to my supervisor Dr.-Ing. Grazia Lamanna. Thank you for your unvarying support, our countless scientific discussions, and the opportunity to work with you on the research project. At last, I would like to thank my project partner Andreas Preusche for the excellent cooperation, the joint measurement sessions, and our many discussions.

My experimental work has been depending on the support given by the workshops of the ITLR. I would like to thank my colleges of the electrical workshop Uli Schwaderer and Thomas Bertnik for their dedication. Their expertise in fixing seemingly any electrical equipment at a moments notice has been vital for my research. For the same commitment, I would like to express my gratitude to the members of the mechanical workshop. Particularly, I would like to thank Dennis Nehring, Christian Otto, Jürgen Fauser, Attila Lomlu, and Olaf Ordner for their excellent work in building my experimental test rigs. I also would like to mention the support of my student assistants during long measurement campaigns. I would like to thank Anton Schaumäker, Moritz Stein, Patick Palmetshofer, and Shoma Kaiser in particular for their support regarding the set up and characterisation of the experimental and optical facilities. A special thanks goes to Birgid Panzer, Susanne Stegmeier, and Jasmina Radoncic from the administrative staff of the ITLR for their support, patience and the insights into accounting and bureaucracy in general.

In the more than six years I have been working at the ITLR many colleagues have become friends. I would like to thank everyone for the interesting conversation, the relaxed atmosphere and the time we enjoyed together. In particular, I would like to express my gratitude to Jonathan Reutzsch with whom I started and assisted the thermodynamic lecture. Thank you for the great start at the ITLR. Moreover, I would like to thank Stefano Ruberto, Martin Reitzle, and Rolf Stierle for our cooperation within the SFB-TRR 75. A special thanks belongs my office colleges Stefan Brack, Matthias Ibach, and Valerie Gerber for our many discussions and the relaxed atmosphere in our offices. Furthermore, I would like to express my gratitude to Valerie Gerber for our ongoing cooperation in the laboratory, the support during the experimental campaigns, and for proofreading this thesis.

Finally, I would like to thank my friends and band mates from the Allmand Chaoten Orchester for sharing my love in music and performing. Our concerts, tours, festivals, and band practices have been a great way to unwind and recharge. My deepest gratitude, however, belongs to my family. Your unconditional support made me who I am today and helped me to achieve all the goals I set for myself over the years. Moreover, I would like to sincerely thank my life partner Annika Möller for her unwavering support, especially during the challenging times of finalising this thesis.

Leinfelden-Echterdingen, December 2022
Christoph Steinhausen

Contents

Appendix

List of Figures

List of Tables

List of Symbols

Latin characters

Symbol	Description	Unit
$\mathcal{A}_{P1,P2}$	complex amplitudes of the acoustic waves	–
$\mathcal{A}_{T}$	complex amplitudes of the thermal grating	–
B	amplitude of harmonic oscillation	–
C	amplitude of harmonic oscillation	–
D_T	thermal diffusivity	$\mathrm{m^2\,s^{-1}}$
E	energy	$\mathrm{kg\,m^2\,s^{-2}}$
$\mathcal{H}_e$	Green's function for opto–acoustic response of the fluid to electrostriction	–
$\mathcal{H}_{e,P_{1,2}}$	Green's function coefficient for opto–acoustic response of the fluid to electrostriction	–
$\mathcal{H}_{e,T}$	Green's function coefficient for opto–acoustic response of the fluid to electrostriction	–
$\mathcal{H}_{\Theta}$	Green's function for opto-acoustic response of the fluid to thermalisation	–
$\mathcal{H}_{\Theta,P_{1,2}}$	Green's function coefficient for opto–acoustic response of the fluid to thermalisation	–
$\mathcal{H}_{\Theta,T}$	Green's function coefficient for opto–acoustic response of the fluid to thermalisation	–

Symbol	Description	Unit
$\mathcal{H}_{\Theta,D}$	Green's function coefficient for opto–acoustic response of the fluid to thermalisation	–
I	signal intensity	–
M	molar mass	$\mathrm{kg\,mol^{-1}}$
P	power	$\mathrm{kg\,m^{2}\,s^{-3}}$
$\mathcal{P}_{1,2}$	complex parameter to compute $\Psi\,(t)$	–
$\boldsymbol{Q}$	orthogonal matrix of $\boldsymbol{QR}$ decomposition	–
$\boldsymbol{R}$	upper triangular matrix of $\boldsymbol{QR}$ decomposition	–
R	specific gas constant	$\mathrm{m^{2}\,s^{-2}\,K^{-1}}$
S_{xx}	power spectral density	–
$\mathcal{T}$	complex parameter to compute $\Psi\,(t)$	–
T	temperature	K
$\mathcal{U}_{eP}$	dimensionless modulation depth of electrostriction grating	–
$\mathcal{U}_{\Theta}$	dimensionless modulation depth of thermalisation grating	–
X	mole fraction of a fluid in a mixture	–
Y	mass fraction of a fluid in a mixture	–
b	order of Bragg–diffraction	–
c	specific heat capacity	$\mathrm{m^{2}\,s^{-2}\,K^{-1}}$
c_p	specific isobaric heat capacity	$\mathrm{m^{2}\,s^{-2}\,K^{-1}}$
c_v	specific isochoric heat capacity	$\mathrm{m^{2}\,s^{-2}\,K^{-1}}$
c_s	speed of sound	$\mathrm{m\,s^{-1}}$
d	diameter	m
f	focal length	m
$\boldsymbol{g}$	gravitational acceleration	$\mathrm{m\,s^{-2}}$
$h_{y,z}$	dimension of half–minor axis in y and z–direction of optical interference pattern	m
j	indicator related to fluid behaviour; $j = 1$: resonant; $j = 2$: non–resonant	–
k	thermal conductivity	$\mathrm{kg\,m\,s^{-3}\,K^{-1}}$
$\boldsymbol{k}$	wave vector	$\mathrm{m^{-1}}$
l	dimension of half-major axis in x–direction of optical interference pattern	m
m	mass	kg
n	refractive index	–
p	pressure	$\mathrm{kg\,m^{-1}\,s^{-2}}$
o	number of laser shots used for averaging	–
q	magnitude of the grating vector; $q = 2\pi/\Lambda$	$\mathrm{m^{-1}}$

Symbol	Description	Unit
$\boldsymbol{q}$	grating vector	m^{-1}
r	radius	m
s	specific entropy	$\mathrm{m}^{2}\,\mathrm{s}^{-2}\,\mathrm{K}^{-1}$
t	time	s
t_0	time of laser pulse	s
u,v,w	velocity in x, y, z–direction	$\mathrm{m}\,\mathrm{s}^{-1}$
x,y,z	Cartesian coordinates in space	m

Greek characters

Symbol	Description	Unit
Γ	acoustic damping rate	$\mathrm{m}^{2}\,\mathrm{s}^{-1}$
Γ_c	classical acoustic damping rate; volume viscosities are neglected	$\mathrm{m}^{2}\,\mathrm{s}^{-1}$
ΔI	deviation in signal intensity	–
Δy	beam distance in y–direction in front of lens	m
Δz	distance in z–direction between interrogation and excitation beams in front of lens	m
$\Delta \nu$	Doppler shift of laser light	s^{-1}
Θ	crossing angle of excitation beams	rad
Λ	grid spacing of optical interference pattern	m
Π	ratio of acoustic wave frequency to thermalisation rate	–
Σ_D	complex parameter related to the damping of the creation of the thermal grating	–
$\Sigma_{P_{1,2}}$	complex parameter related to the damping of the acoustic waves	–
Σ_T	complex parameter related to the damping of the thermal grating	–
Φ	crossing angle of interrogation beam	rad
$\Psi\,(t)$	time–dependent dimensionless diffraction efficiency of a LITA signal	–
Ω	dominating beat frequency of the LITA signal	s^{-1}
α_λ	acoustic absorption coefficient per wavelength	–
β_T	isothermal compressibility	$\mathrm{m}\,\mathrm{s}^{2}\,\mathrm{kg}^{-1}$
$\gamma_{n\Theta}$	rate of excited–state energy decay not caused by thermalisation	s^{-1}

Symbol	Description	Unit
γ_{Θ}	rate of excited–state energy decay caused by thermalisation	$\mathrm{s^{-1}}$
ζ,$\bar{\zeta}$	misalignment length scales in z-direction	m
η,$\bar{\eta}$	misalignment length scales in y-direction	m
κ	specific heat ratio	–
λ	wavelength	m
μ_s	dynamic shear viscosity	$\mathrm{kg\,m^{-1}\,s^{-1}}$
μ_v	dynamic volume viscosity	$\mathrm{kg\,m^{-1}\,s^{-1}}$
ν	laser light frequency	$\mathrm{s^{-1}}$
ν_a	frequency of the acoustic wave	$\mathrm{s^{-1}}$
ξ,$\bar{\xi}$	misalignment length scales in x-direction	m
ϖ	relaxation time	s
ϱ	mass density	$\mathrm{kg\,m^{-3}}$
σ	Gaussian half–width of interrogation beam	m
τ	laser pulse length	s
υ	angular frequency	$\mathrm{s^{-1}}$
υ_0	natural angular frequency associated with speed of sound	$\mathrm{s^{-1}}$
χ	dielectric susceptibility	–
ψ	crossing angle of interrogation and excitation beam in x–z plane	rad
ω	Gaussian half–width of excitation beams	m

Subscripts

Symbol	Relation & Description
∞	ambient conditions
0	unfocused beam
$+$	anti–Stokes process
$-$	Stokes process
Ar	fluid argon
D	creation of the thermal grating
DFT	calculations using a direct Fourier transformation
DG	condition in droplet generator
Fit	calculations using a curve fitting
LITA	measurement using laser–induced thermal acoustics
LIFP	measurement using laser–induced fluorescence phosphorescence

Symbol	Relation & Description
P	laser–induced thermal acoustics induced acoustic waves
N_2	fluid nitrogen
NIST	theoretical calculations using NIST database by Lemmon et al. [56]
T	thermal grating
ad	adiabatic
c	properties in the critical point
cal	calibration measurements
ch	condition in measurement chamber
coll	elastic collisions
d	droplet
diff	diffusion
e	electrostriction
exc	excitation beams
f	focal point
inter	internal degrees of freedom
int	interrogation beam
jet	gaseous jet
kn	Knudsen layer
max	maximum
min	minimum
mix	local condition of mixture
$n\Theta$	not related to thermalisation
r	reduced properties scaled with properties at critical point
rot	rotational degrees of freedom
s	saturated condition
sig	signal beam
th	theoretical calculations using data sheet specification
Θ	thermalisation
v	vapour
vibr	vibrational degrees of freedom
win	windowed signal

Superscripts

Symbol	Description
$*$	complex conjugate

Miscellaneous characters

Symbol	Description
$\mathcal{O}$	order of magnitude

Abbreviations

Abbreviation	Description
BE	beam expander
CMOS	complementary metal oxide semiconductor
CP	critical point
cw	continuous wave
D	detector
DAQ	data acquisition
DFG	German Research Foundation
DFT	direct Fourier transformation
DPSS	diode pumped solid state
EoS	equation of state
FIR	finite impulse response
FOV	field of view
FS3D	free surface 3D
GLP	Glan–Laser polarizer
GUM	guide to the expression of uncertainty in measurement
ITLR	Institute of Aerospace Thermodynamics
L	lens
LAR	Least Absolute Residuals
LASER	light amplification by stimulated emission of radiation
LDL	large detector limit
LED	light–emitting diode
LIFP	laser–induced fluorescence phosphorescence
LIGS	laser–induced (transient) grating spectroscopy
LITA	laser–induced thermal acoustics
LV	laser–induced thermal acoustics measurement volume
MM	multi–mode fibre with diameter of 25 µm
NC	non–condensible
Nd:YAG	neodymium–doped yttrium aluminium garnet
NIST	National Institute of Standards and Technology

Abbreviation	Description
PBS	polarising beam splitter
PC–SAFT	perturbed–chain statistical associating fluid theory
SBS	stimulated Brillouin scattering
SDL	small detector limit
SM	single–mode fibre with diameter of 4 µm
STRS	stimulated (thermal) Rayleigh scattering
UV	ultra violet
VDF	velocity distribution function
VLE	vapour–liquid equilibrium
WP	wave–plate

Abstract

The political and social aspiration to reduce greenhouse gases together with increasing energy demands are driving the development of new sustainable energy solutions. To achieve long term sustainability both innovative energy sources and improvements in efficiency are essential. Higher process efficiencies have been achieved by raising combustion pressures, reaching values that now exceed the critical pressures of the injected fuels. However, for an efficient and stable combustion a profound understanding of the processes prior to the combustion, such as fluid injection, disintegration and subsequent evaporation is essential. Unfortunately, the fundamental changes in fluid behaviour at near- to supercritical conditions leading to the observed fluid phenomena are not yet fully understood. Besides fluid injection, supercritical fluids themselves have been identified as an innovative path for an efficient energy conversion and heat transfer processes. The Brayton cycle using supercritical carbon dioxide as operating fluid, supercritical water as coolant and process fluid in nuclear reactors, or the application of supercritical methane as new ’green’ fuel in rocket propulsion are just a few examples.

Laser–induced thermal acoustics (LITA) has been identified as a promising diagnostic tool in near- to supercritical fluid research. The latter is based on the capability to acquire speed of sound data as well as to resolve thermal and acoustic attenuation in both pure fluids and complex mixing processes, such as evaporation and jet disintegration. Moreover, based on the non–linear pressure dependencies, LITA becomes increasingly more effective in high-pressure environments. By analysing the frequency domain of recorded signals, speed of sound data can be directly determined without any equation of state or additional modelling approaches. Furthermore, acoustic damping rates and thermal diffusivities can be acquired by an analytical expression for the temporal–domain of the signals. By combining both evaluations with suitable analytic expressions for the thermodynamic properties, mixing states, such as local mixing temperatures and concentrations, can be determined. Moreover, since in complex fluids at near- to supercritical conditions acoustic damping is related to both sound dispersion and volume viscosity, important insights into the physics of supercritical fluids are provided.

Concordantly, the purpose of this thesis is to apply LITA in the investigation of macroscopic fluid phenomena at nearcritical to supercritical fluid conditions. This includes the following major research objectives. First, the significance of volume viscosities in complex fluids at dense gas conditions as well as the dependency of acoustic damping on mixing states are assessed. Second, the feasibility of time–resolved LITA measurements under complex flow conditions is evaluated. To achieve these objectives an experimental test facility has been designed, which enables investigations at high pressure and high temperature conditions in both pure fluids and complex mixing processes. Moreover, the laser–induced thermal acoustics setup of the ITLR has been optimised for high pressure investigations. Also a new high–speed LITA system with an adjustable measurement volume has been developed. Furthermore, a new post–processing methodology capable of analysing both the frequency and time–domain of the signal has been developed and validated. With the developed system and routines investigations in carbon dioxide, nitrogen, and binary mixtures at gas and gas–like states have been conducted to assess acoustic attenuation and volumes viscosities. Additionally, a jet mixing process has been studied to characterise the LITA arrangement and to evaluate the dependency of acoustic damping on mixing concentration. At last, to assess the feasibility of transient LITA measurements in turbulent, physically complex flow conditions and to further characterise the evaporation process, time–resolved LITA measurements have been performed in the wake of a free falling droplet evaporating in a supercritical atmosphere.

Kurzfassung

Der steigende Primärenergiebedarf steht konträr zu den gesellschaftlichen und politischen Ambitionen einer Reduktion von Treibhausgasemissionen. Dieser aktuell inhärente Widerspruch ist einer der Hauptgründe für die fortschreitende Entwicklung nachhaltiger Ansätze in der Energieversorgung. Neben der Entwicklung neuartiger Technologien, ist die Steigerung der Effizienz von konventioneller und erneuerbarer Energiewandlung unumgänglich. Eine Erhöhung des Prozesswirkungsgerades wird hierbei unter anderem durch eine Steigerung des Verbrennungsdruckes erreicht. Infolgedessen überschreiten die Verbrennungsdrücke mittlerweile die kritischen Drücke der verwendeten Brennstoffe. Allerdings erschweren die nah- und überkritischen Phänomene den physikalischen Erkenntnisgewinn, welcher für die Realisierung eines effizienten und stabilen Verbrennungsprozesses notwendig ist. Überdies ist der Einsatz überkritischer Fluide ein möglicher Ansatz zur Effizienzsteigerung in der Energiewandlung und in Warmeübergangsprozessen. Neben der Verwendung von überkritischem Kohlenstoffdioxid im Brayton-Kreisprozess, wird der Einsatz von überkritischem Wasser als Kühl- und Prozessfluid in Kernreaktoren sowie überkritisches Methan als neuer “grüner” Treibstoff in Raketenantrieben erforscht.

Die Möglichkeit Schallgeschwindigkeiten sowie thermische und akustische Dämpfung zu messen, zeichnet laserinduzierte thermische Akustik (LITA) als eine vielversprechende Messtechnik für die Untersuchung nah- bis überkritischer Fluide aus. Darüber hinaus steigt die Signaleffizienz in Hochdruckumgebungen durch die nicht lineare Druckabhängigkeit der LITA Technik. Mithilfe einer Frequenzanalyse des LITA Signals können Schallgeschwindigkeiten ohne eine zusätzliche thermische Zustandsgleichung beziehungsweise Modellierung gemessen werden. Eine Analyse der Signalintensität über der Zeit bietet zudem die Möglichkeit die akustische Dämpfungsrate sowie die Temperaturleitfähigkeit zu bestimmen. Unter der Voraussetzung geeigneter analytischer Ausdrücke für die thermodynamischen Zustandsgrößen, können demnach lokale Mischungszustände abgeschätzt werden. Da sowohl Schalldispersion als auch Volumenviskosität in komplexen Fluiden bei nah- bis überkritischen Bedingungen von der akustischen Absorption abhängig sind, können zusätzliche physikalische Phänomene überkritischer Fluide erforscht werden.

Das Ziel dieser Arbeit ist die Anwendung von LITA zur Untersuchung makroskopischer Fluidphänomene in der Nähe des kritischen Punktes. Dies umfasst die folgenden, übergeordnete Forschungsziele. Zum einen wird die Volumenviskosität in komplexen, dichten Gasen sowie die Abhängigkeit der akustischen Dämpfung von der Konzentration einer Mischung untersucht. Zum anderen wird die Machbarkeit zeitaufgelöster LITA Messungen in komplexen Strömungsbedingungen bewertet. Um diese Forschungsziele zu verwirklichen, wurde eine Versuchsanlage konstruiert, welche die Untersuchungen reiner Gase und komplexer Mischungsprozesse bei hohen Drücken und Temperaturen ermöglicht. Überdies wurde der optische Aufbau des LITA Systems des ITLRs für Experimente bei hohen Drücken optimiert und ein neues Hochgeschwindigkeits–LITA Setup aufgebaut, welches eine Anpassung des LITA Messvolumens erlaubt. Darüber hinaus wurde eine neue Auswerteroutine, die sowohl den Frequenz- als auch den Zeitbereich des Signals analysiert, entwickelt und validiert. Mit dem Ziel die akustische Dämpfung sowie die Volumenviskosität zu messen, wurde mithilfe dieser Aufbauten und Routinen Untersuchungen in Kohlenstoffdioxid, Stickstoff und binären Mischungen in gasförmigen und gasähnlichen Zuständen durchgeführt. Darüber hinaus wurde ein Strahlmischungsprozess untersucht, um die Größe des LITA Messvolumens zu charakterisieren und die Abhängigkeit der akustischen Dämpfung von der untersuchten Mischungskonzentration zu bewerten. Abschließend wurden instationäre LITA-Messungen unter turbulenten, physikalisch komplexen Strömungsbedingungen im Nachlauf eines frei fallenden, verdunstenden Tropfens in einer überkritischen Atmosphäre durchgeführt. Ziel der Untersuchung war hierbei die Prüfung der Machbarkeit zeitaufgelöster LITA–Messungen sowie die quantitative Beschreibung des Verdunstungsprozesses.

CHAPTER 1

Introduction into near- to supercritical fluid phenomena

Increasing energy demands in addition to both political and social aspirations to reduce greenhouse gas emissions are continuously driving the interest for new sustainable energy solutions. Innovative energy sources as well as improvements in efficiency of both renewable and non–renewable power generation processes are vital to achieve long term sustainability. The latter includes the development of new thermodynamic cycles with regenerative use of excess heat of combustion and heat transfer processes.

Considering the entropy balance equation, the specific entropy production is inversely proportional to the density–temperature product. Consequently, entropy production decreases with increasing density/pressure. As higher operating pressures lead to a reduction in entropy production and, hence, higher efficiencies, combustion pressures have increased in the last decade to the point that they exceed the critical pressures of the injected fluids. However, the fundamental changes in fluid behaviour at near- to supercritical conditions are not yet fully understood and are of high importance for a stable and efficient combustion. Controlling the latter comprises profound understanding of the processes prior to the combustion, such as fluid injection, disintegration and subsequent evaporation. These processes have been receiving increased attention in the past years, as recent investigations of near- to supercritical fluid injection by Baab et al. [5], Crua et al. [18], Falgout et al. [28], Gerber et al. [33], Lamanna et al. [52], and Müller et al. [65] show. Apart from fluid injection studies, research in nearcritical evaporation on criteria characterising the onset of dense fluid mixing have been conducted by Banuti [7], Dahms and Oefelein [22], and Qiu and Reitz [84]. A detailed review on the validity of these criteria has been presented by Lamanna et al. [53].

Besides fluid injection in the vicinity of the critical point, supercritical fluids have been identified as innovative path for efficient heat transfer and energy conversion, see Pizzarelli [79]. The Brayton cycle is one example for the application of supercritical carbon dioxide in a closed thermodynamic cycle used for energy conversion, with the advantage to recover excess heat of the combustion process, as presented by Marchionni et al. [60] and Pecnik et al. [75]. Supercritical CO_2 is also applied in transcritical heat pump systems for cooling applications (see Austin and Sumathy [4]), whereas supercritical water is considered as coolant and process fluid in nuclear reactors to increase overall efficiency (see Pizzarelli [79]). While supercritical fluids, such as oxygen and hydrogen, are commonly used for rocket propulsion, the operating conditions exceed the critical values of the fluids by several magnitudes. Cooling of the combustion chamber in rockets is realised by a regenerative process using the propellant itself as coolant. As recently presented by Pizzarelli et al. [77], methane is considered as a 'green' fuel alternative to hydrazine in order to reduce environmental and operational hazards. However, since the operating conditions of the regenerative cooling system are only slightly above the critical point of methane, additional challenges, such as heat transfer deterioration as discussed by Pizzarelli et al. [78], have to be resolved.

Hereafter, the molecular and macroscopic characteristics of supercritical fluids are briefly summarised. Specifically, the highly non–linear fluid dynamic response to perturbations at transitions among supercritical fluid regimes are discussed. Moreover, the feasibility to investigate these fluid phenomena applying laser–induced thermal acoustic (LITA), the current research state of this measurement technique, and the motivation for the present work is presented.

1.1 Fluid phase transition in the supercritical regime

The behaviour of fluids becomes increasingly complex in the vicinity of the critical point. Furthermore, the underlying physics of the encountered macroscopic fluid phenomena, such as the close link between molecular dynamics and macroscopic thermodynamics, are not yet fully understood. By applying inelastic X–ray scattering and molecular dynamic simulations Gorelli et al. [34, 35] have studied the propagation of density fluctuations in supercritical fluids. These investigations have shown a direct correlation between the damping of acoustic waves in the THz–regime and extrema in thermodynamic properties, such as specific isobaric heat capacity c_p, thermal diffusivity D_T, and bulk μ_v viscosity. Based on these investigations a distinction of fluids at supercritical pressures is possible.

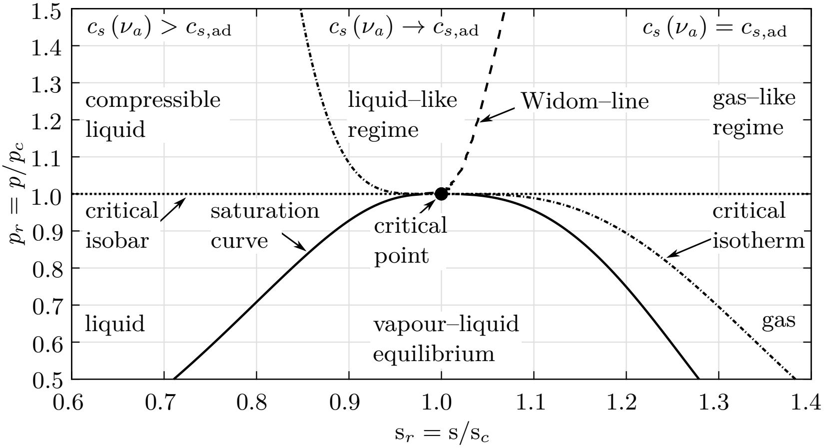

Figure 1.1: Thermodynamic fluid states based on microscopic investigations and sound dispersion measurements ($c_s(\nu_a)$). Reduced properties are scaled with the properties in the critical point. Reduced pressure: $p_r = p/p_c$; reduced entropy: $\mathrm{s}_r = \mathrm{s}/\mathrm{s}_c$. Widom–line: line of maxima in specific isobaric heat capacity. Diagram is computed for pure carbon dioxide. Necessary thermodynamic data are taken from Lemmon et al. [56].

The resulting thermodynamic fluid states are exemplarily depicted for carbon dioxide in Fig. 1.1 showing the reduced entropy $\mathrm{s}_r = \mathrm{s}/\mathrm{s}_c$ as a function of the reduced pressure $p_r = p/p_c$. Reduced properties are hereby scaled with the properties in the critical point. The latter are indicated by the subscript $_c$. The so–called Widom–line, which is characterised by the maximum in specific isobaric heat capacity, divides the supercritical region into a compressible liquid / liquid–like regime and in a gas–like regime. Starting from the compressible liquid / liquid–like regime and heading towards the Widom–line, Gorelli et al. [35] have observed an interaction of acoustic and thermal waves leading to positive sound dispersion, while in the gas–like regime adiabatic sound propagation is recovered. Sound dispersion is the dependency of the propagation speed upon a forced acoustic wave on its frequency. Positive sound dispersion is therefore an increase in propagation velocity depending of the frequency of the forced acoustic wave ($c_s\left(\nu_a\right) > c_{s,\mathrm{ad}}$). As discussed by Gorelli et al. [35], in the limit of low frequencies the longitudinal sound velocity is equal to the adiabatic speed of sound $c_{s,\mathrm{ad}}$. Note that on a macroscopic scale, as observed in liquids by Mysik [66], positive sound dispersion occurs when volume viscosities are non–negligible and the frequency of the induced acoustic waves are in a similar time scale as the molecular relaxation processes.

In compliance with classical thermodynamics another partition in the state diagram is introduced at the critical isotherm at supercritical pressures. The latter separates the liquid–like regime from the compressible liquid state, as shown in Fig. 1.1. As discussed by Bencivenga et al. [10] and Simeoni et al. [98], the supercritical region between the critical isotherm and the Widom–line preserves sound dispersion at large densities, while resembling the molecular structure of a gas, as has been observed by Santoro and Gorelli [87]. As this region exhibits dynamic and thermodynamic properties intermediate between gas–like and compressible liquid states, it can be denoted as the liquid–like regime. Note that molecular dynamic simulations conducted by Banuti et al. [8] support the findings by Santoro and Gorelli [87]. Banuti et al. [8] have shown that for an isothermal transition at supercritical temperatures the molecular structure of a fluid evolves with increasing pressure from an ideal gas to a dense gas structure when crossing the Widom–line. In case of an isobaric transition at supercritical pressures starting from subcritical temperatures, the molecular structure changes from a highly correlated atomic liquid structure to a progressively less correlated structure with increasing temperature. Based on these observations Banuti [7] and Oschwald et al. [71] have postulated a so–called pseudo–boiling transition, when crossing the Widom–line from a liquid–like to a gas–like state.

On a macroscopic scale challenges in supercritical fluid applications are directly related to transitions among supercritical fluid regimes. For first order derivatives of the Gibbs free energy, such as density ϱ, the Widom–line transition is continuous. However second order and higher derivatives, such as isothermal compressibility β_T, specific isobaric heat capacity c_p, and thermal diffusivity D_T, experience extrema. Figure 1.2 presents these thermodynamic fluid properties at an isobaric Widom–line transition for pure carbon dioxide. Additionally, the dynamic shear viscosity μ_s is presented. The Widom–line, critical isobar, critical isotherm, critical point, and the reference pressure for data extraction are depicted on the left in a reduced pressure p_r, reduced temperature T_r

diagram. Note that besides c_p, a Widom–line can be also specified for maxima in the isothermal compressibility β_T. However, for reduced pressures below 1.5 the c_p–Widom–line and the β_T–Widom–line basically overlap. Concordantly, in case of a Widom–line transition in the vicinity of the critical point both the compressibility of a flow (β_T) and the capacity to store energy (c_p) increase.

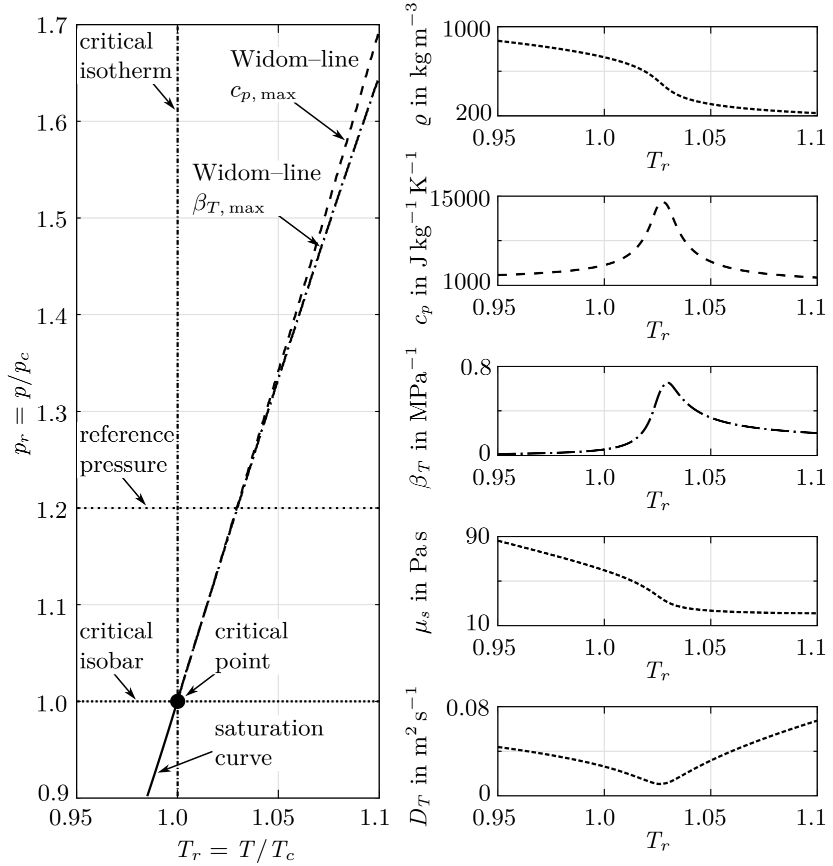

Figure 1.2: Macroscopic fluid properties crossing the Widom–line for carbon dioxide. Reduced properties are scaled with the properties in the critical point. Reduced pressure: $p_r = p/p_c$; reduced temperature: $T_r = T/T_c$. Necessary thermodynamic data are taken from Lemmon et al. [56].

These maxima in response functions are the cause of a non–linear coupling between perturbations in thermodynamic properties and compressible flow dynamics. The increased compressibility leads to anomalous fluid phenomena, such as thermo–convective instabilities and heat transfer deterioration. Thermo–convective instabilities are a consequence of the non–linear response to large pressure and temperature gradients associated to the maxima in β_T and c_p.

Heat transfer deterioration occurs due to the limited capacity to absorb heat in compressible flows (see Zierep [120]). For subsonic flows in cooling channels the maximum absorbable heat decreases with increasing local Mach number. In turn, the elevated compressibility indirectly contributes to an increase in the local Mach number by increasing the speed of sound of the fluid. Consequently, the capability of heat absorption significantly reduces at the maxima in isothermal compressibility irrespective of the specific isobaric heat capacity.

1.2 Current state of laser–induced thermal acoustics

Based on the previous considerations the motivation to apply laser–induced thermal acoustics in the investigation of near- to supercritical fluid phenomena on a macroscopic scale becomes clear. As LITA is capable to simultaneously detect acoustic damping rates $\mathit{\Gamma}$, thermal diffusivities D_T, and speed of sound data c_s, it provides key parameters to enable investigations of the different supercritical fluid regimes presented in Fig. 1.1. Moreover, by applying LITA in injection studies quantitative data for the validation of analytical and numerical models can be provided. The latter has previously been shown by Baab et al. [6] for speed of sound measurements using LITA in multi–component jets mixing at high pressure conditions.

Laser–induced thermal acoustics, also referred to as laser–induced (transient) grating spectroscopy (LIGS) are commonly applied to measure transport properties in quiescent environments, where the spatial resolution is not important to the investigation. Kimura et al. [48] have been among the first to measure transport properties in high pressure fluids with the transient grating method. The focus has hereby been in the determination of thermal and mass diffusion as well as sound propagation in the vicinity of the critical point. Specifically, the thermal diffusion and sound propagation of a binary mixture of carbon dioxide and hexafluorophosphate has been studied by Demizu et al. [24]. Instead, Kimura et al. [49, 50] have investigated the vibrational energy relaxation of azulene in its supercritical and liquid state. A comprehensive review on the application of LIGS in gas–phase diagnostics has been presented by Stampanoni-Panariello et al. [101]. Using a LIGS setup with infinite wave fronts (unfocused beams) Stampanoni-Panariello et al. [101] have conducted thermometry, velocimetry, concentration measurements and investigations of energy transfer processes as well as resonant fluid transitions. Acoustic damping rates in pure fluids with pressures up to 2.5 MPa at room temperature have been determined by Li et al. [57] analysing the signals time–domain. This investigation has later been extended by Li et al. [58] to binary mixtures of atomic species. Heat conduction, speed of sound as well as viral coefficients have been determined by Latzel and Dreier [55] using resonant LIGS for pressures up to 50 MPa by analysing both the oscillation and the long term signal decay. A similar signal analysis has been performed by Willman et al. [118] to determine the pressure by examining the lifetime of the grating. Using a high–repetition rate laser, Förster et al. [31] successfully have conducted time–resolved thermometry applying LIGS under static and transient cell conditions.

It is important to emphasise that the majority of the presented studies apply an optical arrangement with unfocused grid excitation beams, where infinite wave fronts can be assumed. This leads to a poor spatial resolution due to a large optical grid spacing with an order of magnitude $\mathcal{O}\left(10^1\,\text{mm}\right)$ in diameter and $\mathcal{O}\left(10^2\,\text{mm}\right)$ in length. While this spatial resolution is sufficient for studies in pure fluids and mixture, it is not adequate for the investigation in jet disintegration or droplet evaporation. Both experience small–scale phenomena, hence, a high spatial resolution is imperative. Nevertheless, LITA is indeed sensitive to such small–scale processes. By using focused beams in their studies Baab et al. [5, 6] and Förster et al. [32] have proven the capability of the LITA technique to determine speed of sound data along the radial and lateral axis of a jet disintegration process, while Steinhausen et al. [107] have determined acoustic damping rates and speed of sound data in pure substances using a LITA system with focused beams. Due to the focused beams the spatial resolution has been in an order of magnitude $\mathcal{O}\left(10^{-1}\,\text{mm}\right)$ in diameter and $\mathcal{O}\left(10^0\,\text{mm}\right)$ in length. The effects of the finite beam sizes on LITA signals has been theoretically studied by Cummings et al. [21], while Schlamp et al. [89] additionally have taken beam misalignments into account.

1.3 Objectives and organisation of this thesis

The rationale of this thesis has to be seen in context of the supercritical fluid research and within the capability of the LITA technique to detect sound propagation, acoustic damping, and thermal attenuation, as presented above. LITA is a valuable diagnostic tool to characterise supercritical fluids as well as nearcritical fluid injection phenomena.

Based on these considerations, the purpose of this work is to apply LITA to investigate macroscopic fluid phenomena at nearcritical fluid conditions. The latter include three main research objectives. First, the importance of acoustic damping and volume viscosities at high density/pressure conditions in fluids in gaseous and gas–like states are assessed. Second, the dependency of acoustic damping rates on mixing states are investigated. Third, the feasibility of time–resolved LITA measurements with a high–speed LITA system under complex flow condition is evaluated. To achieve these main objectives, the following sub–goals have been addressed, which also reflect the structure of this thesis:

Development Based on the design of a previous pressure chamber, a new, modular, optically accessible test rig is developed. It facilitates the envisaged investigations in pure atmospheres, predefined binary mixtures, gaseous jet mixing processes, and droplet evaporation at nearcritical conditions. Moreover, the LITA setup of the ITLR developed by Förster [30] and Hell [41] is optimised for high pressure environments. In addition, a new high–speed LITA arrangement with an adjustable measurement volume using a high–repetition laser is set up.

Post–processing A post–processing methodology has been developed for a frequency and time–base analysis of the LITA signals, which allows the simultaneous extraction of speed of sound and acoustic damping rate.

Validation To assess the validity and accuracy of the post–processing algorithm a thorough validation of both the time–based and the frequency–based extracted data has been conducted.

Application The validated and characterised LITA arrangements and the post–processing methodology are applied to determine acoustic damping rates and speed of sound data in carbon dioxide, nitrogen and predefined mixtures at high pressure and temperature conditions. Moreover a gaseous jet mixing process is evaluated to characterise the size of the LITA measurement volume and to assess the dependency of acoustic damping on the local mixing state. At last, transient speed of sound measurements have been conducted in the wake of a free falling droplet evaporating in a supercritical atmosphere to evaluate the feasibility of time–resolved LITA measurements under complex flow conditions and to further characterise the evaporation process.

Hereafter, the physical fundamentals on LITA, acoustic damping, and near-critical droplet evaporation are discussed in chapter 2, while the experimental facility together with the LITA setups and optical system for flow visualisation are presented in chapter 3. The post–processing methodology and the validation are then introduced in chapter 4 and 5, respectively. In chapter 6 the envisaged application of LITA in nearcritical fluid phenomena is addressed. The thesis concludes with a summary of the obtained results and puts them into perspective regarding the initially stated objectives.

CHAPTER 2

Physical fundamentals and theoretical considerations

In the scope of this thesis macroscopic fluid phenomena in the vicinity of the critical point are investigated by the non–intrusive measurement technique, namely laser–induced thermal acoustics (LITA). The latter is capable of characterising speed of sound, acoustic attenuation and volume viscosities. Additionally, for known mixing rules the local state of the mixture can be determined. The following chapter summarises the necessary scientific fundamentals of the applied measurement technique as well as theoretical considerations on acoustic attenuation and droplet evaporation. Moreover a brief literature review on volume viscosity models for dilute and dense gases is presented.

2.1 Fundamentals of laser–induced thermal acoustics

Laser–induced thermal acoustics utilises opto–acoustic non–linear interactions of matter with an optical interference pattern to induce a density perturbation grating. The latter is detected based on acousto–optic effects, leading to the possibility to independently and simultaneously detect speed of sound data, acoustic damping rates as well as thermal diffusivities. LITA classifies as a seedless, non–intrusive measurement technique. It is based on the fundamental physics of laser–induced gratings as well as non–linear optics. A theoretical framework on the latter has been presented by Boyd [15], while the fundamentals of laser–induced dynamic gratings have been summarised by Eichler et al. [26]. A detailed review on the early developments relevant for LITA and the distinction between LITA and degenerate four–wave–mixing has been presented by Cummings [20].

Theoretical approaches describing the generation of the laser–induced grating as well as the inherent opto–acoustic and acousto–optic interaction can be found in the works by Cummings et al. [21] and Stampanoni-Panariello et al. [100]. Note that the analytical expression presented by Stampanoni-Panariello et al. [100] assumes wave fronts of infinite extent, while the framework by Cummings et al. [21] takes finite beam sizes into account. In the limit of infinite beam sizes both theories merge. To account for beam misalignments and flow velocities Schlamp et al. [89] extended the theory presented by Cummings et al. [21]. In the following the physics necessary to understand the interpretations and modelling approaches in the present work are summarised.

2.1.1 Opto–acoustic effects in the excitation phase

In the first phase of the LITA technique two short pulsed excitation laser beams with identical linear polarisation are crossed resulting in a spatially periodic modulated polarisation/light intensity distribution. The propagation of the two excitation input waves is determined by their wave vectors $\boldsymbol{k}_{\mathrm{exc},1,2}$, while the crossing angle is denoted with Θ.

A schematic representation of the beam crossing and the resulting interference pattern is shown in Fig. 2.1, with reference to Cummings [20]. The Gaussian half–width of the excitation beams is denoted with ω. The grating is defined by its grating vector $\boldsymbol{q}$, which is perpendicular to the fringes. Following the theoretical framework on induced grating spectroscopy by Eichler et al. [26] the grating vector is related to the excitation wave vectors according to

$$\boldsymbol{q} = \pm\,(\boldsymbol{k}_{\mathrm{exc},1} + \boldsymbol{k}_{\mathrm{exc},2}) \quad \text{with} \quad |\boldsymbol{q}| = \; q = 2\,\pi\,\Lambda^{-1} \; . \tag{2.1}$$

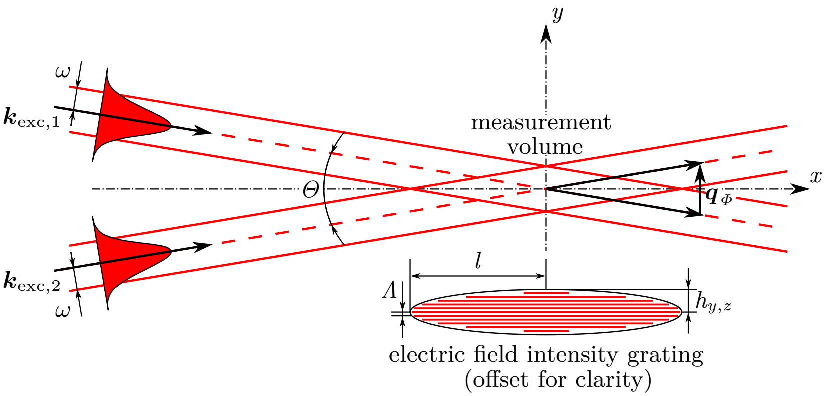

Figure 2.1: Schematic drawing of the excitation beam field distribution resulting in the interference pattern, according to Cummings [20].

The magnitude of the grating vector q is hereby defined by the grid spacing of the optical interference pattern Λ. The latter is determined by the beams' crossing angle Θ as well as the wavelength of the excitation beams λ_{exc}.

$$\Lambda = \frac{\lambda_{\text{exc}}}{2\sin\left(\Theta/2\right)} \tag{2.2}$$

The generated interference pattern has the shape of an ellipsoid with a length l, width h_y, and a height h_z. With reference to the theoretical model by Schlamp et al. [89] the latter are defined as

$$l = \frac{\omega}{\sin\left(\Theta/2\right)} \ , \quad h_y = \frac{\omega}{\cos\left(\Theta/2\right)} \ , \quad \text{and} \quad h_z = \omega \ . \tag{2.3}$$

Since the beam crossing angle Θ is small the length of the interference pattern is large compared to height and width ($l \gg h_{y,z}$) and the assumption $h_y = h_z = \omega$ is justified. This leads to a measurement volume of ellipsoid shape elongated in x–direction.

The spatially periodic modulated light intensity field induces a density grating with an identical spacing within the measurement volume in the probed fluid.

The complex dielectric susceptibility χ is the property describing the opto–acoustic response of the fluid to the imposed electric field. Two opto–acoustic effects, namely electrostriction and thermalisation, are primarily responsible for the generation of the density grating. Electrostriction is proportional to the real part of the dielectric susceptibility $\mathcal{U}_{eP} \propto \mathrm{Re}\,(\chi)$, while thermalisation is proportional to the negative of the imaginary part $\mathcal{U}_{\Theta} \propto -\Im\,(\chi)$. The modulation depth of electrostriction and thermalisation is indicated with $\mathcal{U}_{eP}$ and $\mathcal{U}_{\Theta}$, respectively. (with reference to Cummings et al. [21])

Electrostriction

Electrostriction is described by Boyd [15] as the tendency of a fluid or solid to increase in density when subjected to an electric field, such as the modulated light intensity distribution. In case of fluids, this increase in density leads to an acceleration of the molecules towards regions with high electric field or optical intensity. Subsequently, a molecular velocity grating is generated, which in response leads to the creation of a density grating (see Cummings et al. [21]). These electrostrictive induced density fluctuations are sometimes referred to as phonons. Based on the induced molecular velocity grating the temporal evolution of the modulation in density can be explained by two counter–propagation acoustic wave packets, which move at the speed of sound and decay due to acoustic attenuation [21]. The direction of propagation is hereby defined by the grating vector $\boldsymbol{q}$. Note that the acoustic wave packets are sometimes referred to as phonons.

Thermalisation

Following the framework by Cummings et al. [21], thermalisation occurs when the wavelength of the excitation beams are within a peak of the imaginary part of the fluids susceptibility. Based on this resonance line, the energy of the optical interference pattern is absorbed by the fluid. When the excited molecules return to their ground state, the absorbed energy is released as thermal energy leading to perturbations in temperature. Subsequently a stationary, isobaric density grating is induced, which dominantly decays by thermal diffusion. In the limit of instantaneous heat release the grid spacing of the density fluctuations is equal to the optical interference pattern. The thermally induced density fluctuations are sometimes referred to as thermons. Note that according to Schlamp et al. [89], the perturbations in temperature that are leading to the density grating are small ($\Delta T \ll 1\,\mathrm{K}$).

2.1.2 Light scattering in the interrogation phase

In the interrogation phase the induced fluctuations in optical properties, such as density, dielectric susceptibility, and refractive index, within the probed volume are detected by a third input wave. The latter is referred to as interrogation beam, which is scattered on the spatially periodic modulated fluctuations in density, generating a fourth signal beam. In the framework by Eichler et al. [26], two dominant forms of light scattering important to the LITA technique are presented. Light scattering from a (non–resonant) acoustic wave (phonon) is hereby referred to as stimulated Brillouin scattering (SBS). In contrast, scattering from a resonant thermally induced stationary isobaric density grating (thermon) is caused by stimulated (thermal) Rayleigh scattering (STRS). However, it is important to emphasise that eventhough the scattering phenomena inherent in the LITA technique are Brillouin and Rayleigh scattering, the experimental technique is different from the classical stimulated Brillouin/Rayleigh scattering approach.

To ensure an effective scattering process a precise alignment of the interrogation beam with respect to the angle and position of the excitation beams is vital. Figure 2.2 depicts a schematic representation of the signal beam scattering process, according to Cummings [20]. The crossing angle of interrogation beam Φ is hereby defined as the angle between the interrogation and the signal beam. The Gaussian half–width of the interrogation beam is indicated with σ.

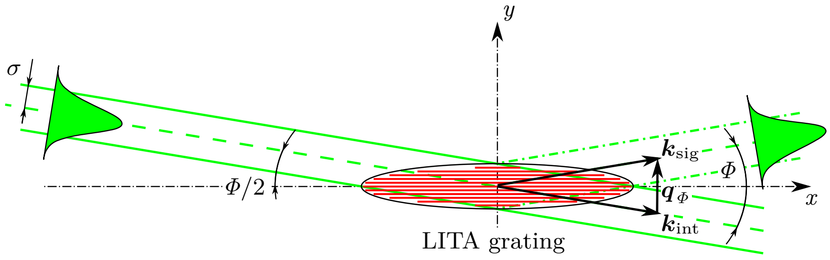

Figure 2.2: Schematic representation of the signal beam scattering, according to Cummings [20].

A strong coherent signal beam is generated, when the wave fields of the grating and the interrogation beam interfere constructively. As refereed by Eichler et al. [26], this phase matching condition is ensured when the wave vector of the interrogation $\boldsymbol{k}_{\text{int}}$ and signal $\boldsymbol{k}_{\text{sig}}$ beam are related to the grating vector $\boldsymbol{q}$ according to equation (2.4).

$$\boldsymbol{k}_{\text{sig}} + \boldsymbol{k}_{\text{int}} = \pm\, b\, \boldsymbol{q} \quad \text{with} \quad b = \pm 1\,,\, \pm 2\,,\, \ldots \tag{2.4}$$

The phase matching condition in equation (2.4) is equivalent to the well–known Bragg condition shown by equation (2.5). Hence, the order of the Bragg scattering is denoted with b. The wavelength of the interrogation beam is indicated by λ_{int}, while the excitation beams wavelength is λ_{exc}.

$$\frac{\sin\left(\Phi/2\right)}{\lambda_{\text{int}}} = b\,\frac{\sin\left(\Theta/2\right)}{\lambda_{\text{exc}}} \quad \text{with} \quad b = \pm 1\,,\, \pm 2\,,\, \ldots \tag{2.5}$$

The planar representation of the input waves alignment in Fig. 2.1 and Fig. 2.2 is ideal. However, in an optical arrangement the positioning of the laser beams is three dimensional and subjected to small misalignments. The reference frame for signal analysis using the theoretical model by Schlamp et al. [89] is, hence, displayed in Fig. 2.3.

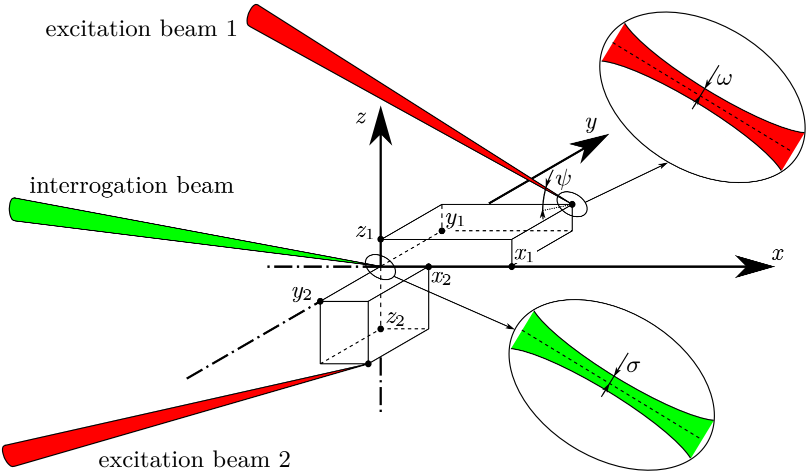

Figure 2.3: Reference frame for signal analysis, according to Schlamp et al. [89].

The interrogation beam is hereby located in the centre. The intersection angle of interrogation and excitation beam in x–z plane is denoted with ψ. Note that beams with finite beam sizes are applied. Concordantly, the Gaussian half–width of the interrogation beam σ and the excitation beams ω have to be determined at the intersection plane. Following the derivation by Schlamp et al. [89], the linear beam misalignments in x, y, and z–direction are expressed according to equation (2.6).

$$\begin{aligned} \xi &= (x_1 + x_2)/2 \,, \quad & \eta &= (y_1 + y_2)/2 \,, \quad \text{and} \quad & \zeta &= (z_1 + z_2)/2 \\ \bar{\xi} &= (x_1 - x_2)/2 \,, \quad & \bar{\eta} &= (y_1 - y_2)/2 \,, \quad \text{and} \quad & \bar{\zeta} &= (z_1 - z_2)/2 \end{aligned} \tag{2.6}$$

Misalignment in x–direction is denoted with ξ and $\bar{\xi}$, while y and z–directions is indicated with η, $\bar{\eta}$ and ζ, $\bar{\zeta}$, respectively. Note that in the work by Schlamp et al. [89] no angular misalignment is assumed. Since the length of the interference pattern is large compared to height and width ($l \gg h_{y,z}$) any rotations of the grating can be excluded. Consequently, the grating remains always perpendicular to the y–direction such that the sound waves are considered to propagate parallel to the y–axis.

2.1.3 Signal detection and fluid property deduction

In the scope of this work only the signal beam scattered in the first order of Bragg's law is used for the deduction of flow properties. Following the theoretical framework on stimulated Brillouin scattering by Boyd [15] together with the adaptation for the incidence angle of the interrogation beam by Still [111] the magnitude of the grating vector q can be expressed as

$$|\boldsymbol{q}| = q = 2\,|\boldsymbol{k}_{\text{int}}|\,\sin(\varPhi/2) = \frac{4\,\pi}{\lambda_{\text{int}}}\,\sin(\varPhi/2) \;. \tag{2.7}$$

In case of non–resonant fluid behaviour, the signal beam is scattered only on the electrostrictively induced counter–propagating sound waves. The SBS is hereby inelastic. Hence, the incoming photons either experience a loss (Stokes process) or a gain (anti–Stokes process) in energy. This leads to a Doppler shift of the laser light frequency of the interrogation beam ν_{int}. The Doppler shift $\varDelta\nu$ is also denoted as Brillouin frequency, which expresses the frequency of the acoustic wave ν_a. With reference to the framework of Boyd [15] and equations (2.2), (2.5), and (2.7) the Doppler shift is computed with

$$\Delta\nu\,(\pm c_s) = \nu_a = q\,\frac{c_s}{2\,\pi} = \frac{2\,c_s}{\lambda_{\mathrm{int}}}\,\sin\left(\Phi/2\right) = \frac{c_s}{\Lambda}\;. \tag{2.8}$$

In case of a resonant fluid response the stimulated thermal grating leads to an additional elastic Rayleigh scattering of the signal beam. The photons energy is hereby conserved.

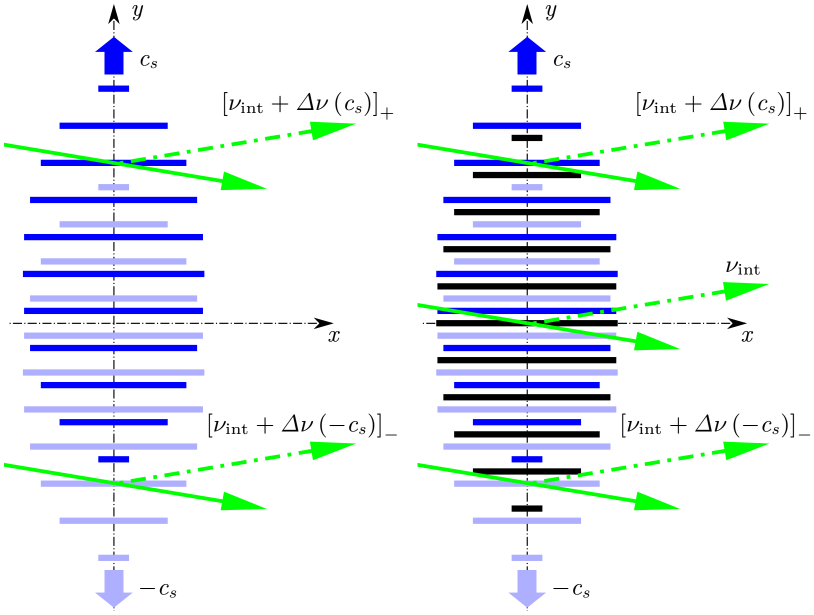

(a) Non–resonant fluid response. (b) Resonant fluid response.

Figure 2.4: Light scattering of the interrogation beam on the counter–propagating acoustic waves (blue shades) and the stationary thermal gradient (dark grey), respectively. Note that grating is elongated in y–direction for clarity.

Figure 2.4 schematically illustrates the scattering of the interrogation beam for a non–resonant and resonant fluid response in a quiescent atmosphere with homodyne detection. The counter–propagating acoustic waves are presented in blue shades, while the superimposed stationary thermal gradient is depicted in dark grey.

The frequency of the Doppler–shifted signal beams and the interrogation beam is in the THz–regime, which is impossible to resolve with available electronic detectors. To isolate the Doppler–shift from the initial frequency the beams are superimposed on an avalanche detector. The resulting interference generates an output voltage modulated at a beat frequency $\varOmega = \nu_+ - \nu_-$ in the MHz–regime, see Förster [30]. The latter is calculated by the difference of the frequencies within the signal beam.

In case of the pure electrostrictive grating (non–resonant fluid response) only the inelastic scattered beams interfere with each other. With reference to Förster [30], this results in signals with a beat frequency $\varOmega_{2c_s}$ twice the Brillouin frequency, derived according to

$$\varOmega_{2c_s} = \left[\nu_{\mathrm{int}} + \varDelta\nu\,(c_s)\right]_+ - \left[\nu_{\mathrm{int}} + \varDelta\nu\,(-c_s)\right]_- = 2\,\varDelta\nu\,(\pm c_s) = 2\,\nu_a\ . \tag{2.9}$$

The Stokes process is hereby indicated by the subscript $_-$, while the anti–Stokes process is shown with $_+$. For a resonant fluid response the signal beam is scattered on the counter–propagating sound waves as well as on the stationary thermal grating. Since all the three signal beams interfere at the detector, this results in an additional beat frequency $\varOmega_{c_s}$ equal to the Brillouin frequency derived from

$$\varOmega_{c_s} = \left[\nu_{\mathrm{int}} + \varDelta\nu\,(\pm c_s)\right]_\pm - \nu_{\mathrm{int}} = \varDelta\nu\,(\pm c_s) = \nu_a\ . \tag{2.10}$$

It has been shown by Förster [30] that for flows with a bulk velocity in y–direction the homodyne detected beat frequencies in equations (2.9) and (2.10) experience no dependency on the flow velocity. By mixing the signal beam with an unperturbed reference beam (heterodyne detection) flow velocities in y–direction for both resonant and non–resonant fluid behaviour can be determined. A comprehensive analysis is presented by Förster [30].

2.1.4 Thermodynamic property deduction in the temporal domain

To evaluate the temporal domain of a LITA signal, the dependencies of the observed relaxation processes need to be understood. The latter can be assimilated to a damped harmonic oscillation, see Steinhausen et al. [107]. As an intuitively accessible example, a simple analytical solution of the time–dependent dimensionless diffraction efficiency $\mathit{\Psi}(t)$ of a LITA signal has been provided by Cummings [19]. The relation in equation (2.11) is obtained for a short–duration, monochromatic driver beam with infinite wave fronts (unfocused beams) assuming a dominant thermalisation process

$$\mathit{\Psi}(t) \propto \left[C \exp\left\{ -D_T q^2 t \right\} + B \exp\left\{ -\mathit{\Gamma} q^2 t \right\} \cos\left\{ \upsilon \left(t - t_0 \right) \right\} \right] \;, \qquad (2.11)$$

where t denotes the time, t_0 is the time of the laser pulse, B and C are dimensionless amplitudes, $\mathit{\Gamma}$ is the acoustic damping rate, D_T is the thermal diffusivity, and υ is the angular frequency of the acoustic wave. Following the derivation of Stampanoni-Panariello et al. [99] the latter can be expressed as

$$\upsilon = \sqrt{{\upsilon_0}^2 - q^4 \mathit{\Gamma}^2} \quad \text{with} \quad \upsilon_0 = q c_s \;. \qquad (2.12)$$

The natural frequency of the acoustic wave is hereby denoted with υ_0. For a system with small acoustic damping rates and/or grating vectors small in magnitude (${\upsilon_0}^2 \gg q^4 \mathit{\Gamma}^2$), the angular frequency of the acoustic wave υ is close to the undamped natural frequency υ_0. The relation in equation (2.12) shows indeed a dependency of the speed of sound upon the acoustic damping rate. Note that for the results presented in this work, ${\upsilon_0}^2 \gg q^4 \mathit{\Gamma}^2$ can be applied. Concordantly, the well–known condition that sound waves propagate at the adiabatic speed of sound is recovered. Moreover, based on equation (2.12) the local speed of sound is a function of the magnitude of the grating vector and, hence, the frequency of the sound wave. This effect is known as sound dispersion and has been observed in liquids by Mysik [66]. In case of supercritical fluids at compressed liquid and liquid–like states a significant sound dispersion has been observed by Bencivenga et al. [10], Gorelli et al. [35], and Simeoni et al. [98]. However, since investigations are performed at microscopic length scales the magnitude of the grating vector is $\mathcal{O}\left(q_{\mathrm{Gorelli}}\right) = 1\,\mathrm{nm}^{-1}$. In comparison for the LITA arrangement applied in this work $\mathcal{O}\left(q_{\mathrm{LITA}}\right) = 10^{-4}\,\mathrm{nm}^{-1}$. Hence, (positive) sound dispersion phenomena cannot be investigated with the system used in the present work.

2.2 Essentials of acoustic damping and volume viscosity

Applying laser–induced thermal acoustics in macroscopic fluid phenomena, such as mixing processes, provides the opportunity to independently and simultaneously detect speed of sound data, acoustic damping rates and thermal diffusivities. The rationale for the application at conditions in the vicinity of the critical point is twofold. First, measurements of acoustic damping rates allow indirect estimations of volume viscosities. The consideration of the latter is essential at supercritical states to assess the importance of sound dispersion in supercritical fluids states, to improve stress tensor models, and to enhance kinetic energy dissipation models in supercritical fluid flow simulations. Note that in simulations and theoretical predictions of complex flow phenomena in gases, Stokes' hypothesis is commonly applied. The latter in fact neglects volume viscosity compared to shear viscosity. Second, as discussed by Steinhausen et al. [107], simultaneous and independent measurements of speed of sound data, acoustic damping rates, and thermal diffusivities provide an option to derive a set of independent equations to locally define a mixture. The local state of a fluid mixture is hereby defined by the mixing temperature T_{mix}, the mole fraction of the fluid X_{Fluid}, and the pressure p. Speed of sound $c_{s,\mathrm{mix}}$, acoustic damping rate $\mathit{\Gamma}_{\mathrm{mix}}$ and thermal diffusivity $D_{T,\mathrm{mix}}$ depend on these mixing states and can be expressed in the following way.

$$\begin{aligned} c_{s,\mathrm{mix}}\left(p_{\mathrm{ch}}, T_{\mathrm{mix}}, X_{\mathrm{Fluid}}\right) &= c_{s,\mathrm{LITA}} \\ \mathit{\Gamma}_{\mathrm{mix}}\left(p_{\mathrm{ch}}, T_{\mathrm{mix}}, X_{\mathrm{Fluid}}\right) &= \mathit{\Gamma}_{\mathrm{LITA}} \\ D_{T,\mathrm{mix}}\left(p_{\mathrm{ch}}, T_{\mathrm{mix}}, X_{\mathrm{Fluid}}\right) &= D_{T,\mathrm{LITA}} \end{aligned} \tag{2.13}$$

Extracting $c_{s,\mathrm{LITA}}$, $\mathit{\Gamma}_{\mathrm{LITA}}$, and $D_{T,\mathrm{LITA}}$ by applying LITA in a controlled environment at known chamber pressure p_{ch}, it follows that T_{mix} and X_{Fluid} are the only unknown fluid properties of the investigated mixture. Provided a thorough calibration and subsequent validation in well known binary mixtures, local mixing parameters can be determined by equation (2.13), when coupled to non–ideal mixture data. The latter are accessible for the thermal diffusivity and speed of sound by the National Institute of Standards and Technology (NIST) database by Lemmon et al. [56]. However, the acoustic damping has to be modelled in more detail and mixing effects have to be considered.

In classic acoustic attenuation of ideal gases, dissipation of the energy of a sound wave is caused by internal friction and heat conduction, as discussed by Herzfeld and Litovitz [44]. It depends therefore on both the shear viscosity and the thermal conductivity of the fluid. At real gas conditions and in complex fluids, however, additional losses due to molecular interactions and the species' molecular degrees of freedom arise, as discussed by Ejakov et al. [27]. Following the derivation by Boon and Yip [11] the acoustic damping rate of an isotropic fluid depends on the fluid density ϱ, the shear viscosity μ_s, the specific heat ratio κ, the thermal conductivity k, the specific isobaric heat capacity c_p, and the volume viscosity μ_v. The latter is, from a macroscopic point of view, the resistance to (rapid) compression or expansion of a fluid. From a molecular standpoint, volume viscosity can be associated with the time necessary for distributing imposed energy among rotational and vibrational degrees of freedom, as referred to by Tisza [112].

$$\mathit{\Gamma} = \frac{1}{2\,\varrho} \left[\frac{4}{3}\,\mu_s + \mu_v + (\kappa - 1)\,\frac{k}{c_p} \right] \tag{2.14}$$

The relation for the acoustic damping rate $\mathit{\Gamma}$ shown in equation (2.14), is hereby derived from the linearised balance equations for mass, momentum, and energy. The applied framework of generalised hydrodynamic fluctuation developed by Boon and Yip [11], is applicable to the LITA technique, since changes in dielectric constants due to an electric field intensity grating are considered in terms of fluctuations in local thermodynamic properties. Note that due to the rise in c_p in the vicinity of the Widom–line, see Fig. 1.2, the last expression $(\kappa - 1)\, k/c_p$ is negligible. This is, as stated by Herzfeld and Litovitz [44], also true in liquids.

For monoatomic ideal gases, Herzfeld and Litovitz [44] have shown that the volume viscosity μ_v is zero. Hence, at ideal gas conditions the acoustic damping rate can be simplified to the classical acoustic damping rate Γ_c, expressed by equation (2.15). Following the framework by Herzfeld and Litovitz [44], the classical acoustic damping rate is derived from the Stoker–Navier equation for classical sound absorption.

$$\mathit{\Gamma}_c = \frac{1}{2\,\varrho} \left[\frac{4}{3}\,\mu_s + (\kappa - 1)\,\frac{k}{c_p} \right] \tag{2.15}$$

Moreover, at real gas conditions of monoatomic gases the significance of the volume viscosity is assessed by the theoretical framework by Meier et al. [62]. Applying the molecular dynamic simulation with Lennard–Jones fluids by Meier et al. [62] viscosity ratios μ_v/μ_s over fluid density ϱ for the noble gas argon are estimated. The results are depicted in Fig. 2.5. The right graph presents values in the density range investigated by Meier et al. [62], while the left image shows viscosity ratios in the density range regarded in this work.

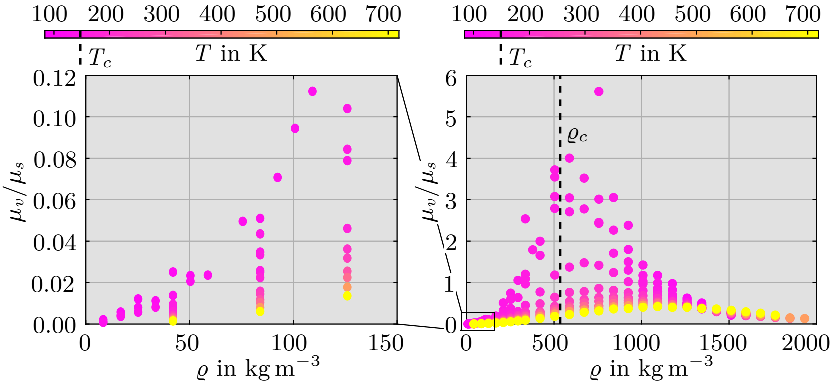

Figure 2.5: Viscosity ratio μ_v/μ_s for pure argon with volume viscosities calculated using the model by Meier et al. [62], whereas shear viscosity data are taken from Lemmon et al. [56]. **Left:** Viscosity ratio at low densities as expected in the presented work. **Right:** Viscosity ratio at the density range investigated by Meier et al. [62].

The right diagram in Fig. 2.5 shows that at high temperatures ($T > 400\,\mathrm{K}$) even for high density conditions the volume viscosity is much smaller as the shear viscosity. In case of a gaseous state ($\varrho < \varrho_c$, $T > 400\,\mathrm{K}$) argon behaves similar to an ideal gas. In contrast for temperatures $T < 400\,\mathrm{K}$ the volume viscosity has the same or higher magnitudes as the shear viscosity. Moreover, at nearcritical conditions ($\varrho \approx \varrho_c$, $T \approx T_c$) the viscosity ratio rises to values greater than one. As shown in the left diagram in Fig. 2.5, within the operating conditions presented in this work, volume viscosities for argon are negligible compared to shear viscosities. Therefore, away from the critical isotherm and the critical isopycnal the acoustic damping rate can be simplified by the classical acoustic damping rate Γ_c, see equation (2.15).

Transient grating spectroscopy with wave fronts of infinite extend has been applied by Li et al. [57] to investigate acoustic damping rates in pure fluids for pressures up to 2.5 MPa at room temperature. Measurements have been conducted in argon, nitrogen, carbon dioxide, methane, and ethylene. Comparing the measured acoustic damping rates with its classical counterpart, Li et al. [57] have observed a linear increase of the acoustic damping rate ratio Γ/Γ_c with pressure for all fluids except ethylene. In fact, the latter has shown an exponential increase. The slope of the linear increase depends on the investigated fluid. The difference in acoustic attenuation has been related by Li et al. [57] to the molecular structure of the fluids and the internal relaxation times. The latter is associated with the volume viscosity. The concept of volume viscosity has been first introduced by Tisza [112] as an explanation for the discrepancy between classical sound absorption applying Stokes' hypothesis and experimental investigations. Hence, as shown by Herzfeld and Litovitz [44], the volume viscosity μ_v is expressed by the difference of the acoustic damping rate Γ and its classical counterpart Γ_c.

$$\mu_v = 2\,\varrho\,(\Gamma - \Gamma_c) \tag{2.16}$$

With equation (2.16) the volume viscosity can be computed by acoustic damping rates Γ_{LITA} extracted using LITA together with theoretical values for the classical acoustic damping rate $\Gamma_{c,\mathrm{NIST}}$ computed with data taken from the NIST database by Lemmon et al. [56].

2.2.1 Acoustic attenuation in complex fluids

As previously discussed and summarised in the work of Ejakov et al. [27], acoustic attenuation in complex fluids is caused by viscous dissipation (μ_s), heat conduction (κ), and molecular relaxation processes (μ_v). Depending on the molecular structure, the vibrational and/or rotational degrees of freedom can be excited by an induced acoustic wave with a specific frequency to pressure ratio leading to additional losses and an increase in acoustic attenuation. The latter has been experimentally observed by Shields [94, 95] in carbon dioxide for dilute gas conditions at various temperatures. The peak in acoustic attenuation is hereby temperature dependent [94, 95]. Moreover, studies in halogen gases at low pressure conditions by Shields [96] show an increased acoustic attenuation at a species specific frequency to pressure ratio. Experimental investigations in gas mixtures with nitrogen at pressures up to 3 MPa have been investigated by Ejakov et al. [27]. They experimentally observed an acoustic frequency–pressure ratio dependent increase in acoustic absorption for nitrogen mixed with molecular complex species, such as methane and carbon dioxide, while nitrogen, hydrogen, oxygen, and oxygen–nitrogen mixtures did not show such a behaviour [27].

The peak in acoustic attenuation at a specific acoustic frequency–pressure ratio is hereby evaluated by the dimensionless acoustic absorption coefficient per wavelength α_λ. Following the mathematical derivation by Herzfeld and Litovitz [44] the coefficient α_λ can be expressed as

$$\alpha_\lambda = \frac{4\,\pi^2\,\nu_a}{{c_s}^2} \varGamma \ , \tag{2.17}$$

where the frequency of the acoustic wave is indicated with ν_a. The acoustic absorption coefficient per wavelength α_λ over the logarithmically scaled acoustic frequency–pressure ratio ν_a/p is called attenuation spectrum. In case of additional acoustic attenuation due to an excitation of molecular degrees of freedom, this leads to a bell–shaped attenuation spectrum.

2.2.2 Volume viscosity models for dilute gases

Theoretical models for the estimation of volume viscosities or simulation data in noble gases have been presented for both liquids (Borgelt et al. [12], Chatwell and Vrabec [16], Fernández et al. [29], and Meier et al. [62]) and gases (Borgelt et al. [12] and Meier et al. [62]). Experimental investigations in noble gases near the triple point have been conducted by Malbrunot et al. [59] and studies in liquid argon by Naugle et al. [67] using ultrasonic sound attenuation. However, the applied theoretical models assume Lennard–Jones fluids and are limited by the molecular structure of noble gases. Since noble gases have no rotational and vibrational degrees of freedom, experimental and computed volume viscosities are solely a result of relaxation based on molecular interactions among the particles translational motion. Concordantly, an application to complex fluids is not feasible, since a consideration of internal relaxation processes is not possible. Moreover, theoretical models and experimental data for validation remain sparse for complex gases.

Experimental investigations for the estimation of volume viscosities using spontaneous Rayleigh–Brillouin scattering have been performed by Shang et al. [91, 92] in nitrogen, oxygen, air and carbon dioxide at dilute gas conditions with pressures up to 0.7 MPa. Moreover, temperature dependencies of the volume viscosity in nitrogen have been determined with spontaneous Rayleigh–Brillouin scattering and pressures up to 0.34 MPa by Gu and Ubachs [37]. A non–equilibrium molecular dynamic approach for the calculation of volume viscosities in dilute gases has been proposed by Sharma and Kumar [93] and applied to nitrogen.

Based on the framework of Tisza [112] a theoretical model for volume viscosities in dilute gases has been introduced by Cramer [17]. Cramer [17] proposed an uncoupled model for the vibrational and rotational modes of relaxation. Hence, the volume viscosity $\mu_{v,\mathrm{Cramer}}$ is estimated as the superposition of both contributions as shown by equation (2.18)

$$\mu_{v,\mathrm{Cramer}} = \mu_{\mathrm{rot,Cramer}} + \mu_{\mathrm{vibr,Cramer}} \ , \tag{2.18}$$

where the rotational and vibrational contribution is indicated with μ_{rot} and μ_{vibr}, respectively. This uncoupled approach, however leads to an overprediction in volume viscosity for carbon dioxide at low temperature conditions. The latter will be discussed in the following and is presented in Fig. 2.9.

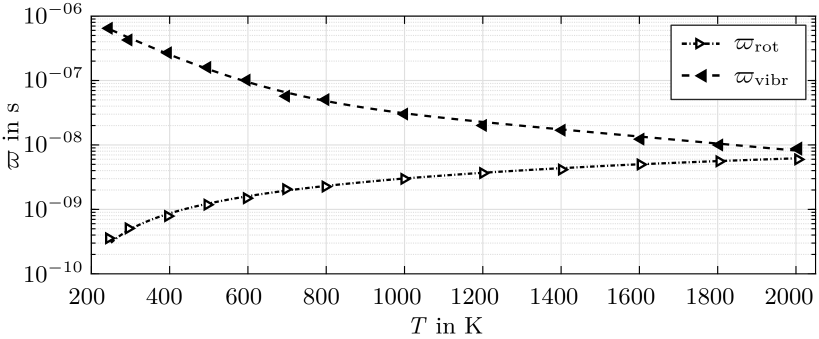

Figure 2.6: Temperature dependency of relaxation times of vibrational and rotational degrees of freedom for pure carbon dioxide at $p = 0.1\,\mathrm{MPa}$. Data are taken from Kustova et al. [51].

As discussed by Kustova et al. [51], the considerable overprediction in volume viscosity in the model by Cramer [17] is a result of the large vibrational relaxation times at temperature up to 800 K, see Fig. 2.6. Since the vibrational modes are essentially frozen at low temperature conditions, excitement of the vibrational degrees of freedom is unlikely. Concordantly, they do not influence the volume viscosity. This is, however, not captured in the dilute gas model by Cramer [17]. To incorporate this dependency, Kustova et al. [51] developed a coupled one–temperature model for carbon dioxide at dilute gas conditions, which considers the interdependency of the vibrational relaxation time ϖ_vibr and the rotational relaxation time ϖ_rot:

$$\mu_{v,\mathrm{Kustova}} = p\,R \left(\frac{c_\mathrm{inter}}{c_v}\right)^2 \left(\frac{c_\mathrm{rot}}{\varpi_\mathrm{rot}} + \frac{c_\mathrm{vibr}}{\varpi_\mathrm{vibr}}\right)^{-1} \tag{2.19}$$

The rotational contribution of the specific isochoric heat capacity c_v is indicated by c_rot, while the vibrational part is c_vibr. The combined internal contribution to the specific heat is $c_\mathrm{inter} = c_\mathrm{rot} + c_\mathrm{vibr}$. Additionally, the pressure is indicated with p and the specific gas constant is R. Note that the model by Kustova et al. [51] is restricted to dilute gases, since intermolecular interactions are not considered.

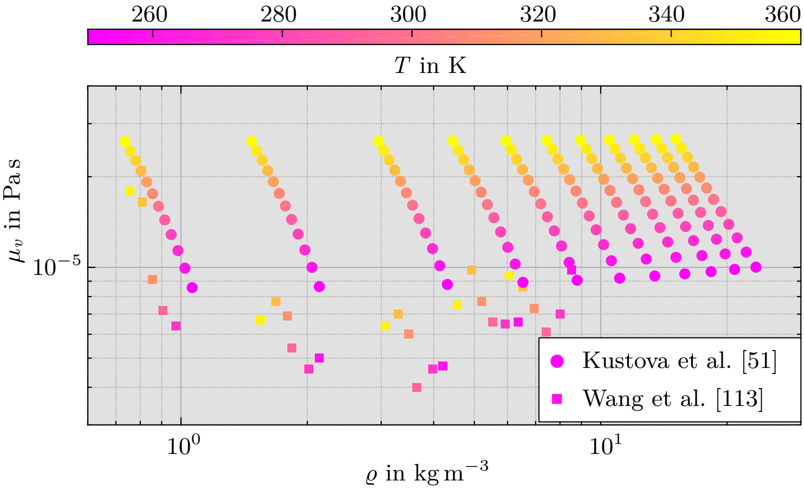

Figure 2.7: Experimental and theoretical volume viscosity μ_v over density for pure carbon dioxide at temperatures from 250 to 360 K. Data are calculated using the model for dilute gases by Kustova et al. [51]. For validation, experimental data of Wang et al. [113] are presented. Thermodynamic data are taken from Lemmon et al. [56].

The comparison of volume viscosities in carbon dioxide calculated with the model by Kustova et al. [51] and experimental investigations by Wang et al. [113] using spontaneous Rayleigh–Brillouin scattering at pressures up to 0.4 MPa is depicted in Fig. 2.7. The results agree satisfactorily. This highlights the validity of the coupled modelling approach by Kustova et al. [51]. The observed dependency in pressure is also noteworthy. While equation (2.19) implies linear pressure dependency, the results in Fig. 2.7 are hardly pressure dependent. As discussed by Shields [94], this behaviour is based on the reciprocal pressure dependency of the relaxation times. From a physical standpoint, higher pressures lead to increasing molecular interactions resulting in a faster relaxation [94]. This results in the observed nearly pressure independent volume viscosity. However, this behaviour is only true for dilute gas conditions. Note that similar dependencies in pressure are observed for c_p and β_T. While nearly pressure independent at low density/pressure condition, both c_p and β_T experience strong pressure dependencies at higher pressures. Moreover, as presented in Fig. 1.2, both values experience maxima at the Widom–line. The molecular dynamic simulation by Meier et al. [62] shown in Fig. 2.5 for the monoatomic fluid argon, indicates a similar behaviour for the volume viscosity at nearcritical conditions. Hence, further investigations and theoretical model extension are necessary to account for dense gas effects in dilute gas models. Of particular interest are hereby Widom–line transitions.

2.2.3 Model expansion for the consideration of dense gas effects

Dense gas effects have been taken into account in the framework by Jaeger et al. [46]. Based on a literature review, Jaeger et al. [46] have proposed an uncoupled approach to extend the dilute gas model by Cramer [17] for dense gases. The volume viscosity $\mu_{v,\mathrm{Jaeger}}$ is hereby estimated by the sum of the dense gas contributions $\mu_{v,\mathrm{coll}}$ due to elastic collisions and the dilute gas term $\mu_{v,\mathrm{Cramer}}$ calculated with the model by Cramer [17].

$$\mu_{v,\mathrm{Jaeger}} = \mu_{v,\mathrm{Cramer}} + \mu_{v,\mathrm{coll}} \tag{2.20}$$

The dense gas contribution $\mu_{v,\mathrm{coll}}$ is associated with the energy transfer due to intermolecular collisions. Figure 2.8 shows the contribution on the viscosity ratio $\mu_{v,\mathrm{coll}}/\mu_s$ due to elastic collisions for pure carbon dioxide at 323 K. The values used in the simulation by Jaeger et al. [46] (circle) are simulated with the EPM2 model developed by Harris and Yung [40]. The EPM2 model considers the molecular structure by assuming rigid bond lengths with a flexible angular bond potential. Additionally, results computed with the Lennard–Jones fluid model by Meier et al. [62] (square) are presented. Note that the Lennard–Jones model applied by Meier et al. [62] neglects the molecular structure and bonds in carbon dioxide.

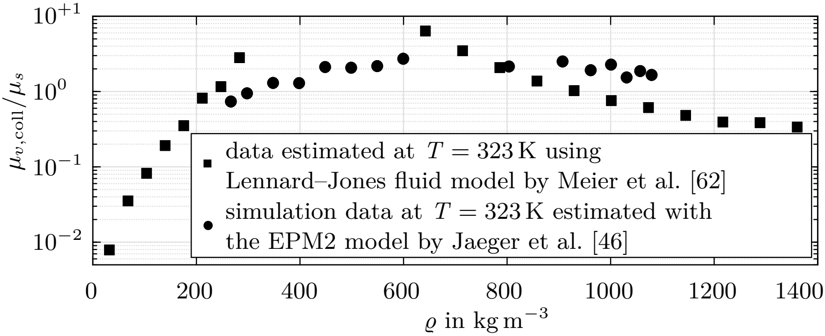

Figure 2.8: Comparison of the viscosity ratio $\mu_{v,\mathrm{coll}}/\mu_s$ due to elastic collisions for pure carbon dioxide at 323 K. Data are extracted from the Lennard–Jones fluid model by Meier et al. [62] and simulations from Jaeger et al. [46] with the EPM2 model by Harris and Yung [40]. Thermodynamic data are taken from Lemmon et al. [56].

Eventhough the model by Meier et al. [62] assumes Lennard–Jones fluids, a general agreement with the EPM2 model is shown. Furthermore at gaseous fluid states ($\varrho < 185\,\mathrm{kg\,m^{-3}}$) the ratio of the viscosity ratio $\mu_{v,\mathrm{coll}}/\mu_s$ increases with density to values close to one. Note that solely based on the estimations of the contribution of elastic collisions, the assumption of negligible volume viscosities compared to shear viscosities no longer holds and Stokes' hypothesis has to be revisited. While the contribution of the volume viscosity $\mu_{v,\mathrm{coll}}$ due to molecular collisions presents values in the same magnitude as the shear viscosity, it is negligible in the computation $\mu_{v,\mathrm{Jaeger}}$. This results from the vast overprediction of the dilute gas contribution $\mu_{v,\mathrm{Cramer}}$ at low temperature conditions due to the modelling approach by Cramer [17].

2.2.4 Comparison of volume viscosity models

Spontaneous Rayleigh–Brillouin scattering studies by Shang et al. [92] and Wang et al. [113] in CO_2 are compared to the dilute gas models by Cramer [17] and Kustova et al. [51] as well as to the simulations by Jaeger et al. [46]. Figure. 2.9 shows the viscosity ratio μ_v/μ_s for carbon dioxide at 300 K over density ϱ. Since theoretical values range over more than four orders of magnitude, the viscosity ratio is scaled logarithmically.

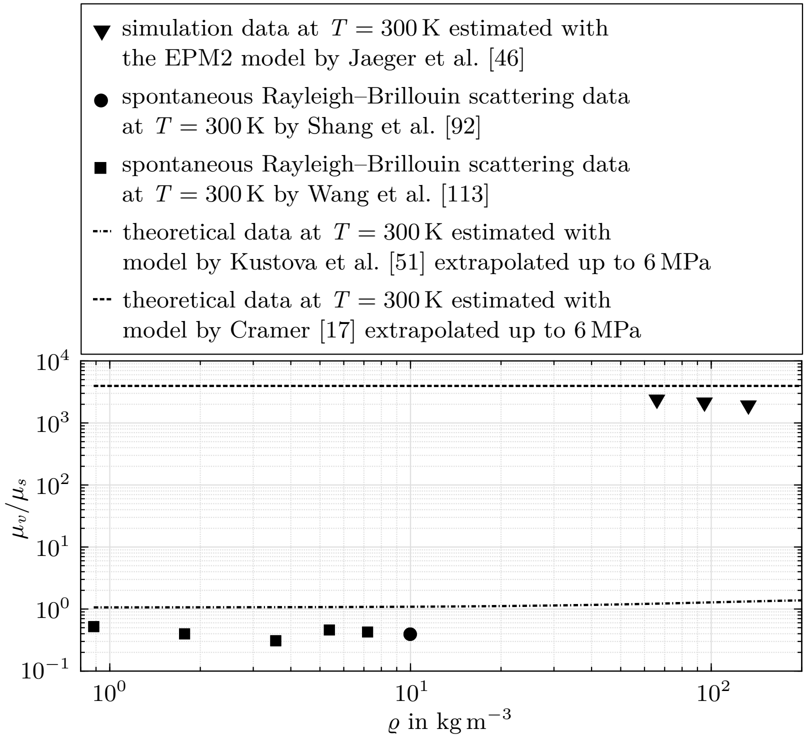

Figure 2.9: Comparison of viscosity ratio μ_v/μ_s for pure carbon dioxide at 300 K with volume viscosity data extracted from different models, simulations, and experimental investigations. Thermodynamic data are taken from Lemmon et al. [56].

The coupled framework by Kustova et al. [51] provides the best agreement with the experimental data by Shang et al. [92] and Wang et al. [113]. The observed discrepancy between the uncoupled model by Cramer [17] and coupled model by Kustova et al. [51] are based on the relaxation times of the vibrational and rotational modes and their interdependence. While the model proposed by Cramer [17] assumes an independence of these relaxation times and estimates the volume viscosity by the superposition of both contributions (see equation (2.18)), the theoretical framework by Kustova et al. [51] takes the interdependence of the relaxation times into account (see equation (2.19)). The latter results in an inverse temperature dependency compared to the model by Cramer [17] for temperatures below 800 K as well as overall lower viscosity ratios. Since the dilute gas contribution in the simulations by Jaeger et al. [46] is based on the model by Cramer [17] (see equation 2.20), the simulation data by Jaeger et al. [46] are close to the theoretical data by Cramer [17]. Note that the decrease in μ_v/μ_s with rising density results hereby from lower values in shear viscosity, as the volume viscosity increases slightly due to the dense gas contribution. Also note that the high viscosity rates in the molecular simulations by Jaeger et al. [46] result from the uncoupled modelling approach by Cramer [17] for dilute gas contribution rather than the simulated molecular interactions ($\mu_{v,\mathrm{coll}}$). It is therefore of great interest to develop a theoretical framework based on the approach by Jaeger et al. [46] using the model by Kustova et al. [51] for the dilute gas contribution. In contrast to the data by Jaeger et al. [46], comparing Fig. 2.8 and Fig 2.9, both contributions have the same order of magnitude. Hence, the dense gas contribution has to be considered.

Unfortunately, as presented in Fig. 2.9, experimental investigations for the validation of volume viscosities at high density/pressure conditions are sparse. The LITA investigations in carbon dioxide performed in the framework of this thesis are designed to close this gap by providing volume viscosity data for pressures between 0.5 and 8 MPa and temperatures up to 600 K.

2.3 Physical aspects of nearcritical droplet evaporation

The understanding of evaporation processes at conditions in the vicinity of the fluids critical point has increasingly become important in order to achieve a stable and efficient combustion. Since the specific entropy production is inversely proportional to the density–temperature product, processes with high operating pressures lead to a reduced entropy production and, hence, a more efficient process, combustion pressures have increased to the point that they exceed the critical values of the injected fluids. However, mixing and evaporation processes at near- to supercritical fluid conditions are not yet fully understood. Theoretical investigations on the onset of dense fluid mixing processes have been conducted by various research groups using different criteria. The pseudo–boiling criterion has been developed by Banuti and co–workers (Banuti [7] and Banuti et al. [9]). It operates under the assumption of a supercritical pseudo–boiling transition crossing the Widom–line similar to classical evaporation processes. In contrast, the criteria by Dahms [23] and Qiu and Reitz [84] are based on a global thermodynamic equilibrium approach assuming adiabatic mixing to estimate the droplets temperature. The onset of dense fluid mixing has been predicted by Qiu and Reitz [84] with the critical locus criterion comparing the droplets state with the corresponding critical properties of the mixture. The Knudsen criterion by Dahms [23] applies a length–scale analysis comparing the thickness of the interface layer with the mean–free path of thermal diffusion in the vapour phase. A detailed discussion on the drawbacks and validity of these criteria has been presented by Lamanna [54], while the selection of boundary conditions for evaporation processes at high pressure and temperature conditions has been discussed by Stierle et al. [110]. Besides theoretical studies, experimental investigations of dense fluid mixing processes have been conducted by different research groups (Baab et al. [5, 6], Crua et al. [18], Falgout et al. [28], Förster et al. [32], and Gerber et al. [33]). Nevertheless, quantitative data for validating numerical and theoretical evaporation models at near- to supercritical conditions remain sparse and present a growing research objective (Bork et al. [14], Mo and Qiao [63], Nomura et al. [68], Preusche et al. [81], and Qiao et al. [83]).

Experimental investigations on the phenomenology of a preheated acetone droplet injected into a supercritical atmosphere have been performed by Weckenmann [116]. By applying shadowgraphy and diffuse lighted imaging the evaporation process and the material interface have been visualised. The investigations by Weckenmann [116] indicate that the acetone droplet remains subcritical when injected into a supercritical atmosphere with respect to the injectant. However, since the shadowgrams and the diffuse lighted images have been conducted with different optical setups under slightly different operating condition a direct comparison is not possible. To close this gap Steinhausen et al. [104] has developed front lighted shadowgraphy. The latter is an optical arrangement combining both shadowgraphy and diffuse lighted imaging resulting in a direct overlay of both results with the same optical setup. The interface of the droplet is hereby detected by reflections and refractions of incoming light on the droplet surface, while direct shadowgraphy in parallel light visualises changes in density gradients, as referred by Settles [90].

Figure 2.10 depicts front lighted shadowgrams of an evaporating free falling n–pentane droplet in a nitrogen atmosphere at four different time steps. The time stamp on the left upper corner is hereby the time, after droplet detachment. Investigations have been conducted with the test facility and the front lighted shadowgraphy setup presented by Steinhausen et al. [104]. The reduced atmospheric temperature is $T_{r,\mathrm{ch}} = 1.11$ at an reduced pressure of $p_{r,\mathrm{ch}} = 1.78$. Prior to injection the droplet is preheated to $T_{r,\mathrm{d}} = 0.95$. Note that the reduced conditions are with reference to the critical values of n–pentane.

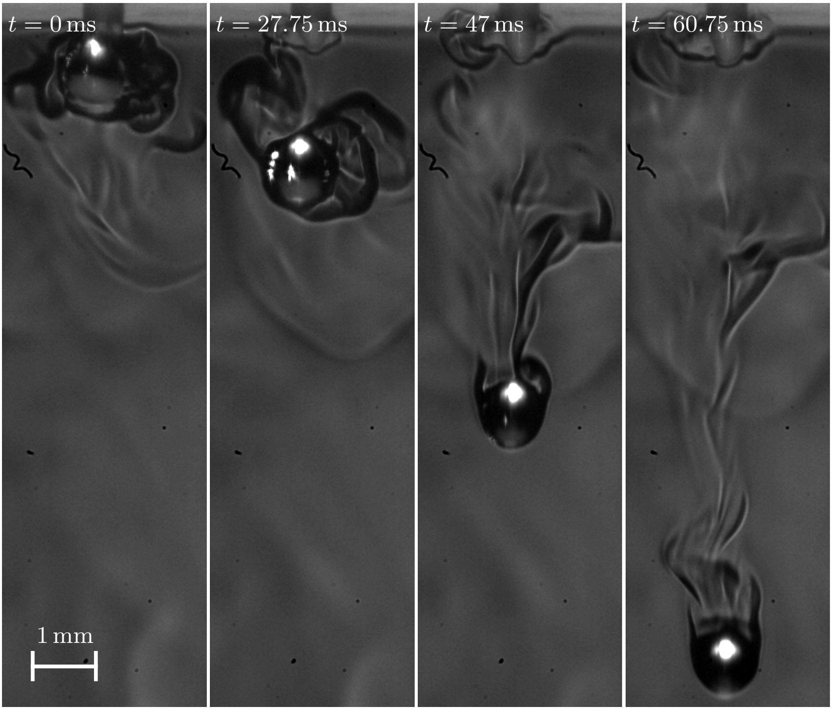

Figure 2.10: Front lighted shadowgrams at four time steps of a free falling n–pentane droplet evaporating in a nitrogen atmosphere at super–critical conditions. Reduced operating conditions: $T_{r,\mathrm{d}} = 0.95$; $T_{r,\mathrm{ch}} = 1.11$; $p_{r,\mathrm{ch}} = 1.78$. Shadowgram data have previously been presented by Steinhausen et al. [104] and Lamanna et al. [53].

As discussed by Steinhausen et al. [104], the front lighted shadowgrams depicted in Fig 2.10 indicate a classical two–phase evaporation, eventhough the preheated fluid is injected into a supercritical atmosphere. While changes in density gradients are displayed by different shades of grey, the material interface is indicated by refractions and reflection on the droplets surface. The latter results from the sensitivity to phase boundaries of the diffuse lighted imaging technique. However, a transition from classical two–phase evaporation to dense fluid mixing is always accompanied by a dissolution of the material interface. Concordantly, reflections and refractions on the droplet surface vanish. A supercritical fluid cluster will consequently lack clear signs of reflection or refractive glare points compared to a subcritical droplets. The explanation for the observed subcritical evaporation process lies in the evaporative cooling of the droplet mitigating the heat fluxes from the supercritical atmosphere into the droplet. It is important to emphasise that as presented by Steinhausen et al. [105] and discussed in detail by Lamanna [54] the temporal evolution of the droplet temperature and its thermodynamic state depends on a complete flux scheme according to a non–equilibrium framework, such as the Onsager theory. Only by applying such a non–equilibrium framework in form of the evaporation model by Young [119] the experimental database by Crua et al. [18] could be reproduced in the work of Lamanna [54].

2.3.1 Estimation of the temperature–concentration field in the wake of an evaporating droplet

The concentration field in the wake of free falling n–hexane and acetone droplets evaporating in a nitrogen atmosphere has been examined by Bork [13] using spontaneous Raman scattering with planar imaging. The investigations by Bork [13] measure the local concentration and the local relative number density in a planar field in the wake of the droplet. Based on both values the concentration–temperature field in the droplet wake can be estimated. As to that a relation between relative number density, concentration, and temperature is necessary. As discussed by Lamanna et al. [53] the advection–governed mixing process in the droplets wake supports an adiabatic mixing assumption relating the measured local properties to the local temperature of the mixture.

Based on the Raman scattering results by Bork [13] of a preheated n–hexane droplet evaporation in a nitrogen atmosphere, the concentration–temperature field is computed by Steinhausen et al. [106] and compared to numerical results from the evaporation model in the direct numerical simulation framework free surface 3D (FS3D). To that purpose the perturbed–chain statistical associating fluid theory (PC–SAFT) equation of state (EoS) developed by Gross and Sadowski [36] has been applied assuming adiabatic mixing. The results are depicted in Fig. 2.11. Note that the numerical boundaries have been selected based on the operating conditions of $p_\infty = 6\,\mathrm{MPa}$ and $T_\infty = 473.15\,\mathrm{K}$ in the nitrogen atmosphere and $T_\mathrm{d} = 473.15\,\mathrm{K}$ as fluid temperature prior to droplet injection. Comparison of the values based on the Raman scattering data (black dots) with the simulation data using FS3D (red dot) shows good agreement. Hence, the adiabatic mixing assumption is additionally verified by the numerical results.

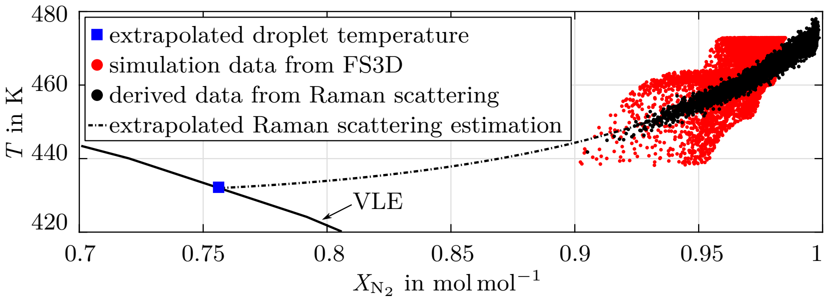

Figure 2.11: Comparison of experimental, numerical, and theoretical concentration–temperature data in the wake of a free falling n–hexane droplet evaporating in a N_2 atmosphere. Dash–dotted line: PC–SAFT–based curve fit to Raman scattering data; Blue dot: extrapolated droplet temperature; Experimental and numerical conditions: $p_\infty = 6\,\mathrm{MPa}$, $T_\infty = 473.15\,\mathrm{K}$; $T_\mathrm{d} = 473.15\,\mathrm{K}$; $r_{\mathrm{d},t=0.5\,\mathrm{s}} = 0.625\,\mathrm{mm}$. Adapted from Steinhausen et al. [106].

By extrapolating the Raman scattering based concentration–temperature field the droplets temperature is estimated. For this purpose an adiabatic mixing curve is fitted to the Raman scattering based data with the PC–SAFT EoS.

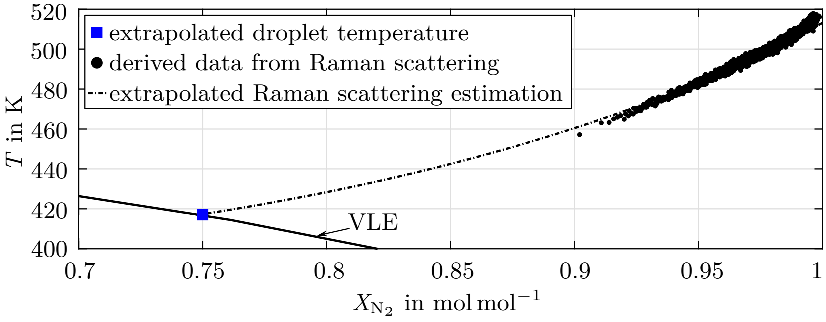

Figure 2.12: Concentration–temperature data in the wake of a free falling acetone droplet evaporating in a N_2 atmosphere. Blue dot: extrapolated droplet temperature; Dash–dotted line: PC–SAFT–based curve fit to Raman scattering data; Experimental conditions: $p_\infty = 6\,\mathrm{MPa}$, $T_\infty = 513.15\,\mathrm{K}$; $T_\mathrm{d} = 453.15\,\mathrm{K}$; $r_{\mathrm{d},t=1\,\mathrm{s}} = 0.7\,\mathrm{mm}$. Data have been presented by Preusche et al. [81].

Based on this extrapolated Raman scattering estimation (dash–dotted line), the extrapolated Raman temperature (blue square) is computed by the intersection with the vapour equilibrium curve (VLE). The temperature estimation confirms an evaporative cooling of the droplet, leading to a subcritical classic evaporation of the droplet as well as a subcritical mixing process in the droplet wake. Preusche et al. [81] have used this framework to evaluate Raman scattering results by Bork [13] of an acetone droplet evaporating in a nitrogen atmosphere. The droplet is hereby preheated to $T_{\mathrm{d}} = 453.15\,\mathrm{K}$, while the pressure and temperature of the nitrogen atmosphere are $p_\infty = 6\,\mathrm{MPa}$ and $T_\infty = 513.15\,\mathrm{K}$. The results are displayed in Fig. 2.12. As for the n–hexane case, the temperature estimation for acetone indicate a subcritical evaporation and subsequent mixing process.

2.3.2 Modelling the droplet temperature and its temporal evolution

The temporal evolution of the droplet temperature can be computed using modelling approaches, such as the theoretical framework by Abramzon and Sirignano [2], Gyarmathy [38], or Young [119]. While the model by Abramzon and Sirignano [2] is a classic hydrodynamic model commonly used in numerical simulation, the frameworks by Gyarmathy [38] and Young [119] are Langmuir–type models. The latter take the kinetic effects in the Knudsen layer around the droplet into account. However, based on the used velocity distribution functions (VDF) only the model by Young [119] is a non–equilibrium model and complies with the Onsager theory for simultaneous heat and mass fluxes. As discussed in the work by Lamanna [54], due to its non–equilibrium approach and the possibility to consider kinetic effects, the evaporation model by Young [119] is applied to estimate the temporal evolution of droplets injected into a supercritical atmosphere. Figure 2.13 shows a schematic representation of the droplet evaporation process. On the left side the fluxes across the interface are shown together with the radial distribution of both the temperature T and the vapour mole fraction X_{v}, whereas the right side shows the Langmuir's Knudsen layer in direct vicinity of the droplet based evaporation model by Young [119]. Saturated conditions are hereby indicated by the subscript $_{\mathrm{s}}$, while conditions in the far field are presented with $_\infty$. The droplet radius is r_{d}, the radius of the Knudsen layer r_{kn}, and the mass and energy fluxes are $\dot{m}$ and $\dot{E}$, respectively. As can be seen, the VDF of the incoming vapour molecules is a Grad distribution [119], whereas the outgoing molecules are modelled by a half–Maxwellian VDF. Note that a temperature jump within the collision–free zone may be observed.

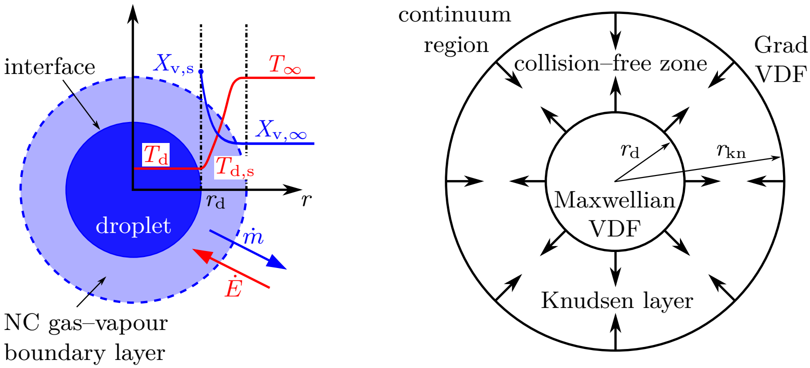

Figure 2.13: Schematic representation of the droplet evaporation process. **Left:** Evaporating droplet with radial distribution of mole fraction X and temperature T embedded in a non–condensible (NC) gas–vapour boundary layer. **Right:** Langmuir's Knudsen layer based evaporation model by Young [119]. Representations are adapted from Lamanna [54].

The evaporation model by Young [119] is applied to determine the temporal evolution of droplet radius and temperature under the operating conditions of the Raman results presented in Fig. 2.12. Since most of the evaporation occurs with the droplet anchored at the capillary, only natural convection effects are considered. For this purpose the correlations by Pinheiro and Vedovoto [76] are applied. Since thermodynamic data for more advanced diffusion models are not available, the binary diffusion coefficient is computed using the model by Wilke and Lee [117]. However, as presented by Palmetshofer et al. [73], the selection of diffusion models only shows a minor influence at the investigated conditions. Additionally, solubility effects of nitrogen into acetone are considered. Note that the dwell time of the droplet prior to Raman scattering investigation is 1 s. The initial droplet radius is iteratively determined to agree with the experimental observations by Preusche et al. [81]. A comparison of the resulting temporal evolution of droplet temperature and radius are depicted together with the Raman scattering based droplet temperature (blue dot) in Fig. 2.14. Furthermore, the droplet evolution computed with the model by Young [119] (black line) is compared to investigations using laser–induced fluorescence phosphorescence (LIFP) by Preusche et al. [81] (green and red triangle with error bars) measured at two different positions below the capillary at equal operating conditions.

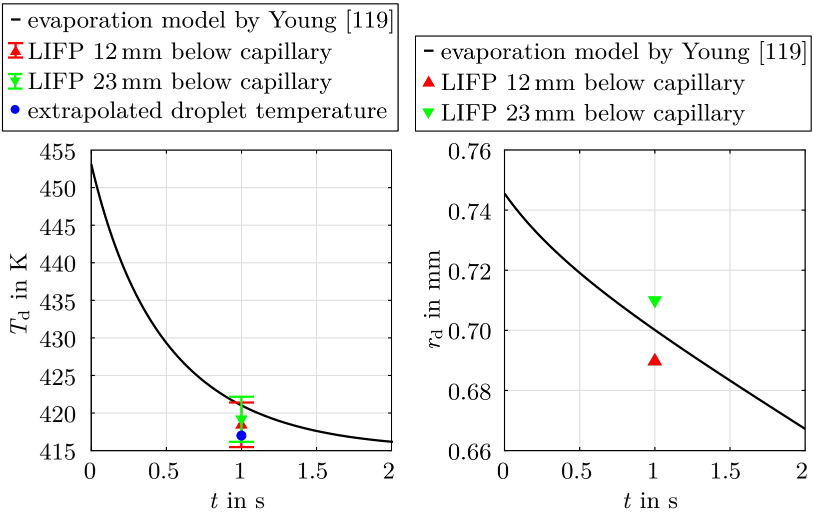

(a) Droplet temperature over time. (b) Droplet radius over time.

Figure 2.14: Temporal evolution of droplet temperature and size of a free falling acetone droplet in a nitrogen atmosphere. Experimental conditions: $p_\infty = 6\,\mathrm{MPa}$, $T_\infty = 513.15\,\mathrm{K}$; Test fluids: acetone in nitrogen, initial temperature: $T_\mathrm{d} = 453.15\,\mathrm{K}$, far–field acetone mole fraction: $X_{\mathrm{Ac},\infty} = 0.0051\,\mathrm{mol\,mol^{-1}}$, droplet radius: $r_{\mathrm{d},t=1\,\mathrm{s}} = 0.7\,\mathrm{mm}$. LIFP and Raman scattering data are taken from Preusche [82].

Both the Raman scattering based extrapolated temperature and the evaporation model by Young [119] agree well with the LIFP results. The implications of this validation is twofold. First, the adiabatic mixing assumption used to estimate the temperature–concentration field is valid for the observed evaporation process. Second, the evaporation model by Young [119] together with the applied corrections is appropriate to predict the temperature evolution of the droplet. Concordantly, the time–resolved LITA measurements conducted in the wake of a free falling acetone droplet in a nitrogen atmosphere presented in section 6.3, are evaluated based on the advection controlled mixing model applied to compute the data in Fig. 2.12. With this model the local state of the mixture (T_mix and X_mix) can be estimated based on the speed of sound data calculated from LITA measurements.

CHAPTER 3

Experimental facility and optical arrangements

The investigations presented in this thesis comprise measurements in pure fluids, predefined mixtures, droplet evaporation, and gaseous jet mixing processes. These experiments are all performed in well known quiescent conditions. A temperature, pressure, and flow controlled high–pressure–high–temperature chamber with a modular top design is used for all presented studies. Macroscopic fluid properties, such as speed of sound and acoustic damping rate, are detected by applying laser–induced thermal acoustics, whereas the flow for the gaseous jet mixing processes is visualised using the schlieren technique. At last, the investigated droplet evaporation process is observed by shadowgraphy. The following chapter presents in detail the experimental facility together with the optical arrangement used for quantitative fluid measurements and flow visualisation.

3.1 Experimental facility for fluid phenomena studies

Experimental investigations are performed in a heatable, pressure, and flow controlled high–pressure–high–temperature chamber. The latter is designed for phenomenological and statistical investigations of evaporating free–falling droplets in a nearcritical environment. The droplet on demand system on top of the chamber can be replaced by a closed lid for operation as homogeneous flow reactor for calibration purposes or by an expansion module with a small orifice for investigating gaseous jet mixing processes. The experimental facility is mounted on a *xyz*–traversal stage. The vertical placement of the chamber is hereby realised by two linear drives with stepper motors (LF–series, isel Germany AG). The positioning error in x and y–direction is determined by the smallest step, which yields an error of ±12.5 µm. Due to the chamber weight the z–position is adjusted using a hydraulic platform (TL 1000B, EdmoLift Hebetechnik GmbH), controlled and measured by a draw-wire sensor (WDS–1000–P60, Micro–Epsilon Messtechnik GmbH & Co. KG). Due to the compressibility of the hydraulic fluid the positioning error in z–direction is approximately ±150 µm.

For calibration and validation purposes four different pure atmospheres, namely nitrogen (N_2), argon (Ar), carbon dioxide (CO_2), and helium (He) are studied. Additionally, five different predefined binary gas mixtures are investigated. In particular two argon–helium mixtures, a argon–nitrogen, a argon–CO_2, and a nitrogen–CO_2 mixture are used for the validation of the LITA technique. Droplet evaporation studies are performed in a nitrogen atmosphere. Acetone (Ac) for spectroscopic purposes (product line Uvasol®) is used as liquid. Gaseous jet mixing is investigated in an argon jet in a nitrogen atmosphere. In Tab 3.1 all used fluids, their purity, concentrations, and suppliers are listed.

Table 3.1: Overview of used gases, predefined binary gas mixtures, and liquids.

fluid	purity in %	mole fraction	supplier
nitrogen	99.999	N/A	Widmann Gase GmbH
argon	99.998	N/A	Widmann Gase GmbH
carbon dioxide	99.995	N/A	Widmann Gase GmbH
helium	99.996	N/A	Widmann Gase GmbH
argon–helium	99.998 / 99.996	0.2000 / 0.8000	Widmann Gase GmbH
argon–helium	99.999 / 99.999	0.9000 / 0.1000	Air Liquide SA
argon–nitrogen	99.999 / 99.999	0.8000 / 0.2000	Air Liquide SA
argon–CO_2	99.999 / 99.995	0.8000 / 0.2000	Air Liquide SA
nitrogen–CO_2	99.999 / 99.995	0.7999 / 0.2001	Air Liquide SA
acetone	99.9	N/A	Merck KGaA

In the following paragraph the design of the high–pressure–high–temperature chamber, its different lids as well as the fluid supply and pressure control system is presented.

3.1.1 High–pressure–high–temperature chamber in closed lid design

Horizontal and vertical sections of the high–pressure–high–temperature chamber with the closed lid are depicted in Fig. 3.1. The chamber is build with heat–resistant stainless steel (EN-1.4913). It is designed for pressures up to 8 MPa at temperatures up to 773 K. The pressure vessel encloses a cylindrical core 40 mm in diameter and a height of 240 mm. Based on the design of the top and bottom lid an annular orifice (A) of 0.5 mm in width is located on the inlet and outlet of the cylindrical core. These circumferential slits are used to guide the atmospheric gas into and out of the measurement volume inside the chamber. Top and bottom lid are sealed using metallic O-Rings (O; Willis Ring®, Trelleborg Sealing Solutions Germany GmbH). For optical accessibility eight ultra violet (UV)–transparent quartz windows (W) are placed at two different heights with an angle of 90° to each other. The windows are at least of Suprasil 2 Grade A quality, concordantly they exhibit a functional optical direction orthogonal to the windows transmission surface. Sealing of the windows is achieved by a combination of metallic O-Rings and graphite gaskets (G; novaphit® MST XP, Frenzelit GmbH). For temperature control, eight heating cartridges (H; HLP T, Türk+Hillinger GmbH) are vertically inserted in the chamber body and a heating plate with four cartridges is placed below the chamber. All cartridges are controlled by PID controllers (LTR 4200 and dTRON316, Juchheim GmbH). The latter use type–K thermocouples (K; TC Mess- und Regeltechnik GmbH) in the metal body and the heater cartridges as input parameters. For thermal insulation, a mineral–based silicate (I; SILCA 250 KM) is used around the chamber. The bottom of the heating plate is insulated with a vermiculite plate (V).

The pressure inside the chamber is measured at the chamber exhaust by a temperature–compensated pressure transducer (35 X HTC, Keller Ges. für Druckmesstechnik mbH) with an uncertainty of ± 0.05 MPa. Temperature measurements inside the chamber are located at three different heights with resistance thermometers (T; PT100A, ES Electronic Sensor GmbH) penetrating the metal core. Due to the temperature dependent uncertainty of the resistance thermometers the measurement uncertainties are calculated for each condition according to DIN EN 60751:2009-05 [25] respectively. A detailed description on the measurement uncertainties and characteristics of the experimental facility can be found in the Bachelor thesis of Schaumäker [88]. Both temperature and pressure are logged continuously using LabVIEW 2016 (National Instruments Corp.).

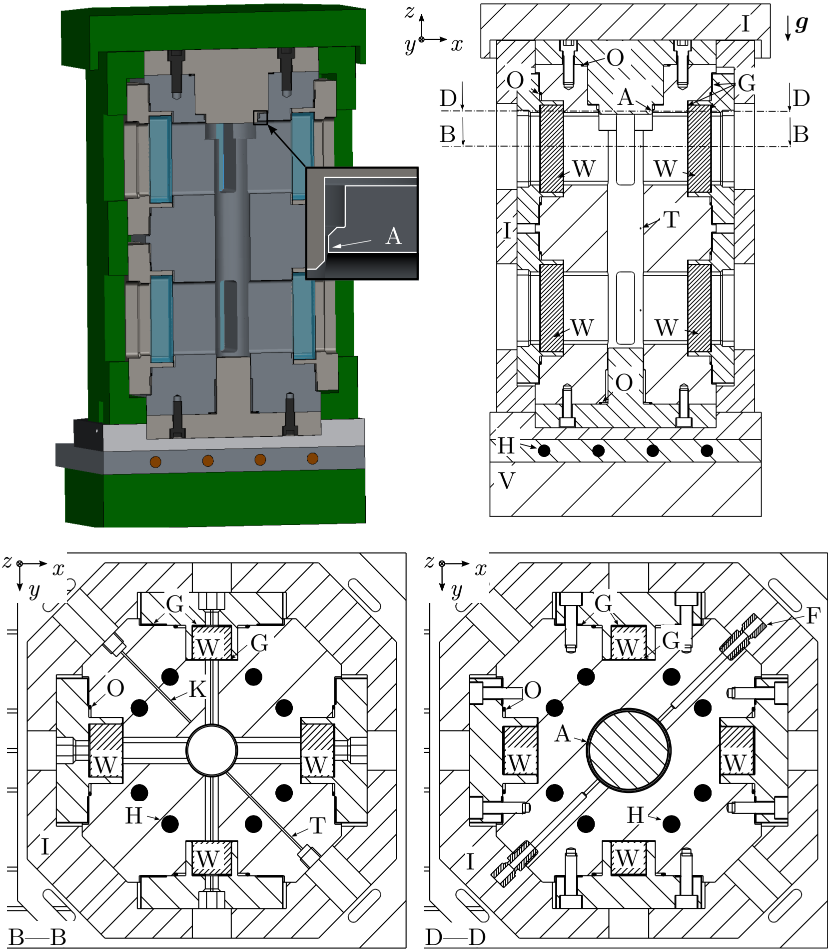

Figure 3.1: Horizontal and vertical sections of chamber. **Upper left:** Cutaway view of chamber with closed lid. **Upper right:** Vertical section through chamber with closed lid. **Lower left (section B—B):** Horizontal section through chamber at centre of first window. **Lower right (section D—D):** Horizontal section through chamber at fluid inlet and annular orifice. A: annular orifice; F: fluid inlet; $\boldsymbol{g}$: gravitational acceleration; G: graphite gaskets; H: heating cartridges; I: thermal insulation; K: type–K thermocouple; O: Willis Ring®; T: resistance thermometer; V: vermiculite plate; W: UV-transparent quartz windows.

3.1.2 Droplet on demand generator

The droplet on demand generator, shown in Fig. 3.2, is mounted in a silicone oil temperature-controlled chamber lid. The droplet generator is thermally and electrically insulated against the chamber body by a ceramic ring (I; Macor) around the lid, flat gaskets (I; Klingersil® C-4430, Klinger GmbH) between lid and chamber body/top and a Teflon insulation (I) on the bottom of the lid around the grounded capillary (C). The latter has inner and outer diameters of 200 and 700 µm, respectively. The Teflon insulation is designed to create an annular orifice (A) with the chamber body as previously described for the closed lid design. The circumferential slit is located below the droplet generator assembly and above the capillary tip, which is used for droplet injection. The rationale of the chosen slit and capillary configuration is to minimise the effects of the constantly purging gas inflow onto the droplet detachment and free–fall.

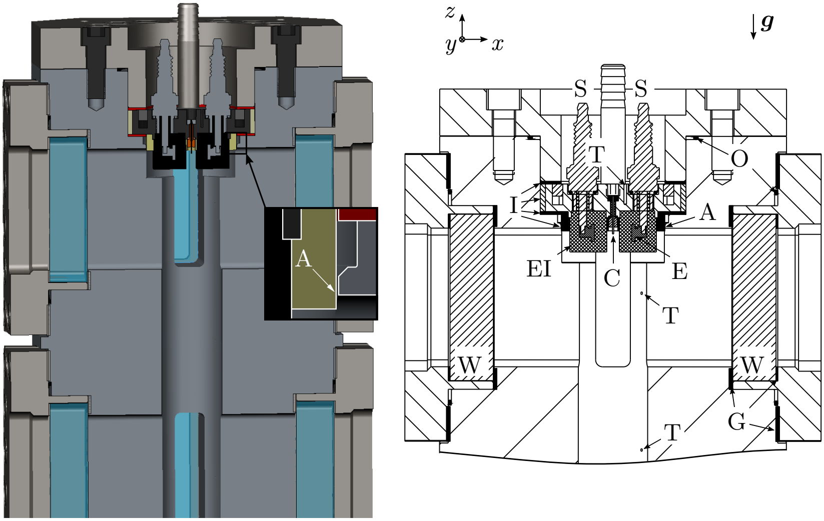

Figure 3.2: Vertical section of mounted droplet generator. **Left:** Cutaway view of chamber with droplet generator. **Right:** Vertical section through chamber with droplet generator. A: annular orifice; C: capillary; E: electrode; EI: electrical insulation; $\boldsymbol{g}$: gravitational acceleration; G: graphite gaskets; I: thermal insulation; O: Willis Ring®; S: spark plug; T: resistance thermometer; W: UV-transparent quartz windows.

The temperature of the droplet generator lid is measured with a resistance thermometer (T; PT100A, ES Electronic Sensor GmbH) in its metal core close to the capillary. As for the resistance thermometers inside the chamber, measurement uncertainties are calculated for each condition according to DIN EN 60751:2009-05 [25]. The droplet on demand assembly is heated and temperature controlled by a silicon oil (Thermofluid P20.275.50, Peter Huber Kältemaschinenbau AG) flow generated by a heating circulation bath thermostat (CC-202C, Peter Huber Kältemaschinenbau AG). The temperature for the investigation presented in this thesis is limited to a maximum of 473 K by the available bath thermostat. Note that the used materials are designed for temperatures up to 573 K.

Droplets anchored at the capillary are detached by initiating an electric force between the fluid due to a strong, pulsed electric field in the vicinity of the droplet. The electric field is generated by two copper electrodes (E), screwed in the central electrode of spark plugs (S; DCPR6E, NGK). To prevent an electric breakdown of the surrounding atmosphere, the electrodes are cast in an epoxy–based temperature and acetone resistant glue (EI; Duralco® 4700 HT, Polytec PT GmbH). To avoid interferences between the pulsed electric field and the detectors, sensors, and oscilloscopes, opto–isolators (AD–TV 810 GS, Adamczewski GmbH) are used in the wiring. Moreover, laying the connecting cables is done with great care.

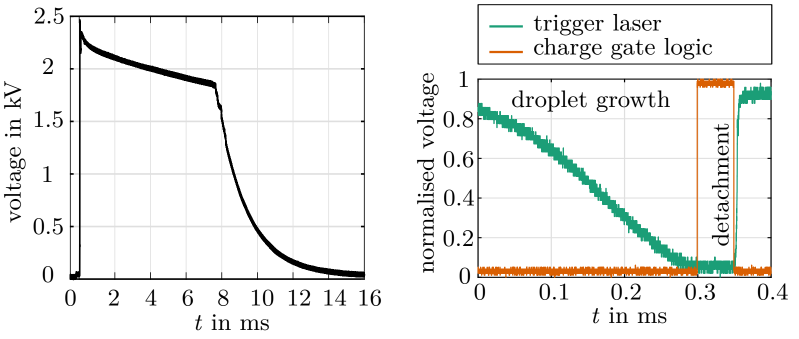

(a) High voltage probe measurements. Power supply is set to 4 kV, with a pulse length of 8 ms.

(b) Detachment laser barrier occlusion measurement. Image is adapted from Preusche [82].

Figure 3.3: Oscilloscope trace of high voltage pulse measured at one electrode and laser light barrier detector (D8) used for triggering.

Figure 3.3a depicts voltage measurements taken at one electrode with a high voltage probe and an oscilloscope (Waverunner 400Xi, Teledyne LeCroy). The pulse length is hereby set to 8 ms, with the power supply set to 4 kV. As it is evident from the measurements, the voltage of the power supply cannot be reached. This is due to the capacities of the electrical setup, which is designed to achieve equal capacities for droplet generator and capacitor. The latter is charged by the power supply prior to droplet detachment. Bork [13] presents a detailed description of the electrical setup together with the timing characteristics of the pulse generation unit.

Droplet detachment is triggered, when the growing droplet crosses a laser light barrier generated by a fibre coupled continuous wave (cw) laser with a wavelength of 635 nm (S1FC635, Thorlabs Inc.). The laser beam is focused closely under the capillary and detected by a high–speed silicon detector (D8; DET100A/M, Thorlabs Inc.), as shown in Fig. 3.13. To avoid interferences a laser–line filter for the light barrier operating wavelength is mounted in front of the detector. As an example the measurements conducted by Preusche [82] depicted in Fig. 3.3b show the normalised voltage signal of the detector (D8) used for triggering. Two phases are displayed. First the droplet grows over time until the threshold for triggering the detachment is reached. After the electric pulse the droplet detaches. Note that since the pulse ends prior to the detachment no residual electric charge remains. The influence of the applied voltage on the droplet's acceleration in z–direction is presented by Preusche [82]. A selection of shadowgrams of acetone droplets in a nitrogen atmosphere taken directly after detachment is presented in Fig. 3.4.

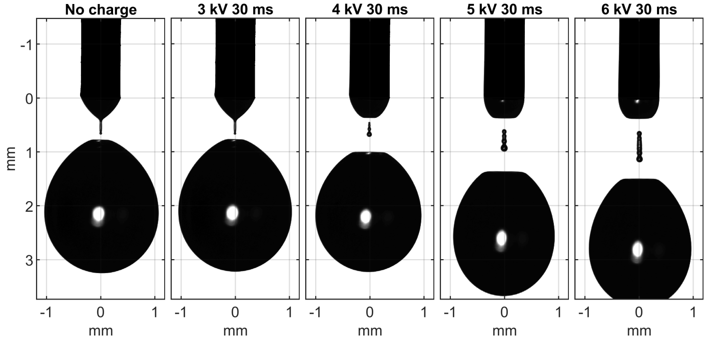

Figure 3.4: Parametric study on detachment charge for acetone droplets in a nitrogen atmosphere at 300 K and 0.3 MPa. Image is taken from Preusche [82].

A significant acceleration is observed for a power supply voltage of 4 kV, which increases with increasing voltage. A detailed characterisation of droplet detachment at low pressure (0.3 MPa) and temperature (300 K) conditions is presented by Preusche [82]. Investigations on the droplet free fall and the induced oscillations of acetone droplets in a nitrogen atmosphere at nearcritical chamber conditions conducted by Weckenmann et al. [114] and Oldenhof et al. [69] have proven the reproducibility of the detachment concept at high pressure and temperature conditions. A numerical study of the detachment principle as well as the underlying physics is presented by Ouedraogo et al. [72].

3.1.3 Expansion module for jet mixing processes

The design of the expansion module for jet mixing processes is based on the closed lid design. Figure 3.5 shows a vertical section of the mounted jet mixing module. Position and size of the annular orifice (A) as well as the sealing concept are equal to the close lid design described in chapter 3.1.1.

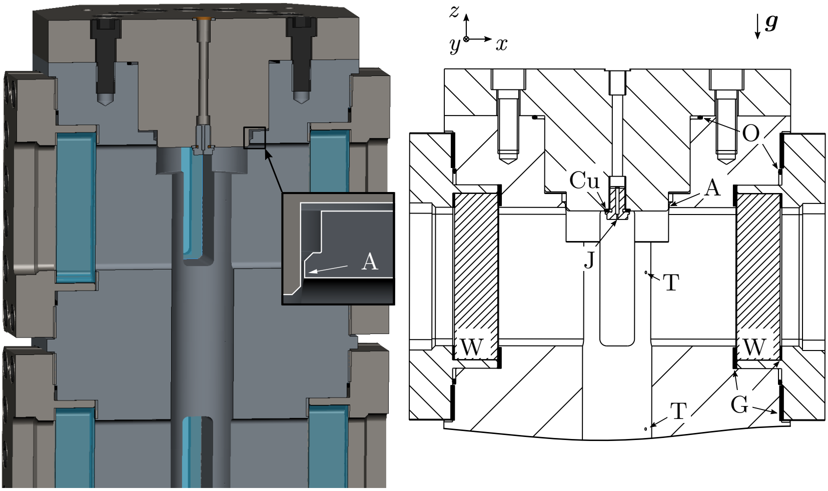

Figure 3.5: Vertical section of the expansion module for jet mixing processes. **Left:** Cutaway view of jet orifice module. **Right:** Vertical section of jet orifice module. A: annular orifice; Cu: cooper sealing; $\boldsymbol{g}$: gravitational acceleration; G: graphite gaskets; J: brazen jet orifice; O: Willis Ring®; T: resistance thermometer; W: UV-transparent quartz windows.

To generate a gaseous jet a copper sealed (Cu) brazen jet orifice (J) with a diameter of 700 µm is concentrically mounted in the lid. Since the investigated gaseous jet mixing processes are solely conducted at room temperature and no heating was applied, temperature measurement of the jet are omitted. Note that the argon mass flow used to generate the jet is in the range of $\dot{m}_{\mathrm{Ar}} = 5.4\,10^{-3}\,\mathrm{kg\,s^{-1}}$, which leads to a mean entrance jet velocity of approximately $w_{\mathrm{Ar}} = 0.2\,\mathrm{m\,s^{-1}}$. Together with the ideal gas behaviour of argon at low pressures, no significant changes in temperature due to the Joule–Thomson effect are anticipated.

3.1.4 Fluid supply and pressure control system

The experimental facility is operated as a continuous flow reactor. The gas supply is provided by pressurised gas cylinders. A schematic drawing of the gas and liquid supply as well as the pressure control system is depicted in Fig. 3.6. The test rig can be operated in a closed loop, indicated in black and blue, and an open loop configuration, indicated in black and green. Note that the closed loop configuration is only applied when operating with pure fluids or predefined mixtures. Particularly, for investigating carbon dioxide atmospheres the closed loop configuration is applied, as it reduces CO_2 emissions. For droplet or jet injection experiments the open loop configuration is used. The fluid supply system for the jet orifice module and droplet generator is highlighted in red.

Liquid test fluids are stored at room temperature in a pressure vessel with edge welded bellows. Due to the welded bellows the fluids are held at constant pressure without any physical contact between fluid and nitrogen, which is used for pressurisation. Hence, solubility effects of nitrogen in the pressurised liquids can be excluded. Fluid pressure is set to approximately 2 MPa above chamber operating pressure. This ensures a stable and reproducible fluid flow controlled by a Coriolis-based mass flow controller (MINI CORI-FLOW™, Bronkhorst High–Tech B.V.) to the droplet generator (DG). In case of the gaseous jet operation/investigation, the fluid tank is bypassed, thereby connecting the argon gas cylinder directly to flow controller upstream of the jet orifice module (JO).

Mass flows of nitrogen, argon and non carbon dioxide mixtures into the chamber are controlled by a heat–capacity based mass flow controller (EL–FLOW®, Bronkhorst High–Tech B.V.). A Coriolis–based mass flow controller (MINI CORI-FLOW™, Bronkhorst High–Tech B.V.) is utilised for carbon dioxide and CO_2–mixtures. Note that carbon dioxide is pressurised beforehand by a pneumatic-driven piston pump (DLE15–2–GG–C, Maximator GmbH).

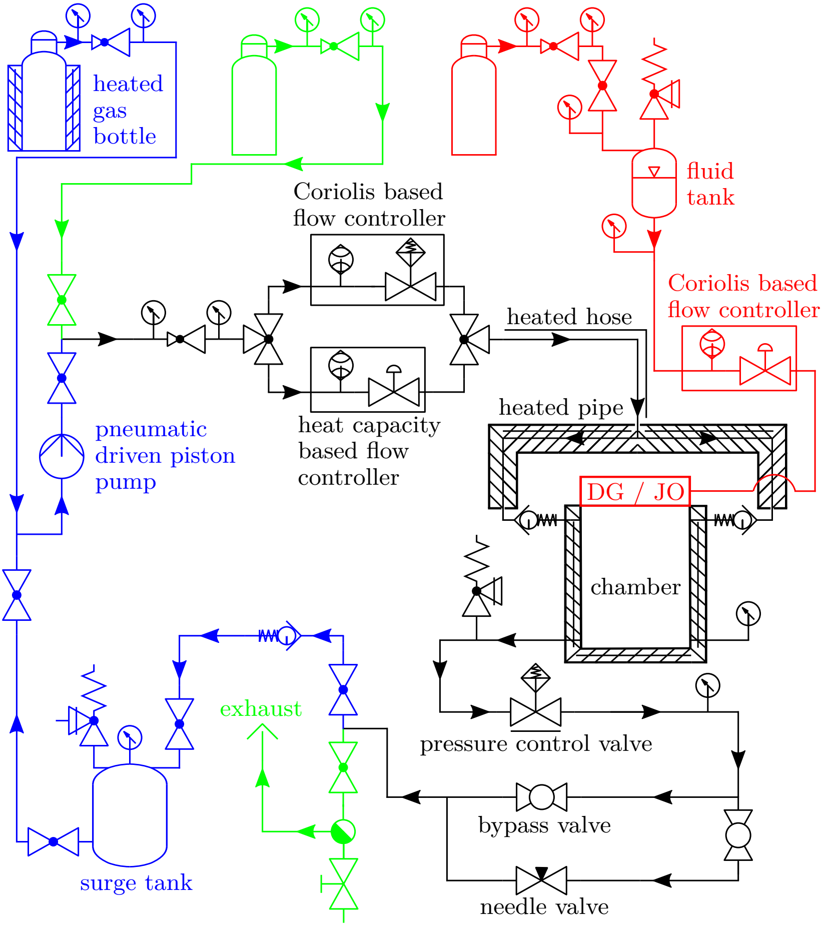

Figure 3.6: Schematics of the gas and liquid supply and pressure control system. The fluid supply for the jet orifice and droplet generator is highlighted in red. For the open operating mode the green extensions are used. The closed mode of operation is indicated in blue. DG: droplet generator; JO: jet orifice module; All symbols are chosen according to ISO 1219-1:2012-06 [45].

Before entering the pressure chamber the pressurised gases are preheated by a customised heated hose to temperatures up to 323 K. High temperatures of up to 773 K are obtained by using mineral wool insulated heated pipes with build–in heating cartridges (HLP T, Türk+Hillinger GmbH). The heating cartridges and the heated hose are controlled by PID controllers (LTR 4200/3500, Juchheim GmbH) and type–K thermocouples (TC Mess- und Regeltechnik GmbH). Based on the thermal insulation, the temperature controlled chamber and the heated inflow, a stationary temperature control within ±0.5 K is achieved. However, for mean chamber temperatures between 500 and 700 K the temperature difference between top and bottom rises from around $\Delta T = 2\,\mathrm{K}$ up to 9 K, respectively. Note that the temperature distribution inside the chamber is considered in the estimation of the measurement uncertainty of the temperature inside the chamber, as described by Schaumäker [88]. Figure 3.7b exemplarily depicts the temperature distribution over time for a nitrogen atmosphere with a chamber pressure of $p_{\mathrm{ch}} = 8\,\mathrm{MPa}$ and a chamber temperature of $T_{\mathrm{ch}} = 603.7\,\mathrm{K}$. Additionally, the chamber temperature T_{ch} (dashed line) and the corresponding error limits (dotted line) inside the pressure chamber are shown.

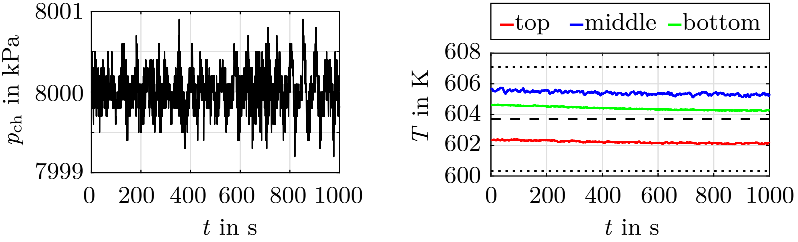

(a) Chamber pressure over time. (b) Chamber temperature over time.

Figure 3.7: Chamber characteristics for a nitrogen atmosphere with a pressure of $p_{\mathrm{ch}} = 8\,\mathrm{MPa}$ and a temperature of $T_{\mathrm{ch}} = 603.7\,\mathrm{K}$. Dashed line: mean temperature; Dotted lines: error limit.

The pressure is controlled by a temperature controlled pneumatic control valve (RC25, Badger Meter Europa GmbH) at the system exhaust. The latter is controlled by a PID controller programmed using LabVIEW 2016 (National Instruments Corp.). To optimise pressure control a needle valve is places downstream of the control valve prior to the exhaust/surge tank. Due to the combination of control and needle valve a stationary pressure control within ±1 kPa is achieved for all operating conditions. The chamber pressure over time for a nitrogen atmosphere at 603.7 K and 8 MPa is shown in Fig. 3.7a.

Since the derivation of the equations presented in the upcoming chapter 4.2.1 rely on the assumption of negligible flow velocities, it is important to emphasise that the mass flows do not exceed $6.9\,10^{-4}\,\mathrm{kg\,s^{-1}}$ for carbon dioxide and $3.5\,10^{-4}\,\mathrm{kg\,s^{-1}}$ for argon, nitrogen and the predefined mixtures. This leads to mean flow velocities inside the chamber of $0.04\,\mathrm{m\,s^{-1}}$. Furthermore it should be stressed that to exclude contamination from previous investigations, the chamber is carefully evacuated before each set of experiments.

3.2 Optical arrangement for laser–induced thermal acoustics

Laser–induced thermal acoustics relies on non–linear interactions of matter with an optical interference pattern to detect speed of sound, acoustic damping rate as well as thermal diffusivity. The optical interference pattern is created by two short pulsed excitation laser beams emitted by a Nd:YAG laser with an excitation wavelength of $\lambda_{\mathrm{exc}} = 1064\,\mathrm{nm}$. The third input wave is provided by a continuous wave DPSS laser with a wavelength of $\lambda_{\mathrm{exc}} = 532\,\mathrm{nm}$ and a 5 MHz line–width. It interrogates the resulting changes in the physical properties of the investigated fluids generated by the spatially periodic modulated polarisation/light intensity distribution due to the crossed excitation beams. Note that the line–width of the interrogation laser source is smaller than the minimal expected Doppler shift experienced by the signal beam. The arrangement of beam splitters and mirrors allows uniform splitting of the excitation beam and adjustment of the optical path length of both excitation beams. To achieve high grating excitation efficiency, both beams should be equal in intensity, with respective path length smaller than the excitations laser coherence length, as discussed in Stampanoni-Panariello et al. [100]. Additionally, the direction of linear polarisation of the excitation beams is set perpendicular to the crossing plane (Rozouvan and Dreier [86]).

The optical arrangement of the high–speed LITA system is depicted in Fig. 3.8. Excitation laser pulse detection is realised by a high–speed silicon detector (D2; DET10A/M, Thorlabs Inc.) and logged via the data acquisition unit (DAQ). To adjust the region of the highest laser intensity a beam expander (BE; 87–562, Edmund Optics Inc.) is added to the excitation beam path. The latter is vital in ducted flows to place the region of highest laser intensity at some distance to the windows, as discussed by Hell [41]. Additionally the beam expander can be used to adjust the size of the optical interference pattern. The direction of linear polarisation is ensured by a Glan–Laser polariser (GLP). Before entering the pressure chamber the excitation beam is 50/50–splitted using a beam splitter (T). Finally, a forward folded BOXCARS configuration is applied to arrange excitation and interrogation beams and achieve phase matching.

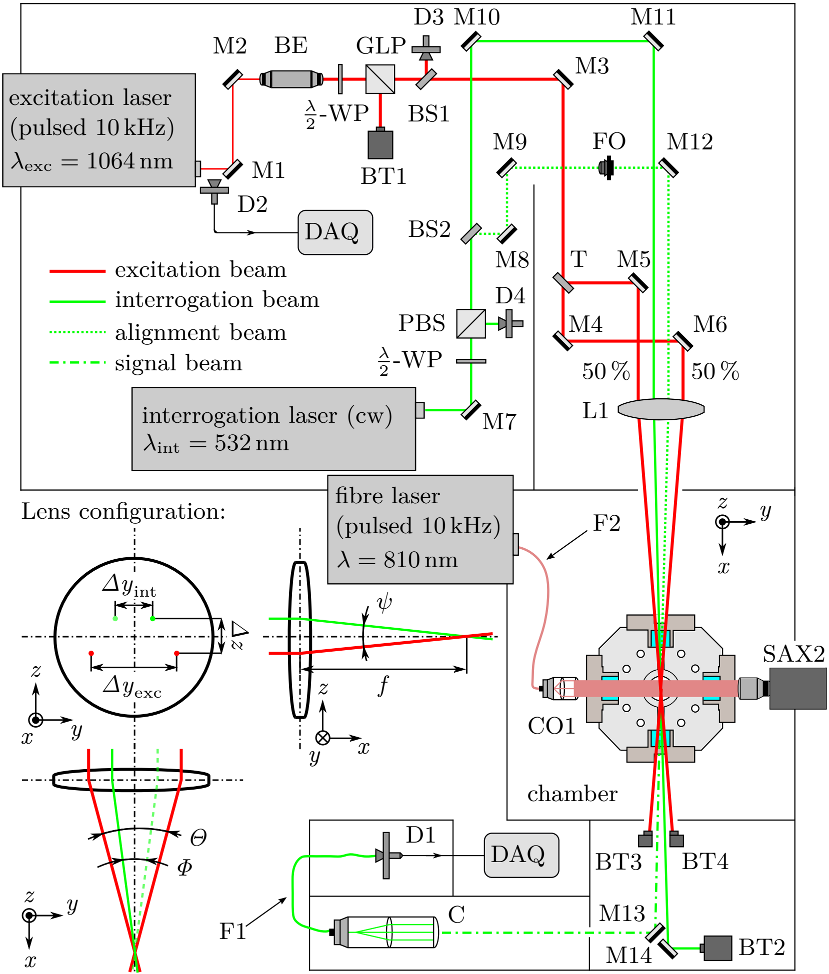

Figure 3.8: Optical setup of the high–speed laser–induced thermal acoustics system with shadowgraphy arrangement for flow field visualisation. BE: beam expander; BS: beam sampler; BT: beam trap; C: coupler; CO: collimator; D: detector (D1: avalanche detector; D2: silicon detector; D3, D4: thermal sensor); DAQ: data acquisition unit; F: fibre; FO: neutral density filter wheel with orifice; GLP: Glan–Laser polariser; L: lens; M: mirror; PBS: polarised beam splitter; SAX2: high–speed camera; T: beam splitter; WP: wave–plate.

All beams are crossed and focused into the measurement volume via an anti–reflective–coated lens (L1; $f = 1000\,\mathrm{mm}$ at 532 nm). The focal length is selected based on the expected speed of sound, the available bandwidth of the detector, the data acquisition unit, as well as the position of pressure chamber and optical setup. The latter has hereby been the most important selection criterion for the LITA setups used in this work. The two excitation beams are positioned with $\Delta y_{\mathrm{exc}} \approx 36.9\,\mathrm{mm}$ distance to each other on the lens, yielding to a crossing angle of $\Theta \approx 2^{\circ}$ and a grid spacing of $\lambda \approx 30\,\mu\mathrm{m}$.

The power of the interrogation beam is adjusted between 0.1 to 8.5 W to ensure good signal to noise ratio. To achieve a stable output at low power settings, the beam power is reduced using a polarising beam splitter (PBS) together with a $\lambda/2$–wave–plate (WP), and a thermal beam power sensor (D4; S405C, Thorlabs Inc.). The interrogation beam is scattered on the spatially periodic perturbations within the measurement volume. Subsequently, the scattered signal beam is spectrally and spatially filtered by a coupler (C) with an integrated laser–line filter and single–mode (SM) or multi–mode (MM) fibres (F1). For detecting the signal beam, an avalanche detector (D1; APD110, Thorlabs Inc.) is used, where the voltage signal is logged with 20 GS/s by the data acquisition unit (DAQ).

Since different optical layouts, laser sources, and DAQs are used within this work, the following sections highlight these differences and present the operational parameters and specification of the used LITA setups. Additionally, the alignment process using a beam profiler camera and tomographic measurements of the high–speed LITA measurement volume are shown.

3.2.1 Enhancement of the low frequency LITA setup

The optical low frequency LITA arrangement is adapted from the one developed by Hell [41] and Förster [30]. Note that the term ’low frequency’ refers to the pulse frequency of the laser used in the setup. It is introduced to distinguish this setup from the high–speed arrangement. In the present work, the low frequency LITA setup is used for investigating pure atmospheres and predefined binary mixtures. For excitation, a pulsed Nd:YAG laser (QuantaRay, Spectra Physics Inc.: $\lambda_{\mathrm{exc}} = 1064\,\mathrm{nm}$, $\tau = 10\,\mathrm{ns}$, 30 GHz line–width) with an operating frequency of 10 Hz is used. The interrogation beam is emitted by a cw DPSS laser (Verdi V8, Coherent Inc.). Data acquisition is done with 20 GS/s by a 1 GHz bandwidth digital oscilloscope (Waverunner 610Zi, Teledyne LeCroy). The signal length is hereby set between 1 and 2 µs, depending on the detected signal.

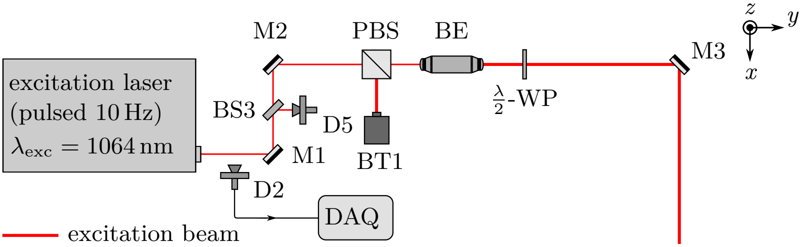

Figure 3.9: Excitation beam energy monitoring and polarisation arrangement of the low frequency laser–induced thermal acoustics setup. BE: beam expander; BS: beam sampler; BT: beam trap; D: detector (D2: silicon detector; D5: pyroelectric sensor); DAQ: data acquisition unit; M: mirror; PBS: polarised beam splitter; WP: wave–plate.

First studies have been conducted with the excitation beam energy monitoring and polarisation arrangement shown in Fig. 3.9. The excitation laser pulse energy is continuously monitored by a pyroelectric sensor (D5; ES111C, Thorlabs Inc.), whereas polarisation is set in a first step by a PBS and a $\lambda/2$–WP. Pulse energies used for investigation are between 41 and 76 mJ. Later investigations with the low frequency setup have used the optimised arrangement illustrated in Fig. 3.10. Note that Fig. 3.9 and Fig. 3.10 only present a section of the whole low frequency LITA setup. Following mirror 3 the optical arrangement depicted in Fig. 3.8 is used.

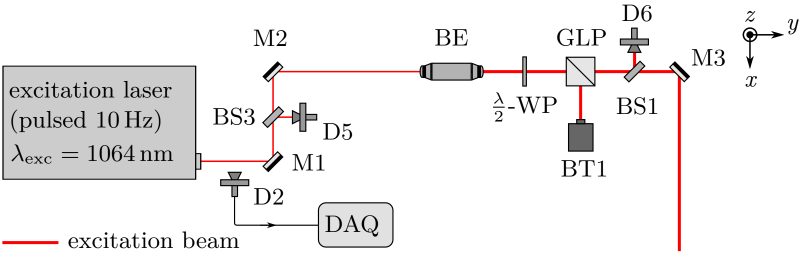

Figure 3.10: Excitation beam energy monitoring and polarisation arrangement of the low frequency laser–induced thermal acoustics setup after optimisation. BE: beam expander; BS: beam sampler; BT: beam trap; D: detector (D2: silicon detector; D5, D6: pyroelectric sensor); DAQ: data acquisition unit; GLP: Glan–Laser polariser; M: mirror; WP: wave–plate.

To improve beam quality and ensure stable and reproducible conditions for low excitation energies, the beam energy monitoring and polarisation arrangement has been optimised as depicted in Fig. 3.10. With the optimised setup the excitation laser is set to a constant pulse energy of 150 mJ, which is continuously measured by a pyroelectric sensor (D5; ES111C, Thorlabs Inc.). The energy is subsequently controlled by a $\lambda/2$-WP together with a GLP and observed by another pyroelectric sensor (D6; ES111C, Thorlabs Inc.). The excitation pulse energy used for investigating is adjusted to values between 18 and 50 mJ. Using equation (3.1), referred in [74], the Gaussian half–width of the excitation ω_{th} and interrogation beams σ_{th} in the focal point is calculated based on the unfocused beam data sheet specifications ω_0 and σ_0. The focal length of the lens is f, while the beams wavelength is λ. This results in a Gaussian half–width of the excitation beam of 92 µm.

$$\begin{aligned} \omega_{\text{th}} &= \frac{\lambda_{\text{exc}}\, f}{\pi\, \omega_0} \\ \sigma_{\text{th}} &= \frac{\lambda_{\text{int}}\, f}{\pi\, \sigma_0} \end{aligned} \tag{3.1}$$

However, with the necessity to place the location of highest laser intensity behind the window downwards of the interference pattern, measurements taken by a near infra–red enhanced beam profiler camera (WinCamD, DataRay Inc.) yield 159 µm. Based on the Gaussian beam profiler measurements and the present beam arrangement the optical measurement volume is an ellipsoid elongated in x-direction. By the application of equation (2.3) the maximum size of the inference pattern is estimated to be 318 µm in the central diameter and 17.6 mm in length. However, it is important to emphasise that the optical interference pattern inhibits a Gaussian intensity profile with a grid spacing Λ modulated in y–direction, as discussed by Siegman [97]. Together with the propagation of the acoustic waves normal to the beam direction and the fact that only a portion of the grating is illuminated by the interrogation beam, the spatial resolution in x–direction is higher than the optical interference pattern might suggests. This enables the investigation of speed of sound radial profiles in multicomponent jets and allows comparison to flow visualisation investigations performed by Baab et al. [6]. As discussed by Steinhausen et al. [107], this results in a spatial resolution of approximately 318 µm in diameter and less than 2 mm in length. The theoretical Gaussian half–width in the focal point of the interrogation beam σ_{th} is computed using equation (3.1) to be approximately 151 µm. Beam profiler measurements corroborate these values.

3.2.2 Development of the high–speed laser–induced thermal acoustics setup

The high–speed laser–induced thermal acoustics arrangement, shown in Fig. 3.8, is applied in the time–resolved investigation on droplet evaporation and the stationary studies of gaseous jet mixing processes. The setup employs a high frequency pulsed Nd:YAG laser (INNOSLAB, EdgeWave GmbH: $\lambda_{\mathrm{exc}} = 1064\,\mathrm{nm}$, $\tau = 8.8\,\mathrm{ns}$, 53 GHz line–width) with an operating frequency of 10 kHz. The laser is operated at a constant pulse energy of 14 mJ, which is subsequently controlled by a $\lambda/2$-WP together with a GLP and continuously monitored by a thermal sensor (D3; S322C, Thorlabs Inc.). The third input wave is generated by a continuous wave DPSS laser (Verdi V6, Coherent Inc.). For data acquisition with 20 GS/s a 2.5 GHz bandwidth digital oscilloscope (WavePRO 254HD, Teledyne LeCroy) is used. In case of the gaseous jet mixing studies, signal length is set to 1 µs, whereas droplet evaporation studies are conducted with a number of data acquisition points set to 2 GS. The signal length is, hence, 100 ms. With an operating frequency of 10 kHz this enables the time–resolved capture of 1000 LITA signals.

The theoretical Gaussian half–width of the excitation beams in the focal point in y and z–direction is $\omega_{y,\mathrm{th}} = 123\,\mu\mathrm{m}$ and $\omega_{z,\mathrm{th}} = 40\,\mu\mathrm{m}$, respectively. The elliptical cross section of the interference pattern is a result of the elliptical beam profile ($\omega_{\mathrm{min}}/\omega_{\mathrm{max}} = 0.33$) of the used high–speed excitation laser source. By the application of equation (2.3) the maximum size of the ellipsoid inference pattern is approximately 13.6 mm in length, with an elliptical cross section in the centre of 80 µm in height and 246 µm in width. As previously mentioned, the spatial resolution in x–direction of the LITA technique is, however, higher than the lengths of optical interference pattern might suggests. Therefore, a detailed assessment of the LITA measurement volume is presented in the next subsection. The analysis is related to the LITA setup used for the investigation of injection processes. As for the low frequency setup the theoretical Gaussian half–width of the interrogation beam σ_{th} is 151 µm.

3.2.3 Visualisation and assessment of the laser–induced thermal acoustics measurement volume

For the injection experiments, the length of the measurement volume for the high–speed LITA arrangement is assessed in the following. Tomographic measurements of the beams' crossing are taken with the beam profiler camera mounted centric on top of the measurement chamber. To include refractive effects of the windows, a quartz window with the same specification is placed in front of the sensor. Laser intensity is reduced by a neutral density filter to avoid over–saturation and damage to the sensor.

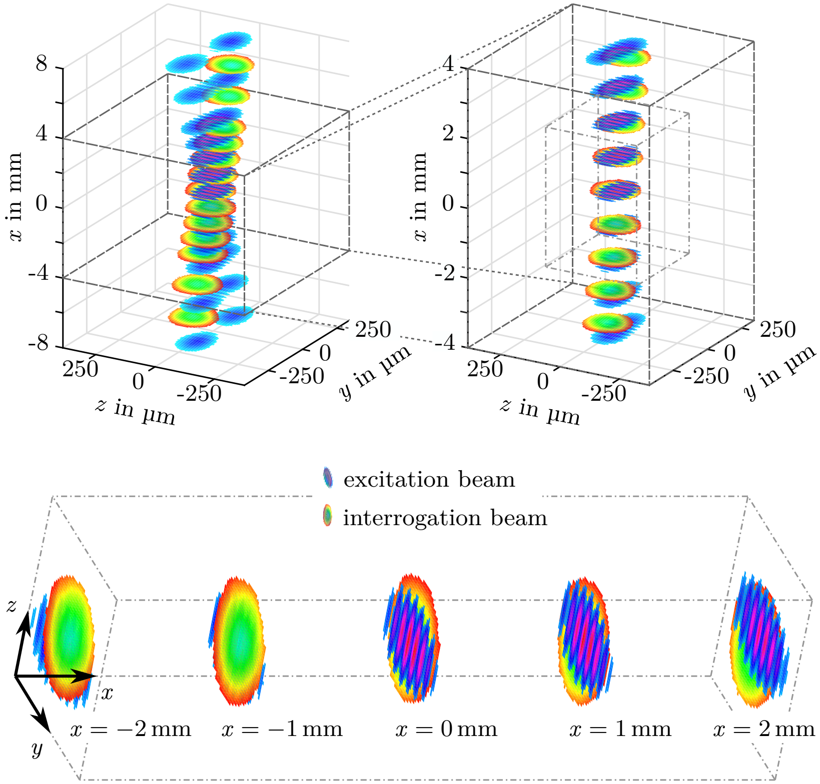

Figure 3.11: Tomographic beam profiler measurements of high–speed laser–induced thermal acoustics measurement volume for investigating droplet evaporation and gaseous jet mixing processes. Beam expander is adjusted for a small optical interference pattern. **Upper left:** Full length of the optical interference pattern. **Upper right:** Enlarged view to highlight the fully developed interference pattern. **Lower:** Zoom of specific positions with full overlap of interference pattern and interrogation beam.

Figure 3.11 displays three enlarged views of the tomographic measurements. On the upper left, the complete length of the interference pattern is shown. By inspecting the excitation beams it becomes evident that the interference pattern is not fully developed at beginning and end of the length of the grating. This observation is confirmed by the analytical work on Bragg diffraction on a intensity grating conducted by Siegman [97].

Zooming in to a length with fully developed interference pattern (upper right) the images show an incomplete overlap in z–direction of the optical grid with the interrogation beam at a half length greater/smaller than $\pm 2\,\mathrm{mm}$. Under the assumption of negligible flow velocities, the theoretical signal model derived by Schlamp et al. [89] concludes that a misalignment in z–direction only leads to a reduced signal strength. Hence, the influence of x–positions with $|x| > 2\,\mathrm{mm}$ is insignificant to the LITA signal. In virtue of this fact, only the positions with a full overlap of interference pattern and interrogation beam, have a significant influence on the detected signal, as is shown in the blow up in the lower image of Fig. 3.11. Concordantly, the shape of the LITA measurement volume is an ellipsoid approximately 4 mm in length, 246 µm in width and 80 µm in height, which defines the spatial resolution of the LITA arrangement. It is important to emphasise that the term ’LITA measurement volume’ referees to the previously tomographically determined ellipsoid, which is different in length from the optical interference pattern. This difference is based on the illumination of the grating by the interrogation beam.

3.2.4 Design of a high–precision optical alignment process

Besides a thorough calibration of the optical parameters of the LITA setup a precise and reproducible alignment is essential for good LITA signals and a robust curve fitting methodology. Alignment of the excitation beams, interrogation, and alignment beam is achieved using the beam profiler camera. Note that since the refractive indices depend on the wavelength, the focal points of the excitation beams differ slightly from the focal point of the interrogation and alignment beam.

Measurements are taken at three different positions, the focal point of interrogation and alignment beam (Position I), the focal point of the excitation beams (Position II), and one position behind the excitation focal point (Position III), as shown in Fig. 3.12. The images present exemplarily the position of the aligned beams in case of the high–speed LITA setup with a beam expander adjustment to generate a large optical interference pattern.

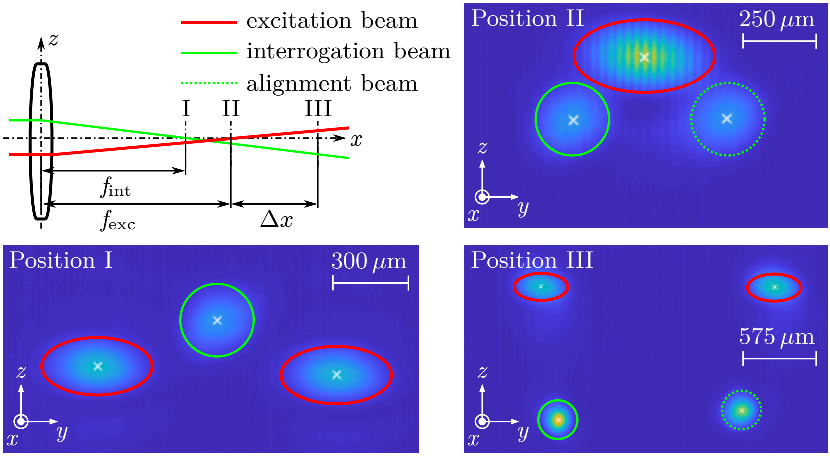

Figure 3.12: Schematic drawing of the laser–induced thermal acoustics alignment process. Beam expander is adjusted for a large optical interference pattern.

The location of the alignment and excitation beams are computed for each position based on the location of the interrogation beam. The latter is used as a reference and remains untouched after initial beam alignment. A detailed description of the alignment process and the mathematical derivation is presented by Stein [102]. Only mirror 3 and mirror 9 (M3 & M9 in Fig. 3.8) are used for alignment. Note that slight adjustments of M3 cause only a change in the location of the interference pattern in y and z–direction, while the relative distance between the beams remains unchanged. Concordantly, the beam crossing geometry is unaltered and the geometric calibration is applicable. Note that the position behind the excitation focal point (Position III) is necessary to set angle and location of the alignment beam correctly.

Analysing the position images and comparing the alignment to the theoretical beam locations, shown in Fig. 2.3, two observations are made. First, due to the difference in focal length of the excitation and interrogation beam, a slight misalignment in z–direction is present. Second, no intersection between the interrogation and the optical interference pattern occurs, hence, a slight misalignment in y–direction is necessary to generate a strong LITA signal. Therefore, misalignments have to be considered in the theoretical model used for curve fitting.

3.3 Optical setups for flow visualisation

The transient investigation on droplet evaporation and the stationary studies of gaseous jet mixing processes are conducted using simultaneously flow visualisation together with the LITA measurements. The applied shadowgraphy and schlieren arrangements are presented in the next sections.

3.3.1 Shadowgraphy setup for visualising droplet evaporation

For the observation of droplet evaporation in the vicinity of the critical point the shadowgraphy setup, shown in Fig. 3.13, is used. Shadowgraphy is an optical technique for visualising changes in density gradients. These changes are displayed by direct shadowgraphy in parallel light due to the second derivative of the refractive index ($\partial^2 n/\partial x^2$, $\partial^2 n/\partial z^2$) in the imaging plane, as described by Settles [90].

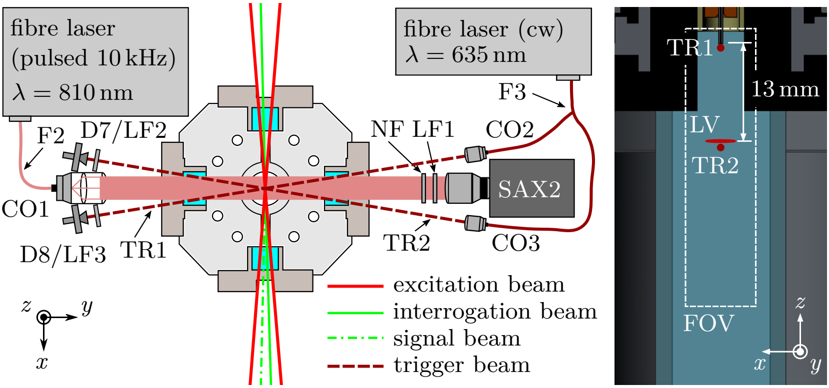

Figure 3.13: Shadowgraphy setup for flow visualisation of droplet evaporation and integrated trigger configuration. CO: collimator; D: detector (D5, D6: silicon detector); F: fibre; FOV: field of view; LF1: laser–line filter (810 nm); LF2, LF3: laser–line filter (635 nm); LV: LITA measurement volume; NF: Nd:YAG notch filter; SAX2: high–speed camera (Photron FASTCAM SA-X2); TR: trigger beam.

The collimated light is generated by a fibre coupled laser source (Cavilux HF, Cavitar Ltd.) with a wavelength of $\lambda = 810$ nm, an operating frequency of 10 kHz and a laser pulse length of $\tau = 30$ ns. After spectral filtering by a laser–line filter (LF1; 810 nm) and a Nd:YAG notch filter (NF) the shadowgram is captured by a high–speed camera (SAX2; FASTCAM SA-X2, Photron) equipped with a long–distance microscope (K2 DistaMax, Infinity Photo–Optical GmbH). Note that the notch filter is used to protect the camera sensor against the high intensity LITA beams. Optical calibration using a distortion target (58–509, Edmund Optics Inc.) and a USAF 1951 high–resolution target (55–622, Edmund Optics Inc.) yields 36 µm/px with a field of view (FOV) of approximately 37 x 9.5 mm.

Time synchronisation of the laser pulses of both LITA and shadowgraphy setup is achieved by a light barrier (TR2) just below the position of the LITA measurement volume (LV), depicted in Fig. 3.13. As for the trigger of the electrical detachment (TR1), described in subsection 3.1.2, the light beam is generated by a fibre coupled cw laser with a wavelength of 635 nm (S1FC635, Thorlabs Inc.). It is focused directly below the capillary, spectrally filtered and detected by a high–speed silicon detector (D7; DET100A/M, Thorlabs Inc.). When the droplet passes the barrier, the laser sources of the LITA arrangement and the shadowgraphy setup are triggered. Delay times are set to ensure laser pulse synchronisation of both the LITA and shadowgraphy setup within the exposure time of the high–speed camera.

3.3.2 Schlieren setup for visualising gaseous jet mixing

The presented investigations on stationary gaseous jets mixing experience changes in density gradients, which are too small to visualise with a shadowgraphy setup. Hence, a optical arrangement utilising the schlieren technique is used. Schlieren is an optical line–of–sight technique for visualising changes in density. To that end, parallel light is focused after passing the observing flow field onto a knife edge and observed by a image capturing system. When using a vertical knife edge the illuminance level in the schlieren image corresponds to the spatial derivative of the refractive index in horizontal direction ($\partial n / \partial x$), as discussed in Settles [90]. The schlieren setup is depicted in Fig. 3.14.

The collimated light is generated by a telecentric lens with a continuous, white LED as a light source. After focussing the parallel light onto a vertical knife edge (K) the schlieren image is spectrally filtered by a Nd:YAG notch filter (NF) and captured by a scientific CMOS camera (PCO; Edge 5.5, Excelitas PCO GmbH) equipped with the long–distance microscope (K2 DistaMax, Infinity Photo–Optical GmbH). The exposer time is hereby set to 100 ms. Optical calibration is realised by the distortion target (58–509, Edmund Optics Inc.) and the USAF 1951 high–resolution target (55–622, Edmund Optics Inc.). It results in a resolution of 2.5 µm/px, however, the diffraction limit of the optical

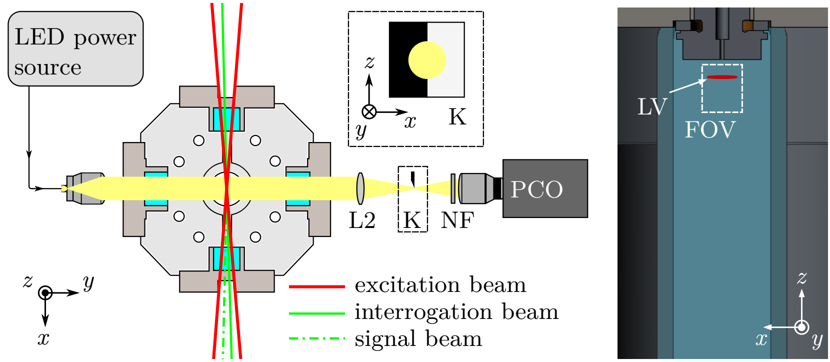

Figure 3.14: Schlieren setup for visualising gaseous jet mixing. FOV: field of view; K: vertical knife edge; L: lens; LV: LITA measurement volume; NF: Nd:YAG notch filter; PCO: sCMOS camera (PCO Edge 5.5).

system is 32 lines/mm or 15.7 µm/px. This leads to a field of view (FOV) of approximately 6.4 x 5.4 mm. Synchronisation between LITA and schlieren setup is achieved by a pulse generator. For every image approximately 27 LITA signals are captured. In this context it is important to note that a stationary process is observed and only mean values are compared in the gaseous jets mixing studies.

CHAPTER 4

Data processing and uncertainty evaluation

Post–processing of detected laser–induced thermal acoustics signals is generally performed in two different schemes. As previously presented in Fig. 2.4 flow properties, such as speed of sound are related to different frequencies of the captured LITA signal. Hence, a first approach relies on frequency analysis to extract the speed of sound data from the signal. A second approach analyses the time domain and compares the detected signal with a theoretical model. Theoretical models that describe the signals temporal domain are presented by different groups (Stampanoni-Panariello et al. [100], Li et al. [57], Cummings et al. [21]). However, only the comprehensive model by the group of Cummings and co-workers [21, 89] account for finite beam sizes. Since the LITA arrangement in this work uses focused beams, only the theoretical model developed by Cummings et al. [21], which has been extended by Schlamp et al. [89] to account for possible beam misalignment is applicable. The following chapter presents the signal post–processing both in the frequency and time domain. Additionally, the methodology for evaluation of measurement uncertainties is shown.

4.1 Evaluation of measurement uncertainties

The uncertainty analysis for the operating conditions, calibration, and results presented in this work is performed following the guide to the expression of uncertainty in measurement by the Joint Committee for Guides in Metrology [47]. Error propagation of uncertainties for differentiable values is conducted using Gaussian error propagation as suggested by the Joint Committee for Guides in Metrology [47]. In case of non–differentiable dependencies, such as values taken from the NIST database by Lemmon et al. [56] and the presented curve fitting algorithms, uncertainties of input parameters are propagated by applying sequential perturbation as presented by Moffat [64]. Note that by using the sequential perturbation method a Gaussian distribution is inherently assumed. The statistical error of the curve fitting algorithm itself is based on the confidence interval computed by the algorithm. These intervals are estimated using the inverse $\boldsymbol{R}$ factor from the $\boldsymbol{QR}$ decomposition of the Jacobian, the root mean squared error as well as the degrees of freedom [61]. $\boldsymbol{Q}$ is hereby an orthogonal matrix, while $\boldsymbol{R}$ is a upper triangular matrix. Based on these intervals and the sequential perturbation computations for each output parameter the measurement uncertainties of the curve fitting results are computed by the square–root of the summation of the square of each contribution. A brief summary of the methodology is presented in appendix A of this work.

4.2 Frequency domain based signal processing

Frequency analysis via fast Fourier transformation algorithms is a common approach in engineering application and signal processing. It allows for an effective and fast computation of the power spectral density S_{xx} of a discretised signal, such as the recorded LITA signal. The obtained power spectrum in the frequency domain is then used for both signal filtering and derivation of flow properties. The upcoming section presents the applied frequency analysis, signal filtering, and speed of sound estimation.

4.2.1 Speed of sound estimation based on signal frequency

The simplest and most common approach to determine speed of sound data from a detected LITA signal is based on the frequency domain of the temporal LITA signal. The speed of sound data are hereby directly related to the beat frequency Ω of the signal. Since only the spacing of the optical grid Λ as a parameter of the optical arrangement is involved, no equation of state or modelling assumptions are necessary at this point.

Based on the theoretical considerations by Hemmerling and Kozlov [42] the speed of sound c_s of the probed fluid can be calculated by

$$c_s = \frac{\Omega_{j\,c_s} \Lambda}{j} \ . \tag{4.1}$$

The constant j is hereby an indicator for resonant or non–resonant fluid behaviour at the wavelength of the excitation beam. In case of resonant fluid behaviour $j = 1$, while in case of non–resonant fluid behaviour $j = 2$.

Note that without a mixing model, thermometry can only be performed at a known gas composition and pressure, by applying a suitable model for the speed of sound. However, the probed temperature is then only indirectly determined and depending on the chosen model for the fluid or mixture under consideration. The latter can be challenging in supercritical or high–pressure states.

4.2.2 Frequency analysis of laser–induced thermal acoustics signals

The frequency analysis of the discrete LITA signals is performed using the direct Fourier transformation (DFT) algorithm implemented in Matlab R2018a (The MathWorks Inc.) [61]. The resolution in the frequency domain is due to the discretisation in frequency directly related to the measurement uncertainty of c_s by equation (4.1). To ensure a suitable resolution and in order to reduce the computational effort the data are zero–padded in the time domain. The best compromise between memory usage, computational time and accuracy is a 18 bit resolution in the frequency domain. As discussed by Harris [39], a DFT assumes the input signal to be periodic over the number of sample points. While being periodic in its oscillation, the damping of the LITA signal prevents a truly periodic treatment. Additionally, offset in signal intensity at the beginning and the end of the observation interval lead to a discontinuity in the periodic extension, as presented by Harris [39]. These discontinuities result, due to the finite signal duration, in a spectral expansion also known as spectral leaking. Note that spectral leakage is not caused by the sampling, albeit the amount of leakage depends on the sampling period [39]. Due to the spectral leaking, an initial single frequency component is smeared out over neighbouring peaks in the power spectral density. Eventhough, an evaluation of the frequency domain according to equation (4.1) is possible, false prediction might occur and filtering in the frequency domain becomes impossible. As suggested by Harris [39], the application of a window function counteracts spectral leaking by weighing the data, leading to a reduction of discontinuities at the observation boundary. A discussion on the use of window functions as well as a catalogue of different window function for harmonic signal analysis is presented by Harris [39].

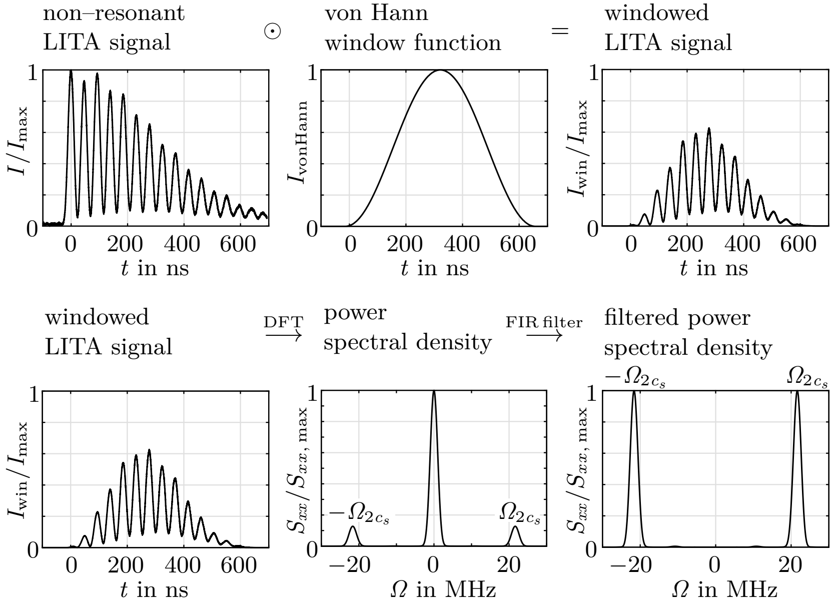

Figure 4.1: Methodology for frequency analysis of non–resonant laser–induced thermal acoustics signals.

A schematic representation of the methodology used for frequency analysis in the presented work is depicted in Fig. 4.1 and Fig. 4.2 for non–resonant and resonant signal evaluation, respectively. The time domain is presented as normalised signal intensity $I/I_{\max}$ over time t, while the frequency domain is displayed as normalised power spectral density $S_{xx}/S_{xx,\,\max}$ over signal beat frequency Ω. As window function a von Hann window, also referred to as Hanning window, is used. A detailed parametric study and theoretical consideration on the selection of a suitable window function for the recorded LITA signals can be found in the work of Stein [102]. As shown in Fig. 4.1, the non–zero mean of the time–based LITA signal leads to a zero frequency in the power spectral density, which is not relevant for the signal evaluation. By applying a finite impulse response (FIR) filter in the frequency domain the zero-frequency is filtered out, leading to frequency components only related to properties of the probed flow. A detailed overview of FIR filter analysis and application is presented by Oppenheim et al. [70].

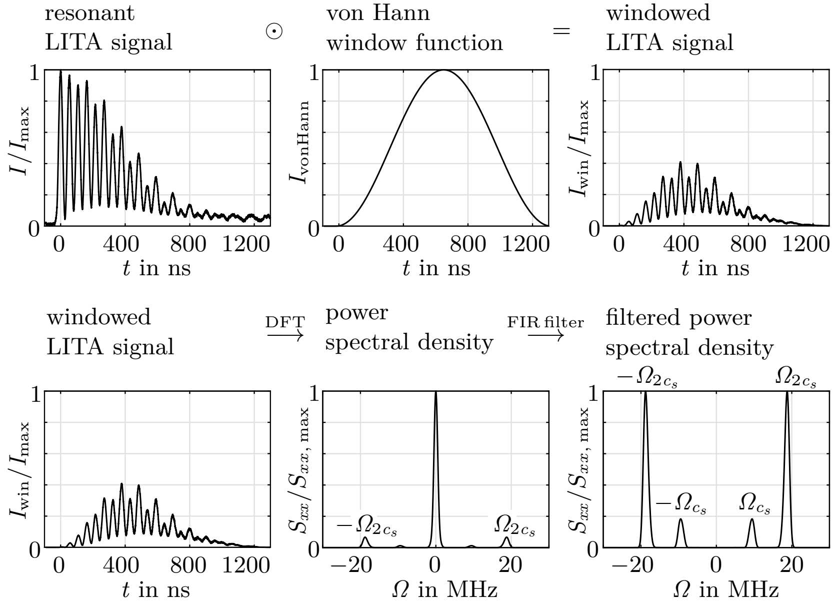

Figure 4.2: Methodology for frequency analysis of resonant laser–induced thermal acoustics signals.

As discussed in section 2.1.3, a non–resonant fluid response with homodyne detection stems from stimulated Brillouin scattering, which results in single non–zero beat frequency $\Omega_{2c_s} = 2\Omega_{c_s}$ two times the size of the Brillouin frequency Ω_{c_s}. In case of resonant fluid behaviour, the additional thermal grating leads to two non–zero beat frequencies, namely the Brillouin frequency Ω_{c_s} and the frequency Ω_{2c_s} due to the electrostrictive fluid response. These characteristic frequencies are applied for speed of sound evaluation.

4.2.3 Filter algorithm based on time and frequency domain

A high signal quality is essential for a robust signal evaluation. This is especially true for post–processing in the time domain using theoretical models. To ensure adequate signal quality, the LITA signals are filtered in both the time and frequency domain. First, all detected signals with a signal intensity below 10 % of the selected oscilloscopes detection range and all over–saturated signals are sorted out. Second, all remaining signals are filtered based on the valid shape of a non–resonant or resonant signal in the frequency domain.

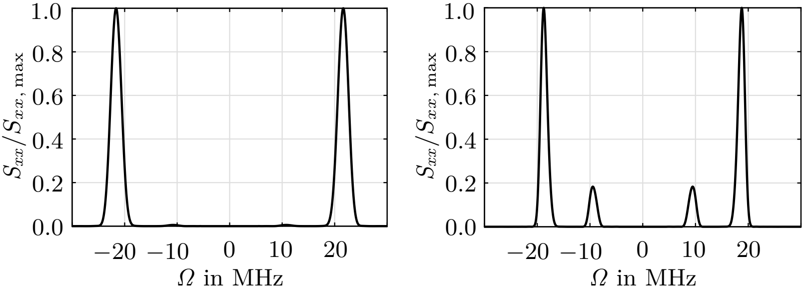

(a) Non–resonant fluid behaviour.

(b) Resonant fluid behaviour.

Figure 4.3: Valid signal shape in frequency domain for resonant and non–resonant fluid behaviour.

As depicted in Fig. 4.3, the previously presented frequency analysis in non–resonant signals leads to a single distinct non–zero frequency, whereas resonant signals show two distinct non–zero frequencies. All remaining valid signals are then used to estimate speed of sound based on the signals beat frequency and averaged to calculate a mean LITA signal for each case, which is subsequently used for the time–based signal evaluation.

4.3 Methodology for time domain based signal processing

By applying the analytical model for finite beam sizes proposed by Schlamp et al. [89], it is possible to extract the speed of sound, the acoustic damping rate as well as the thermal diffusivity from the temporal domain of the signal. However, due to the complexity of the model, curve fitting is challenging. This is mainly a result of the interdependencies between thermodynamic parameters (c_s, Γ,

D_T) on the Green's function coefficients $\mathcal{H}_{e,P_{1,2}}$ and $\mathcal{H}_{e,T}$ for the opto–acoustic fluid response to electrostriction as well as on the Green's function coefficients $\mathcal{H}_{\Theta,P_{1,2}}$, $\mathcal{H}_{\Theta,T}$, and $\mathcal{H}_{\Theta,D}$ related to thermalisation. These coefficients are necessary to compute the Green's functions $\mathcal{H}_e$ and $\mathcal{H}_\Theta$ that describe the opto–acoustic fluid response for electrostriction and thermalisation, respectively. However, in the scope of the investigated fluids and mixing processes, these interdependencies become negligible. A detail mathematical derivation of the full theoretical model is presented by Schlamp et al. [89] and Cummings et al. [21]. In the following only the necessary terms and assumptions for model understanding are presented.

Simplifications applied by Steinhausen et al. [107] are based on three key assumptions proposed by Cummings et al. [21] and Stampanoni-Panariello et al. [100], namely the limit of fast thermalisation, negligible damping over a wave period and an instantaneous release of absorbed laser radiation into internal energy. The latter can be assumed based on a comparison of the temporal signal shape with measurements with resonant fluid response presented in this work and resonant LITA signal with instantaneous heat release investigated by Hemmerling and Kozlov [43]. Additionally, as discussed by Stampanoni-Panariello et al. [100], the temporal shape of the excitation laser pulse is approximated by a δ-function at t_0. The justification and mathematical expressions of the applied assumptions are the following:

- **Limit of fast thermalisation:** Cummings et al. [21] showed that the hypothesis of fast thermalisation holds when the thermal diffusivity is much smaller than one $D_T \ll 1$.
- **Negligible damping over a wave period:** Cummings et al. [21] showed that damping is negligible over a wave period for acoustic damping rates much smaller than one $\Gamma \ll 1$.
- **Instantaneous release of absorbed laser radiation into internal energy:** Stampanoni-Panariello et al. [100] proposed that in case of an instantaneous release of absorbed laser radiation into heat $c_s\, q \ll \gamma_\Theta + \gamma_{n\Theta}$, where γ_Θ denotes the rate of excited-state energy decay caused by thermalisation and $\gamma_{n\Theta}$ denotes the rate of excited-state energy decay not caused by thermalisation.
- **Temporal shape of laser pulse:** Stampanoni-Panariello et al. [100] proposed a δ-function at t_0 for the excitation laser pulse, since the laser pulse length τ is small compared to the reciprocal of the acoustic frequency ($\tau \ll 1/\left(c_s q\right)$) as well as the reciprocal of the acoustic decay rates $\left(\tau \ll 1/\left(q^2 \Gamma\right)\right)$ and $\left(\tau \ll 1/\left(q^2 D_T\right)\right)$.

Under the above assumptions, the ratio of acoustic wave frequency to thermalisation rate becomes $\Pi = 0$ and the Green's function coefficients simplify to $\mathcal{H}_{e,P_{1,2}} = \pm i/2$, $\mathcal{H}_{e,T} = 0$, $\mathcal{H}_{\Theta,P_{1,2}} = 1/2$, $\mathcal{H}_{\Theta,T} = -1$, and $\mathcal{H}_{\Theta,D} = 0$. Correspondingly, the amplitudes of the acoustic waves $\mathcal{A}_{P1,P2}$ and the amplitudes of the thermal grating $\mathcal{A}_T$ in the upcoming modelling equations (4.4) and (4.5) of the LITA signal simplify to

$$\begin{aligned} \mathcal{A}_{P1,P2} &= 1/2\,\mathcal{U}_{\Theta} \pm i/2\,\mathcal{U}_{eP} \\ \mathcal{A}_T &= -1\,\mathcal{U}_{\Theta}\ . \end{aligned} \tag{4.2}$$

The real part of $\mathcal{A}_{P1,P2}$ denoted by $\mathcal{U}_{\Theta}$ is the modulation depth of thermalisation and indicates the influence of thermalisation on the damping oscillation of the LITA signal. The imaginary part $\mathcal{U}_{eP}$ approximates the modulation depth of electrostriction and expresses the electrostrictive contribution. Subsequently, $\mathcal{A}_T$ represent the weight of thermalisation on the signal damping. Both modulation depths are used as fitting constants. Note that in case of resonant fluid behaviour, both thermalisation and electrostriction must be considered. However, since non–resonant fluid behaviour can be modelled purely electrostrictive, the thermal modulation depth $\mathcal{U}_{\Theta}$ is considered negligible. This leads to a further simplified model. This simplification is discussed in the work of Stampanoni-Panariello et al. [100] for large beam sizes.

Additionally to the above discussed simplifications, the following assumption are made based on the specific conditions of the experimental investigations and the used optical arrangement:

- Considering the small beam crossing angles of the excitation beams Θ and the interrogation beam Φ in the optical setup it is assumed that $\cos(\Theta) \approx 1$ and $\cos(\Phi) \approx 1$.

- Due to low mass flow rates and therefore vanishing flow velocities, the influence of the bulk flow velocities v and w on the temporal signal shape is negligible. Hence, the bulk flow velocities can be neglected: $v \approx 0$ and $w \approx 0$.

- As discussed by Schlamp et al. [89], for negligible bulk flow velocities only the beam misalignment in y-direction $\bar{\eta}$ has an effect on the time history of the signal. Hence, after careful beam alignment through the quartz windows before each measurement generating a maximised signal, the beam misalignment terms η, ζ, and $\bar{\zeta}$ are neglected.

4.3.1 Theoretical model for large and small detector limits

In the derivations by Schlamp et al. [89] two possible solutions are presented that express the time–dependent dimensionless diffraction efficiency $\mathit{\Psi}(t)$ of a homodyne detected LITA signal. The so–called small detector limit (SDL) assumes an infinitesimal detector positioned perfectly aligned with the wave vector of the signal beam $\boldsymbol{k}_{\mathrm{sig}}$. It is applicable for measurements conducted using a strong spatial filtering prior to the detector. In the large detector limit (LDL) an infinite integration over the detection angle is performed, hence it is applicable for large detector configurations without or with minor spatial filtering. Both detector limits depend on the magnitude of the grating vector q, which in turn is a function of the grid spacing $\mathit{\Lambda}$. The latter can be defined by the crossing angle of the excitation beams $\mathit{\Theta}$ and the excitation wavelength λ_{exc}, see equations (2.7) and (2.2). In the following the governing equations of both detector limits are presented based on the assumptions and simplifications discussed in the previous section.

Large detector limit for all fibre type data evaluation

The large detector limit model depends on both the damping parameter $\mathit{\Sigma}_T$ related to the thermal grating and the parameters related to the damping of the acoustic waves $\mathit{\Sigma}_{P_{1,2}}$. These complex parameters are expressed by equation (4.3), as reported by Schlamp et al. [89].

$$\begin{aligned} \mathit{\Sigma}_{P_{1,2}} &= \exp\left\{-\mathit{\Gamma} q^2 \left(t - t_0\right) - \frac{2\left[\bar{\eta} \pm c_s \left(t - t_0\right)\right]^2}{\omega^2 + 2\sigma^2}\right\} \\ &\quad \exp\left\{\pm i q c_s \left(t - t_0\right)\right\} \\ \mathit{\Sigma}_T &= \exp\left\{-D_T q^2 \left(t - t_0\right) - \frac{2\bar{\eta}^2}{\omega^2 + 2\sigma^2}\right\} \end{aligned} \tag{4.3}$$

Time is indicated with t, while t_0 being the point in time of the laser pulse. The Gaussian half–width of the interrogation and excitation beam in the focal point are represented by σ and ω, respectively.

With equations (4.2) and (4.3), the time–dependent dimensionless diffraction efficiency $\mathit{\Psi}(t)$ can be expressed as

$$
\begin{aligned}
\mathit{\Psi}(t) \propto \exp & \left\{ -\frac{8\sigma^2}{\omega^2\left(\omega^2+2\sigma^2\right)} \left(\frac{c_s\left(t-t_0\right)}{2} \right)^2 \right\} \\
& \left\{ \left(\mathcal{P}_1+\mathcal{P}_2\right)\mathcal{T}^* + \left({\mathcal{P}_1}^*+{\mathcal{P}_2}^*\right)\mathcal{T} \right\} \\
& + \exp\left\{ -\frac{8\sigma^2}{\omega^2\left(\omega^2+2\sigma^2\right)} \left(c_s\left(t-t_0\right)\right)^2 \right\} \\
& \left(\mathcal{P}_1{\mathcal{P}_2}^* + {\mathcal{P}_1}^*\mathcal{P}_2\right) + \left(\mathcal{P}_1{\mathcal{P}_1}^* + \mathcal{P}_2{\mathcal{P}_2}^* + \mathcal{T}\mathcal{T}^*\right) \ ,
\end{aligned}
\tag{4.4}
$$

where the parameters $\mathcal{P}_1$, $\mathcal{T}$, etc. are estimated by $\mathcal{P}_1 = \mathcal{A}_{P1}\mathit{\Sigma}_{P_1}$, $\mathcal{T} = \mathcal{A}_T\mathit{\Sigma}_T$, etc. with * denoting the complex conjugate. A comparison of theoretical LITA signals in the investigated temperature and pressure range with non–resonant and resonant fluid behaviour using the full model by Schlamp et al. [89] and the presented, simplified model based on equation (4.4) is depicted in Fig. 4.4. The associated ambient conditions and model input parameter are listed in Tab. 4.1. Note that the full model by Schlamp et al. [89] depends on the specific heat ratio κ, which is therefore also listed.

Table 4.1: Overview of ambient conditions and input parameters for the model comparison shown in Fig. 4.4. Fixed input parameters: $\mathit{\Lambda} = 29.47\,\mu\text{m}$; $\sigma = 151\,\mu\text{m}$; $\omega = 226\,\mu\text{m}$. Volume viscosities needed for the computation of $\mathit{\Gamma}$ of CO_2 are computed using the model by Kustova et al. [51]. Necessary thermodynamic data are taken from Lemmon et al. [56].

ambient conditions			input parameters					
fluid	$p/$ MPa	$T/$ K	$\lvert\mathcal{U}_\Theta/\mathcal{U}_{eP}\rvert$	$c_s/$ $\text{m}\,\text{s}^{-1}$	$\bar{\eta}/$ µm	$\mathit{\Gamma}/$ $\text{mm}^2\,\text{s}^{-1}$	$D_T/$ $\text{mm}^2\,\text{s}^{-1}$	κ
Ar	6.0	609	0.00	471	−83	1.019	1.287	1.70
CO_2	1.0	299	0.05	263	−88	1.358	1.007	1.35

The deviation in signal intensity $\mathit{\Delta}I$ between the simplified and full model by Schlamp et al. [89] is less than 0.2 %. Hence, the presented simplifications and assumptions are justified.

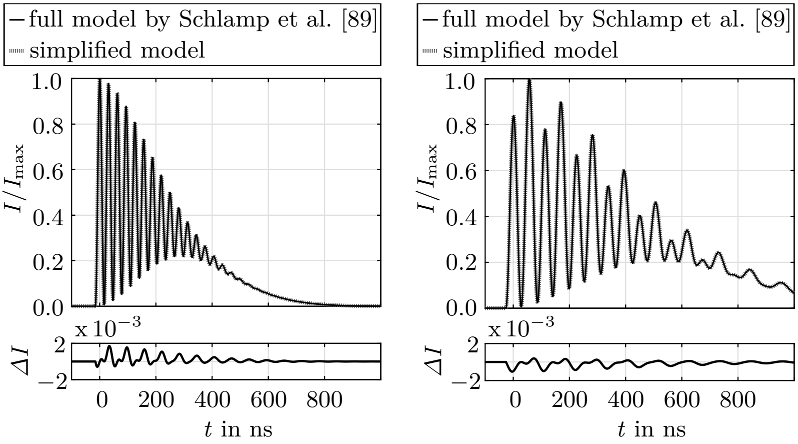

(a) Argon at 6 MPa and 609 K with non–resonant fluid behaviour.

(b) CO_2 at 1 MPa and 299 K with resonant fluid behaviour.

Figure 4.4: Comparison of theoretical LITA signals with non–resonant and resonant fluid behaviour using the LDL of the full model by Schlamp et al. [89] compared to the presented, simplified model (equation (4.4)). Input parameters are listed in Tab. 4.1.

Small detector limit for single–mode data evaluation

The small detector limit model takes the position of the detector with respect to the wave vector of the signal beam $\boldsymbol{k}_{\text{sig}}$ into account. Since prior to each measurement, the coupler, see C in Fig. 3.8, in front of the detector is aligned resulting in a maximised signal, we assume perfect alignment between detector and signal beam. This results in the following definition of the time–dependent dimensionless diffraction efficiency $\Psi(t)$

$$\begin{aligned}\Psi(t) \propto &\{\mathcal{A}_{P1}\Sigma_{P_1} + \mathcal{A}_{P2}\Sigma_{P_2} + \mathcal{A}_T\Sigma_T\} \\ &\{\mathcal{A}_{P1}{}^*\Sigma_{P_1}{}^* + \mathcal{A}_{P2}{}^*\Sigma_{P_2}{}^* + \mathcal{A}_T\Sigma_T{}^*\} \ .\end{aligned} \tag{4.5}$$

Note that the SDL in equation (4.5) differs from the large detector model presented in equation (4.4) only due to the terms of exponential decay in the first and third row of equation (4.4). A detailed comparison is presented in section 5.1.

Theoretical signals with non–resonant and resonant fluid response using the full model and the simplified model based on equation (4.5) are shown in Fig. 4.5. Model input parameter and ambient conditions are listed in Tab. 4.2.

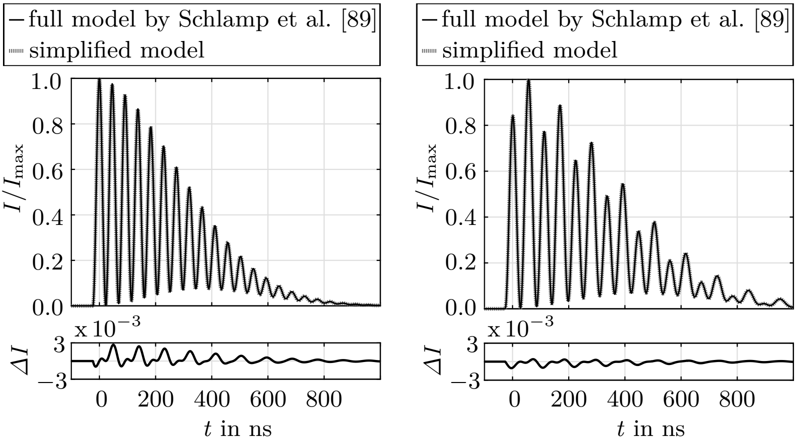

(a) Argon at 1.5 MPa and 296 K with non–resonant fluid behaviour.

(b) CO_2 at 1 MPa and 301 K with resonant fluid behaviour.

Figure 4.5: Comparison of theoretical signals using the SDL of the full model by Schlamp et al. [89] compared to the simplified model (equation (4.5)). Input parameters are listed in Tab. 4.2.

Since the deviation ΔI between the simplified and full model by Schlamp et al. [89] is less than 0.3 %, the used simplifications are justified.

Table 4.2: Overview of ambient conditions and input parameters for model comparison in Fig. 4.5. Fixed input parameters: $\Lambda = 29.47\,\mu\text{m}$; $\sigma = 151\,\mu\text{m}$; $\omega = 131\,\mu\text{m}$. Volume viscositiy for CO_2 is computed according to [51]. Thermodynamic data are taken from [56].

ambient conditions			input parameters					
fluid	p/ MPa	T/ K	$\lvert\mathcal{U}_\Theta/\mathcal{U}_{eP}\rvert$	c_s/ m s^{-1}	$\bar{\eta}$/ µm	Γ/ mm^2 s^{-1}	D_T/ mm^2 s^{-1}	κ
Ar	1.5	269	0.00	322	−56	1.102	1.365	1.70
CO_2	1.0	301	0.05	263	−56	1.382	1.024	1.35

4.3.2 Calibration of optical parameters

The presented theoretical model and frequency analysis of a LITA signal requires a deep understanding of the inherent non–linear optical processes, such as phonon–photon and thermon–photon interaction, presented by Cummings et al. [21]. Additionally, equations (4.4) and (4.5) depend on the beam waist of the excitation beam ω and the magnitude of the grating vector q. Both are highly vulnerable to distortions by turbulence and convective transport processes on similar time scales. By averaging the signal over a certain number of laser pulses the signal is smeared. Consequently, the effects of shot to shot variations in turbulence and convective processes, laser noise, jitter, and drift are minimised. Application of equations (4.1), (4.4) and/or (4.5) to measure speed of sound and acoustic damping rate requires a thorough calibration of the spacing of the optical grid $\mathit{\Lambda}$ and the Gaussian half–width ω of the excitation beam. Therefore, calibration of these optical parameters of the LITA arrangement is done in well-known, controlled, quiescent conditions.

Evaluation of the optical interference grid spacing

The optical interference grid spacing $\mathit{\Lambda}$ is calibrated using measurements in pure nitrogen and pure argon for atmospheric conditions up to 700 K and 8 MPa. Assuming non–resonant fluid behaviour the grid spacing is characterised by equation (4.6), with λ_{exc} being the excitation wavelength, f_{exc} the focal length and $\mathit{\Delta} y_{\mathrm{exc}}$ the beam distance of the excitation beams in front of the lens.

$$\Lambda(\mathit{\Delta} y_{\mathrm{exc}}, f_{\mathrm{exc}}, \lambda_{\mathrm{exc}}) = 2\frac{c_s}{\mathit{\Omega}_{2c_s}} \tag{4.6}$$

The beat frequency of the non–resonant LITA signal $\mathit{\Omega}_{2c_s}$ is hereby computed using the frequency analysis and filter methodology presented in the previous section, whereas the speed of sound c_s is taken from Lemmon et al. [56]. It is important to emphasise that the optical interference grid spacing is, as shown by Li et al. [57], solely dependent on the geometrical and optical parameters of the optical setup and, hence, independent of the refractive index of the probed environment. For calibration, only nitrogen and argon cases averaged over at least 100 valid single shot signals are used to ensure a small signal to noise ratio and a minimal influence of scattered light. For the low frequency LITA setup, the calibration procedure yields a grid spacing of the measurement volume of $\mathit{\Lambda}_{\mathrm{cal}} = 30.69 \pm 0.05\,\mu\mathrm{m}$ for all measurements before 08/2019 and

$\Lambda_{\text{cal}} = 29.47 \pm 0.05\,\mu\text{m}$ for all measurements after 10/2019. This distinction is necessary, due to a slight alteration in the beam alignment resulting from the applied optimisation depicted in Fig. 3.10 between those dates. For the high–speed LITA arrangement with a BE adjusted for large and small measurement volumes, calibration results in a grid spacing of $\Lambda_{\text{cal}} = 29.75 \pm 0.07\,\mu\text{m}$ and $\Lambda_{\text{cal}} = 29.63 \pm 0.17\,\mu\text{m}$, respectively.

Calibration of the Gaussian half-width of the excitation beams

For the calibration of the Gaussian half–width of the excitation beams ω, the excitation beam size is extracted from the time–domain of recorded LITA signals using the previously presented simplified theoretical models. Note that ω has been chosen as calibration parameter, since a direct measurement is due to the high laser intensity not possible and data sheet specification are not applicable due to the beam expander. To ensure signal quality, only previously inspected mean LITA signals averaged over at least 10 valid single shot signals are used. Argon is chosen as the calibration fluid for two reasons. First, due to the absorption cross–sections of argon, resonant fluid behaviour can be a priori excluded. The non–resonant fluid behaviour of argon leads to a further simplified signal model independent from the thermal diffusivity D_T, see Schlamp et al. [89] and Steinhausen et al. [107]. Second, as previously presented in Fig. 2.5, the volume viscosity in gaseous argon at low densities is negligible compared to the shear viscosity. Concordantly, acoustic damping rates are estimated by the expression for the classic acoustic damping rate $\Gamma_{c,\text{NIST}}$ defined by equation (2.15) using thermodynamic data taken from the NIST database by Lemmon et al. [56].

To acquire the Gaussian half–width of the excitation beams ω_{LITA} from the time–domain of detected, filtered, and averaged LITA signals, curve fitting with the simplified model presented in the previous section is used. A robust non–linear least–absolutes fit applying the Levenberg–Marquardt algorithm is utilised. For this the robust fit option Least Absolute Residuals (LAR) in the non–linear fit class in Matlab R2018a (The MathWorks Inc.) [61] is applied. The LAR method, which optimises the fit by minimising the absolute differences of the residual rather than the squared differences [61], has been chosen instead of the approach using bisquare weights. This is justified by the fact that the filtered and averaged signals experience no outliers. In case of signals detected with a MM fibre, the LDL is applied, while for SM fibre measurements the SDL is used. A detailed discussion on the selection of the detector limit follows in section 5.1. In case of the calibration curve fit, the constant input parameters are the calibrated grid spacing Λ_{cal}, the classic acoustic damping rate $\Gamma_{c,\text{NIST}}$ as well as the Gaussian half–width σ_{th} of the interrogation beam. The latter is estimated according to laser data sheet specification. Output parameters are the Gaussian half–width of the excitation beam ω, the speed of sound c_s, the beam misalignment $\bar{\eta}$, and the temporal offset t_0. Exemplary curve fits for the different LITA arrangements and detector configuration are depicted in Fig. 4.6. The operating conditions, input parameters, and results are listed in Tab. 4.3. The number of single shot signals used for averaging is denoted with o and measurement uncertainties are listed using a 68% confidence interval.

Table 4.3: Overview of operating conditions, input parameters and results of the calibration cases shown in Fig. 4.6. Curve fitting is used to estimate ω. Argon is used as calibration fluid. The Gaussian half–width of the interrogation beam is set to $\sigma_{\text{th}} = 151 \pm 16\,\mu\text{m}$. Uncertainties are listed using a 68% confidence interval. Thermodynamic data are taken from Lemmon et al. [56].

	operating conditions			input parameters		results
Case	p_{ch} in MPa	T_{ch} in K	o	Λ_{cal} in µm	$\Gamma_{c,\text{NIST}}$ in $\text{mm}^2\,\text{s}^{-1}$	ω_{LITA} in µm
129	6.0 ± 0.05	609 ± 6.7	4168	29.47 ± 0.05	1.02 ± 0.02	228 ± 1
162	1.5 ± 0.05	296 ± 0.4	1863	29.47 ± 0.05	1.10 ± 0.04	132 ± 40
355	5.0 ± 0.05	301 ± 0.6	5787	29.75 ± 0.07	0.36 ± 0.01	283 ± 18
387	4.0 ± 0.05	297 ± 0.4	3116	29.63 ± 0.17	0.44 ± 0.01	140 ± 37

Comparing the resulting Gaussian half–width of the excitation beam ω_{LITA} monitored using a MM fibre and fitted using the LDL (Case 129) with the values from SM fibre detection and SDL model (Case 162, 355, 387), the measurement uncertainties of MM fibre results are at least one magnitude below the SM detection. The reason for this observation lies in a stronger interdependency of ω and σ for the SDL. Within the latter, the measurement error is predominantly resulting from the uncertainty of σ, while in the LDL the beam misalignment $\bar{\eta}$ counteracts this dependency. However, since MM detection is more prone to light scattering problems and errors due to beam misalignment, SM fibres are generally superior for strong, well aligned LITA signals. Additionally, the differences between the measured LITA signal and the curve fit ΔI in Fig. 4.6 are of an order of magnitude of $\mathcal{O}(\Delta I) = 10^{-2}$, whereas the deviation of the simplified and full model by Schlamp et al. [89] depicted in Fig. 4.5 and Fig. 4.4 presents with $\mathcal{O}(\Delta I) = 10^{-3}$. Since the model deviations are one magnitude below the curve fitting accuracy the model simplifications are applicable and show only a minor influence on the results.

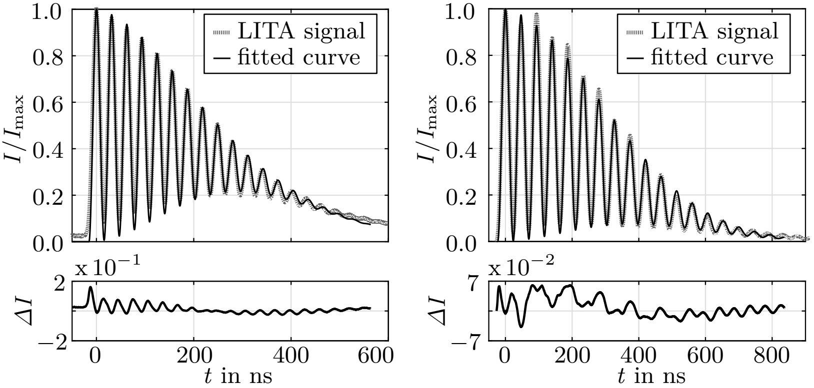

(a) Case: 129; low frequency LITA setup with MM fibre; LDL applied for curve fitting.

(b) Case: 162; low frequency LITA setup with SM fibre; SDL applied for curve fitting.

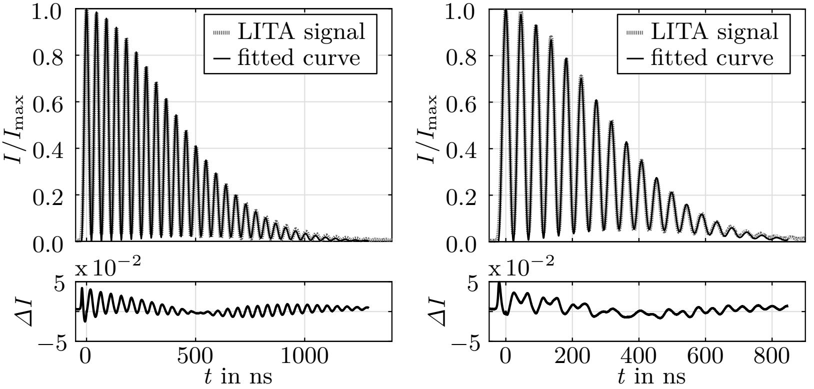

(c) Case: 355; high–speed LITA setup with SM fibre; BE adjusted for large optical interference pattern; SDL applied for curve fitting.

(d) Case: 387; high–speed LITA setup with SM fibre; BE adjusted for small optical interference pattern; SDL applied for curve fitting.

Figure 4.6: Measured LITA signals with non–resonant fluid behaviour in pure argon with curve fitting results used for calibration. Input operating conditions, input parameters, and results are listed in Tab. 4.3.

CHAPTER 5

Juxtaposition of signal modelling approaches and validation

Reliable data, extracted with the methodology presented in the previous chapter, require a theoretical model well–suited for the used optical arrangement as well as a thorough validation. In this chapter the two signal presented modelling approaches are juxtaposed and a recommendation on the best suited model is given. Moreover a validation of both the time–based signal modelling and the frequency analysis is presented.

5.1 Differences of the small and large detector limit model

Based on the derivation by Schlamp et al. [89], the differences in model limits are clear. Since the small detector limit assumes an infinitesimal detector size, it is solely applicable for investigations with a strong spatial filtering prior to detection. In the used LITA setup spatial filtering is performed by optical fibres. While the assumption of a infinitesimal detector can be justified for a SM fibre with a diameter of 4 µm, using MM fibres with a diameter of 25 µm does not provide sufficient spatial filtering to hold this assumption. Hence, for MM fibres the large detector limit with an infinite integration over the detection angle is used, whereas for the SM fibre both model limits are applicable.

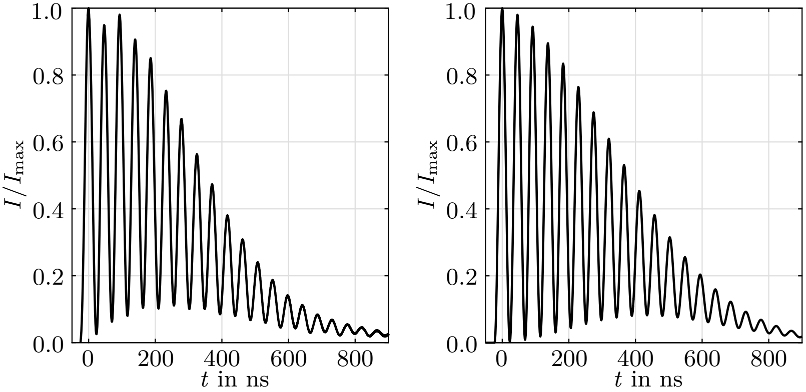

(a) Detected signal; low frequency LITA setup with SM fibre.

(b) Theoretical signal applying the SDL model.

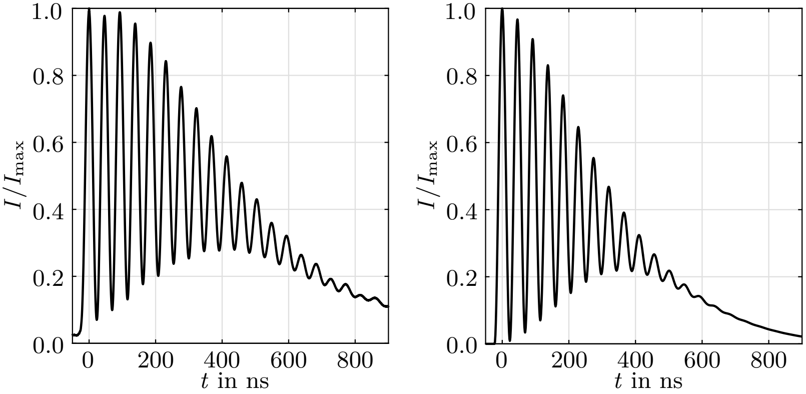

(c) Detected signal; low frequency LITA setup with MM fibre.

(d) Theoretical signal applying the LDL model.

Figure 5.1: Comparison of measured and theoretical LITA signals using the small and large detector limit (SDL/LDL) for pure argon at 2 MPa and 295 K. The measured signals are detected using SM and MM–fibres. Model input parameters: $\Lambda = 29.47\,\mu\text{m}$; $\sigma = 151\,\mu\text{m}$; $\omega = 190\,\mu\text{m}$; $\bar{\eta} = -66\,\mu\text{m}$; $\Gamma = 0.8309\,\text{mm}^2\,\text{s}^{-1}$; $c_s = 322\,\text{m}\,\text{s}^{-1}$. Necessary thermodynamic data are taken from Lemmon et al. [56].

Figure 5.1 depicts therefore two theoretical signals computed with the simplified small and large detector limit, presented in section 4.3.1. The theoretical signals are depicted together with two recorded LITA signals using a SM and a MM fibre. The detected signals are obtained in an argon atmosphere at 2 MPa and 295 K. The comparison shows that the theoretical signal presented in Fig. 5.1b computed with the SDL model reproduces more closely the experimental signal detected with a SM fibre depicted in Fig 5.1a. Note however that the theoretical signal calculated with the LDL agrees well with the recorded signal using a MM fibre presented in Fig. 5.1c. To corroborate the suggestion to favour the SDL for LITA signals recorded with a SM fibre, a direct comparison of curve fitting results used for both calibration and thermodynamic data extraction is presented in the following.

A juxtaposition of the curve fitting results applied to calibrate the Gaussian half–width of the excitation beam using both the small and large detector limit is presented in Fig. 5.2. The operating conditions, input parameters, and curve fitting results are hereby listed in Tab. 5.1. Note that the presented measurement is averaged over 5787 valid single shot signals detected using the high–speed LITA arrangement with a BE adjusted for a large optical interference pattern and a single–mode fibre.

Table 5.1: Overview of operating conditions and results of the calibration case in argon used for model comparison in large optical interference patterns shown in Fig. 5.3. Curve fitting is used to estimate the Gaussian half–width of the excitation beam ω. Fixed input parameters: $\Lambda_{\mathrm{cal}} = 29.75 \pm 0.07\,\mu\mathrm{m}$; $\Gamma_{c,\mathrm{NIST}} = 0.36 \pm 0.01\,\mathrm{mm}^2\,\mathrm{s}^{-1}$; $\sigma_{\mathrm{th}} = 151 \pm 16\,\mu\mathrm{m}$. Uncertainties are listed using a 68% confidence interval. Thermodynamic data are taken from Lemmon et al. [56].

	operating conditions			results
Case	p_{ch} in MPa	T_{ch} in K	theoretical model	ω_{LITA} in µm
355a	5.0 ± 0.05	301 ± 0.6	small detector limit	283 ± 18
355b	5.0 ± 0.05	301 ± 0.6	large detector limit	333 ± 7

Comparing the fitted Gaussian half–width of the excitation beams ω_{LITA} reveals two major differences. First, the value of ω_{LITA} extracted with the LDL is higher as the one computed with the SDL. This result can be explained by the enhanced spatial filtering, leading to only a partial detection of the scattered signal beam. Second, the measurement uncertainty for the LDL is one magnitude below the SDL. This is due to the stronger interdependency of the Gaussian half–width of the interrogation and excitation beams in the SDL, as previously discussed in section 4.3.2.

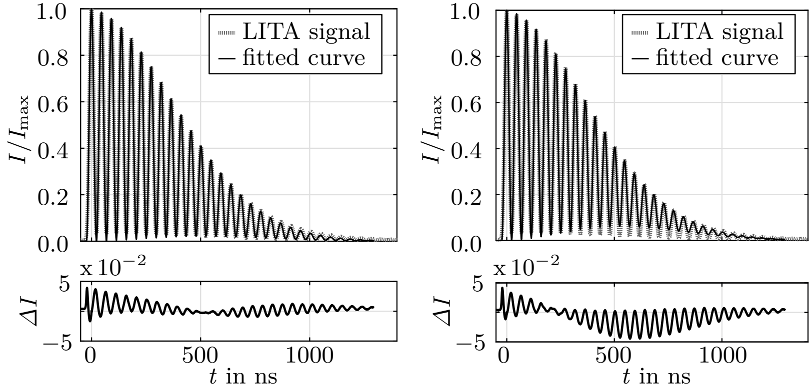

(a) Case: 355a; high–speed LITA setup with SM fibre; BE adjusted for large optical interference pattern; SDL applied for curve fitting.

(b) Case: 355b; high–speed LITA setup with SM fibre; BE adjusted for small optical interference pattern; LDL applied for curve fitting.

Figure 5.2: Comparison of curve fitting results for calibration using the small and large detector limit (SDL/LDL) for large optical interference patterns. Measured LITA signals with non–resonant fluid behaviour in pure argon are presented together with curve fitting results used for calibration. The signal is averaged over 5787 laser shots. Operating conditions, input parameters, and results are listed in Tab. 5.1.

The quality of the curve fit can be compared by the difference ΔI between the normalised signal intensity of the detected LITA signal and the curve fit as presented in Fig. 5.2. Since the LDL, depicted in Fig 5.2b, shows a higher deviation, the model is inferior to the SDL for modelling measurements conducted using a SM fibre, see Fig. 5.2a. The higher deviation is a result of the infinite integration over the detection angle in the LDL. This leads to a dependency of the signal offset on both the beam misalignment and the Gaussian half–width of the interrogation beam. In equation (4.4), this dependency is visible in the exponential terms solely depending on the Gaussian half–widths of the interrogation and excitation beams as well as the speed of sound. In contrast, for the SDL the signal offset solely depends on the beam misalignment included in $\Sigma_{P_{1,2}}$. Note that equation (4.4) and equation (4.5) only differ due to prior discussed terms of exponential decay.

Table 5.2 presents a comparison of speed of sound data and acoustic damping rates extracted using curve fitting with both the small and large detector limit together with their theoretical values taken from the NIST database by Lemmon et al. [56]. Since measurements are performed in an argon atmosphere at $p_{\mathrm{ch}} = 2\,\mathrm{MPa}$ and $T_{\mathrm{ch}} = 297.5\,\mathrm{K}$, the theoretical acoustic damping rate is estimated using its classical counterpart Γ_c. This assumption is valid due to the negligible volume viscosity in monoatomic gases at low density conditions, as presented in Fig. 2.5 and section 2.2.

Table 5.2: Overview of input parameters, curve fitting results and theoretical values of case 385 used for model comparison in small optical interference patterns shown in Fig. 5.3. Curve fitting is used to estimate speed of sound c_s and acoustic damping rate Γ. Operating conditions: $p_{\mathrm{ch}} = 2 \pm 0.05\,\mathrm{MPa}$; $T_{\mathrm{ch}} = 297.5 \pm 0.4\,\mathrm{K}$. Fixed input parameters: $\Lambda_{\mathrm{cal}} = 29.63 \pm 0.17\,\mathrm{\mu m}$; $\sigma_{\mathrm{th}} = 151 \pm 16\,\mathrm{\mu m}$. Uncertainties are listed using a 68% confidence interval. Thermodynamic data are taken from Lemmon et al. [56].

	input parameters		curve fitting results		theoretical values	
Case	ω_{cal} in µm	model limit	$c_{s,\mathrm{LITA}}$ in $\mathrm{m\,s^{-1}}$	Γ_{LITA} in $\mathrm{mm^2\,s^{-1}}$	$c_{s,\mathrm{NIST}}$ in $\mathrm{m\,s^{-1}}$	$\Gamma_{c,\mathrm{NIST}}$ in $\mathrm{mm^2\,s^{-1}}$
385a	134±40	small	318 ± 2	1.12 ± 3.0	323 ± 4	0.84 ± 0.03
385b	230±10	large	318 ± 2	7.76 ± 1.4	323 ± 4	0.84 ± 0.03

As for the curve fitting methodology for calibration a robust non–linear least–absolutes curve fit using a Levenberg–Marquardt algorithm is applied. In contrast to the calibration, input parameters are the grid spacing Λ_{cal} and the Gaussian half–widths ω_{cal} and σ_{th} of the excitation and interrogation beam, respectively. The recorded data are presented together with the curve fit in Fig. 5.3. The experimental signal is hereby averaged over 1644 single measurements detected using the high–speed LITA setup with a SM fibre and BE adjusted for a small optical interference pattern.

In case of the small detector model, the extracted acoustic damping rate as well as the speed of sound agree well with their theoretical values. The acoustic damping rate extracted using the large detector model, however, overpredicts the theoretical value by a factor of 9.2. Note that regardless of the applied LITA arrangement similar overestimations are observed for all measurements where the signal, detected with a SM fibre, is modelled using the LDL. Moreover, as is exemplarily depicted in Fig.5.3b, the quality of the LDL model curve fit is inferior to the SDL approach shown in Fig. 5.3a.

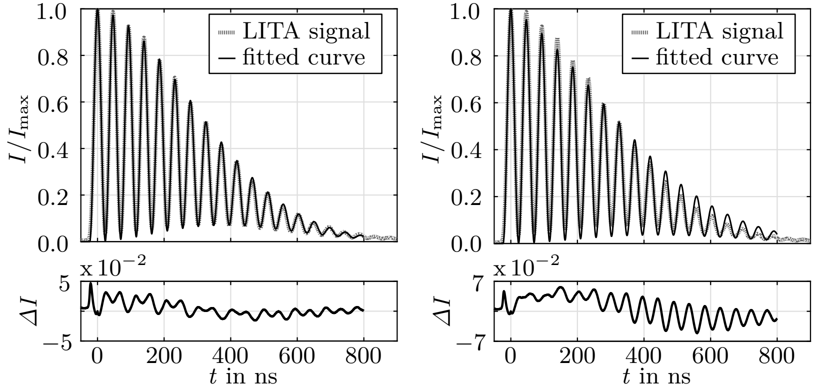

(a) Case: 385a; high–speed LITA setup with SM fibre; BE adjusted for small optical interference pattern; SDL applied for curve fitting.

(b) Case: 385b; high–speed LITA setup with SM fibre; BE adjusted for small optical interference pattern; LDL applied for curve fitting.

Figure 5.3: Comparison of curve fitting results for data extraction using the small and large detector limit (SDL/LDL) in case of small optical interference patterns. Measured LITA signals with non–resonant fluid behaviour in pure argon are presented together with curve fitting results used to estimate speed of sound c_s and acoustic damping rate Γ. The signal is averaged over 1644 laser shots. Operating conditions, input parameters, results, and theoretical values are listed in Tab. 5.2.

Based on the previous discussion and the presented curve fitting results the author recommends to model LITA signals detected with a high spatial filtering, as performed when using a SM fibre for signal detection, with the simplified SDL presented in section 4.3.1. In case of an optical arrangement with a MM fibre for spatial filtering the LDL has to be applied, since the assumption of an infinitesimal detector size does not apply.

5.2 Validation and uncertainty estimation of data processing

Extraction of transport properties, such as speed of sound data, acoustic damping rates, and volume viscosities, from recorded LITA signals, requires besides a thorough calibration of the optical setup a validation of the acquired transport properties. The validation of the speed of sound data obtained from both frequency analysis and curve fitting is presented in the following section. Additionally the acquired acoustic damping rates, absorption coefficients and volume viscosities are validated against experimental and theoretical values.

5.2.1 Speed of sound data validation for time and frequency analysis

Theoretical speed of sound data are accessible for a wide range of temperatures, pressures, pure fluids, and fluid mixtures within the NIST database by Lemmon et al. [56]. Consequently, validation in the whole operating range for all investigated fluids and fluid mixtures is possible. Speed of sound is hereby detected following the frequency analysis presented in section 4.2.

Speed of sound data calculated by frequency analysis

Validation of the frequency analysis is depicted in Fig. 5.4. The range of operating conditions in pressure and temperature for all fluids used in the presented validation are listed in Tab. 5.3. The absolute comparison between theoretical speed of sound data $c_{s,\mathrm{NIST}}$ and experimentally obtained values $c_{s,\mathrm{DFT}}$ using frequency analysis with equation (4.1) is shown in Fig. 5.4a. A first comparison of these absolute data points shows a good agreement between the theoretical and experimental data for a wide range. The relative distribution depicted in Fig. 5.4b shows the speed of sound ratio $c_{s,\mathrm{DFT}}/c_{s,\mathrm{NIST}}$. For clarity the distinction between the fluids argon, nitrogen, helium as well as the fluid mixtures is omitted, resulting in two distributions, one for non–carbon dioxide and the other for carbon dioxide. Validation using the relative distribution shows a good agreement between the measured speed of sound data and the theoretical values for all fluids and fluid mixtures except carbon dioxide. Assuming a Gaussian distribution, which can be justified based on the distributions shape with a kurtosis of 4.5 and a skewness acquired to be -0.024, the validation of all fluids and mixtures except carbon dioxide presents with a mean value of 0.9998 with a standard deviation of 0.0121. The distribution of the CO_2 data has a mean value of 1.062 with a standard deviation of 0.0161. The skewness for the CO_2 data is -0.17 with a kurtosis of 3.64.

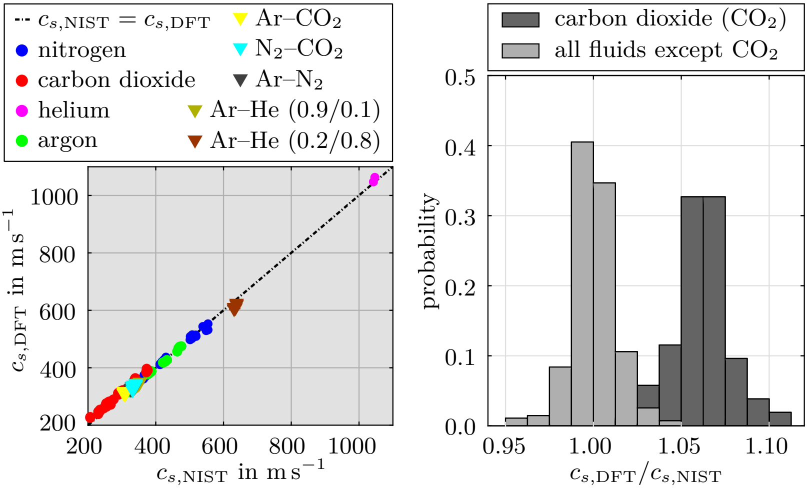

(a) Absolute comparison.

(b) Relative distribution.

Figure 5.4: Absolute comparison and relative distribution of the comparison of speed of sound data extracted using frequency analysis with theoretical values for operating conditions and fluids listed in Tab. 5.3. Speed of sound data are calculated using the frequency analysis presented in section 4.2. Data for validation are taken from Lemmon et al. [56].

It is important to emphasise that using a confidence interval of 95 % the measurement uncertainty of the acquired speed of sound is below 1.21 % for single shot measurements for carbon dioxide and below 1.15 % in all atmospheres except CO$_2$. However, based on the presented distribution the uncertainty is approximately 2.4 % for non carbon dioxide atmospheres and 3.2 % for CO$_2$. Hence, the speed of sound can be extracted with a relative uncertainty rated at 2.4 % (3.2 % for CO$_2$) with a 95 % confidence interval. These results agree well with the accuracy determination based on the deviation of the interrogation beam crossing angle and the subsequent change of the order of Bragg diffraction by Richter et al. [85]. The reason for this increase in measurement uncertainty lies in minimal, unavoidable misalignments of the excitation beams due to beam steering effects in the investigated extreme environments.

The observed discrepancy between experimental and theoretical speed of sound data in the carbon dioxide distribution is most likely a result of residual moisture

Table 5.3: Operating conditions and fluids used for validation of measured speed of sound data extracted by frequency analysis.

fluids	mole fraction	pressure range in MPa	temperature range in K
nitrogen	N/A	0.5 to 8	294 to 714
argon	N/A	0.5 to 8	293 to 610
carbon dioxide	N/A	0.5 to 8	297 to 608
helium	N/A	5 to 6	301
argon–helium	0.2000 / 0.8000	1 to 8	301
argon–helium	0.9000 / 0.1000	5 to 8	301
argon–nitrogen	0.8000 / 0.2000	1 to 8	301
argon–CO_2	0.8000 / 0.2000	1 to 8	301
nitrogen–CO_2	0.7999 / 0.2001	0.5 to 8	301

in the experimental rig as previously discussed by Steinhausen et al. [107]. In addition to the observed deviation for carbon dioxide, a resonant fluid behaviour is observed. The latter intensifies with increasing pressure. However, based on the absorption cross–section of carbon dioxide such a resonant fluid response can be a priori excluded for the excitation wavelength of $\lambda_{\mathrm{exc}} = 1064\,\mathrm{nm}$. One and the most probable explanation for these resonant behaviours is residual moisture in the experimental setup and the peripheral pipe system presented in Fig. 3.6. Since water shares an absorption cross–section with the excitation wavelength, residual moisture would cause a resonant fluid response. This behaviour has previously been observed by Cummings [20]. Assuming the above hypothesis to be correct, the constant offset even for low mole fractions of water demonstrates quite nicely the sensitivity of the LITA technique on the concentration of a mixture. This sensitivity is essential in order to investigate mixing processes and extract mixture parameters, such as the mixing temperature or the mole fraction. To verify the robustness of the optical arrangement as well as the LITA technique itself additional investigations in carbon dioxide have been conducted. The objectives of these investigations are twofold. First, by drying the heatable chamber prior to carbon dioxide investigations and operating in the open mode configuration, see Fig. 3.6 for comparison, residual moisture in the pressure chamber itself is minimised. However, no influence on the fluid response has been observed. Since the purity of the carbon dioxide supply is high, the residual moisture is most likely a result of remaining water in the non–heatable peripheral fluid supply system and the pneumatic piston pump used for pressurisation. Second, an intensity study of systematic variation of the excitation pulse energy has been conducted. With these experiments two other possible explanations, namely spontaneous Raman scattering or optical breakdown, for the observed resonant fluid response have been eliminated from consideration. As described by Stampanoni-Panariello et al. [100], an optical breakdown of the fluid occurs due to high excitation pulse energies leading to a change in fluid properties inside the probe volume. The latter causes a change in the temporal shape of the LITA signal. Regarding the possibility of spontaneous Raman scattering as an explanation for the resonant fluid response, different dependencies of the recorded signal intensity on the excitation beam pulse energy are used for elimination. Non–resonant, purely electrostrictive LITA signals are caused by Brillouin scattering, whereas a resonant fluid response is caused by the combination of Brillouin scattering and Rayleigh scattering. In the theoretical discussion presented by Stampanoni-Panariello et al. [100], the signal intensity of a detected LITA signal for both resonant and non–resonant fluid behaviour experiences a quadratic dependency on the pulse energies of the excitation beams. In contrast, spontaneous Raman scattering experiences a linear dependency on the incident intensity, as discussed by Powers [80]. In case of spontaneous Raman scattering a systematic increase of the pulse energy starting at low energetic pulses, would favour the LITA fluid response over the effect of spontaneous Raman scattering. However, since no such behaviour and no change in the temporal signal profile could be observed for continuously increasing excitation pulse energies both optical breakdown and spontaneous Raman scattering are eliminated as possible explanations for the observed resonant fluid response. This leaves residual moisture as the most probable scenario.

Comparison of frequency analysis and curve fitting speed of sound results

Validation of the speed of sound data obtained using the time–based signal modelling approach presented in section 4.3 is performed by comparing the frequency–based results with the time–based curve fitting predictions. Similar to the curve fit in the calibration procedure the Gaussian half–width of the excitation beam in section 4.3.2, a robust non–linear least–absolutes curve fit using a Levenberg–Marquardt algorithm is applied. Input parameters are hereby the optical parameters of the LITA setup, namely the grid spacing Λ_{cal}, and the Gaussian half–widths ω_{cal} and σ_{th} of the excitation and interrogation beam. Figure 5.5 presents the comparison in the form of a relative distribution of the curve fitted results $c_{s,\mathrm{Fit}}$ divided by the frequency–based estimation $c_{s,\mathrm{DFT}}$. The kurtosis is 11.5 with a skewness of -0.019, leading to a leptokurtic distribution compared to a Gaussian distribution. The ratio of the fitted speed of sound to the frequency–based speed of sound $c_{s,\mathrm{Fit}}/c_{s,\mathrm{DFT}}$ lies fully inside the measurement uncertainty determined in the previous section. It can therefore be stated that the curve fitting predictions agree with the frequency–based results. The implications of this agreement are twofold. On one hand it validates the curve fitting methodology, on the other hand it demonstrates the accuracy of the frequency analysis presented in the previous chapter.

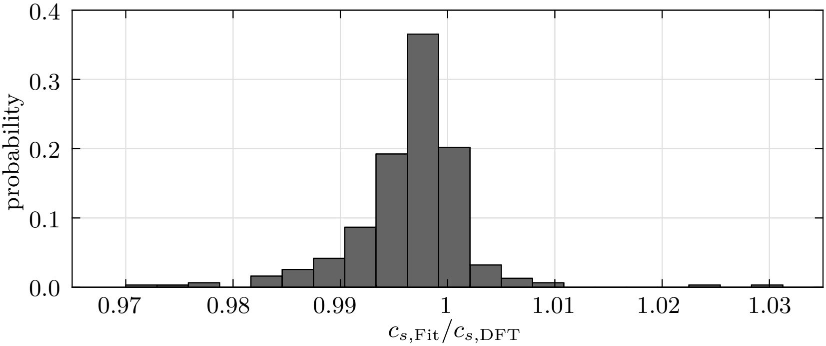

Figure 5.5: Relative distribution of the comparison of speed of sound data extracted using curve fitting ($c_{s,\mathrm{Fit}}$) and frequency analysis ($c_{s,\mathrm{DFT}}$). The skewness of the distribution is acquired to be −0.019 with a kurtosis of 11.5.

5.2.2 Transport property validation based on time–based curve fitting results

Acoustic damping rates are obtained from the time–domain of averaged LITA signals by applying a curve fitting algorithm similar to the one used for determining the Gaussian half–width of the excitation beam ω_{cal} presented in section 4.3.2. A robust non–linear least–absolutes curve fit employing a Levenberg–Marquardt algorithm is utilised. To ensure the robustness of the curve fit the LAR option in Matlab R2018a (The MathWorks Inc.) [61] is used. Input parameters for the curve fitting algorithm to determine speed of sound, acoustic damping rate and thermal diffusivity (only for resonant fluid response) are the optical parameters of the used LITA arrangement. These parameters are the calibrated optical grid spacing Λ_{cal}, the calibrated Gaussian half–width of the excitation beam ω_{cal}, and the theoretical Gaussian half–width of the interrogation beam σ_{th}. The latter is computed from data sheet specifications. Acoustic damping depends on both volume and shear viscosities. Unfortunately, experimental, numerical, and theoretical data for volume viscosities in gases at high temperature/pressure environments are rare. The validation presented in the following is therefore limited to comparisons with dilute gas models and experimental results at pressures up to 2.5 MPa.

Acoustic damping rates at low pressure and temperature conditions

The ratio between acoustic damping rates obtained by LITA $\mathit{\Gamma}_{\mathrm{LITA}}$ and the classical acoustic damping rate $\mathit{\Gamma}_{c,\mathrm{NIST}}$ taken from the NIST database by Lemmon et al. [56] is presented in Fig. 5.6 for investigations in pure argon, nitrogen, and carbon dioxide. The LITA measurements conducted in this work (dots with error bars) are compared to experimental studies by Li et al. [57] (triangle) obtained using LIGS. For the LITA results the temperature is indicated by colour and measurement uncertainties are displayed using a 95 % confidence interval. Note that points at similar pressure conditions indicate experiments, which were conducted on different days. Deviations between those points are caused by beam steering effects or are a result of staining of the quartz windows. The latter can influence the Gaussian beam width of the excitation beams without changing the beam crossing angle. Since the data measured by Li et al. [57] are limited to temperatures of 293 K only LITA measurements in a similar temperature range are shown. Note that Li et al. [57] apply an optical arrangement with a grid spacing of $\mathit{\Lambda} = 22\,\mu\mathrm{m}$ and unfocused beams. The latter leads to simplified modelling equations with only the optical grid spacing as an optical calibration parameter. The experimental results for nitrogen (Fig. 5.6a) and argon (Fig. 5.6b) conducted in this work slightly underestimate the data provided by Li et al. [57], while the data are still included in the presented confidence interval. The explanations for this deviation are threefold. First, the theoretical model applied by Li et al. [57] is a simplified model provided by Cummings [19], which does not take finite beam size effects into account. While the model is generally applicable to the observation with unfocused beams performed by Li et al. [57], slight deviations in the acoustic damping rate could occur. Note that the accuracy of the curve fit in the work by Li et al. [57] is similar to the one presented in this work. Second, the difference in temperatures, which is 293 K for the data by Li et al. [57] versus approximately 300 K for the LITA measurements, might be a source of discrepancy. Third, the difference in optical grid spacing, $\Lambda_{\mathrm{Li}} = 22\,\mu\mathrm{m}$ compared to $\Lambda_{\mathrm{LITA}} \approx 30\,\mu\mathrm{m}$, is another possibility for the observed deviation. Li et al. [57] discussed that the extracted acoustic damping rate ratios depend on the value of the optical grid spacing. However, this hypothesis is only corroborated by comparing signal shapes without computing the acoustic damping rate ratio.

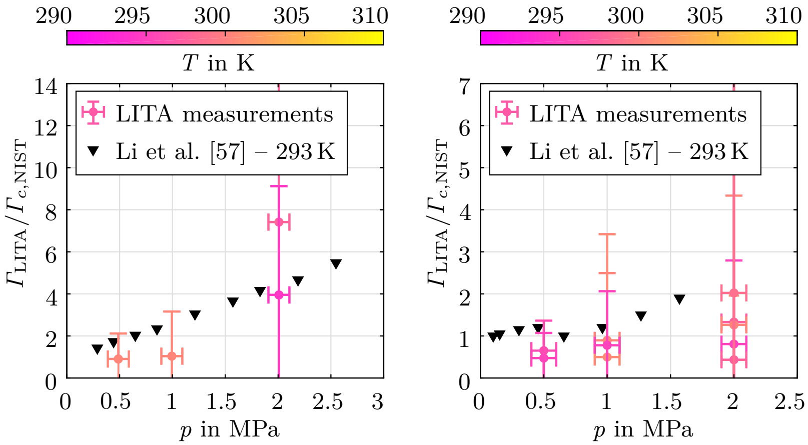

(a) Nitrogen.

(b) Argon.

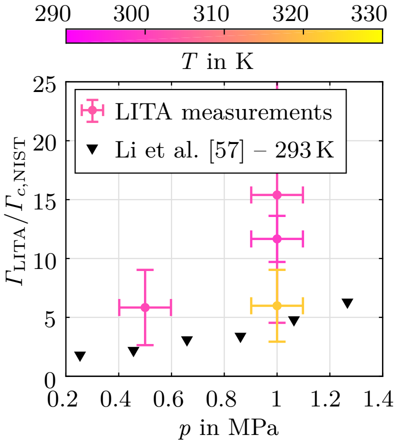

(c) Carbon dioxide.

Figure 5.6: Acoustic damping rate ratio $\Gamma/\Gamma_{c,\mathrm{NIST}}$ over pressure p for pure argon, nitrogen, and carbon dioxide for low pressure and temperature conditions detected with a grid spacing of $\Lambda_{\mathrm{cal}} \approx 30\,\mu\mathrm{m}$. Values are compared with experimental observations measured with a grid spacing of $\Lambda = 22\,\mu\mathrm{m}$ by Li et al. [57]. Uncertainties are displayed using a 95 % confidence interval. Thermodynamic data to compute Γ_c are taken from Lemmon et al. [56].

Since the damping of the signal oscillation depends on $\varGamma q^2$, see equation (4.3), this observation could entirely be a result of a change in q, which is directly related to $\varLambda$. Hence, further investigations are necessary to fully explain this observation. Unfortunately, a significant change in grid spacing would imply a complete new alignment of the excitation and interrogation beams. A parametric study on the influence of the grid spacing was therefore not feasible in this work.

Figure 5.6c depicts acoustic damping rate ratios $\varGamma_{\text{LITA}}/\Gamma_{c,\text{NIST}}$ for pure carbon dioxide at pressures between 0.5 and 1.3 MPa. In contrast to the nitrogen and argon studies, the LITA investigations slightly overestimate the data presented by Li et al. [57]. However, since Li et al. [57] operated at slightly lower temperatures compared to the LITA studies ($T_{\text{Li}} = 293\,\text{K}$ versus $T_{\text{LITA}} = 300\,\text{K}$), higher volume viscosities are expected as discussed by Kustova et al. [51]. Besides the above mentioned reasons for the observed deviation, the residual moisture in the probed carbon dioxide atmosphere, can be another explanation for the slight overestimation of the acoustic damping rate ratio. As presented by Li et al. [58], in mixtures an additional acoustic absorption due to species diffusion arises. As stated before, the difference in grid spacing delivers a possible explanation for the overestimation. In case of carbon dioxide this could be a result of an excitation of the vibrational and/or rotational degrees of freedom by the frequency of the induced acoustic wave. As discussed in section 2.2.1, this leads to an increased loss of acoustic energy and consequently in an increase of the acoustic attenuation. The latter will be outlined in the next section.

Acoustic absorption in carbon dioxide at dilute gas conditions

The acoustic attenuation of a fluid can be expressed by the dimensionless acoustical absorption coefficient per wavelength α_λ defined by equation (2.17). By relating the coefficient α_λ to the frequency of the acoustic wave per pressure Shields [94, 95] experimentally observed an increase of acoustic attenuation related to the acoustic frequency–pressure ratio in CO_2. The measurements were conducted at atmospheric pressure conditions and temperatures between 303 and 578 K using the tube method, which detects the acoustic absorption using a highly sensitive customised microphone. The experimental results presented by Shields [94, 95] (triangle) are depicted in Fig. 5.7 together with the LITA measurements (dots with error bars) for densities below $75\,\text{kg}\,\text{m}^{-3}$. Note that while the data has first been published by Shields [94, 95] the data presented in Fig. 5.7 are processed values taken from Arima et al. [3].

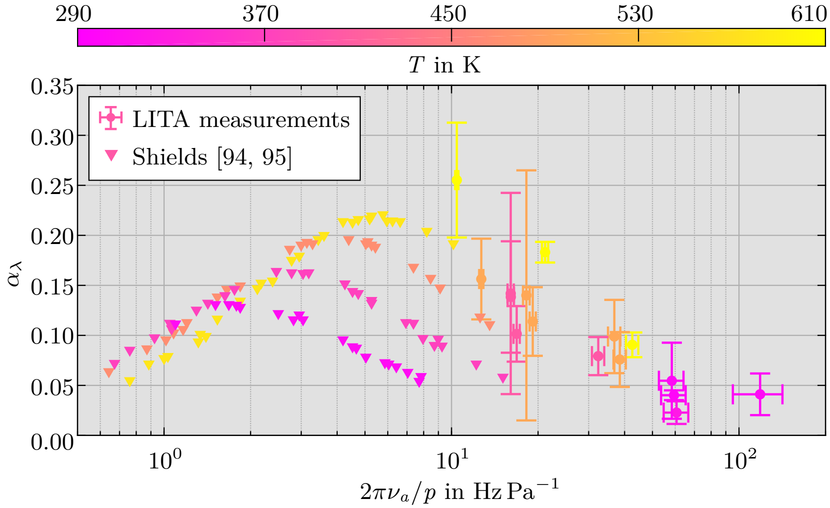

Figure 5.7: Acoustic absorption coefficient per wavelength α_λ over angular frequency of the acoustic wave per pressure $2\pi\nu_a/p$ for pure carbon dioxide at densities below $75\,\mathrm{kg\,m^{-3}}$. α_λ is calculated with equation (2.17) using LITA extracted acoustic damping rates Γ_{LITA}. Values are compared with experimental investigations by Shields [94, 95]. Uncertainties are displayed using a 95 % confidence interval. Necessary thermodynamic data are taken from Lemmon et al. [56].

The acoustic absorption coefficient per wavelength α_λ over the angular frequency of the acoustic wave per pressure $2\pi\nu_a/p$ is shown for pure carbon dioxide. The temperature of the probed fluid is hereby indicated by colour. Measurement uncertainties are presented using a 95 % confidence interval. Note that the acoustic wave frequency in carbon dioxide for the LITA arrangement lies within the MHz–regime, while the experiments by Shields [94, 95] are performed in the kHz–regime. Since LITA investigations are conducted at higher frequencies and pressures, a direct comparison is not possible. Nevertheless, the LITA results extend the data by Shields [94, 95] nicely. Especially the temperature dependency as well as the increase in acoustic attenuation detected by Shields [94, 95] are observed in the LITA results.

According to Ejakov et al. [27] and discussed in section 2.2.1, this behaviour is caused by the fact that vibrational and/or rotational degrees of freedom are excited by the induced acoustic wave, resulting in increased acoustic losses and, hence, a stronger acoustic attenuation. Consequently, the interactions of the molecular degrees of freedom with the frequency of the induced acoustic wave that are observed within the whole operating range need to be considered. To avoid this, higher acoustic wave frequencies (lower grid spacings) are necessary. Unfortunately, this is not feasible with the current setup. Note that a similar dependency could not be observed for measurements in nitrogen and argon.

Volume viscosity data at dilute gas conditions

Figure 5.8 shows a comparison of experimental and theoretical volume viscosities μ_v over density ϱ for pure carbon dioxide at low densities. Experimental vales are acquired using time–based LITA signal evaluation (dots with error bars), while theoretical values are computed with the dilute gas model by Kustova et al. [51] and calculated at the LITA operating conditions (triangle). The temperature is hereby indicated by colour. Measurement uncertainties are presented using a 95 % confidence interval.

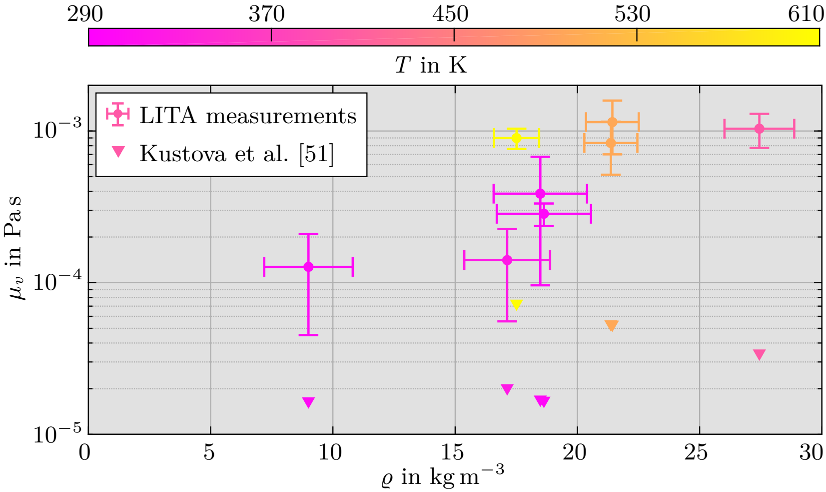

Figure 5.8: Comparison of theoretical and experimental volume viscosity μ_v over density ϱ for pure carbon dioxide at low densities. Experimental volume viscosities are derived from equation (2.16) using LITA extracted acoustic damping rates Γ_{LITA}. Values are compared with theoretical estimations with the model by Kustova et al. [51]. Uncertainties are displayed using a 95 % confidence interval. Necessary thermodynamic data are taken from Lemmon et al. [56].

A qualitative comparison presents a similar trend in temperature for both experimental and theoretical results. However, quantitative comparisons even for low densities show an overestimation in the order of one magnitude for the LITA results versus the theoretical values. This deviation could be a result of the difference in pressure, since the presented LITA results are measured at pressures between 0.5 and 2 MPa and the model by Kustova et al. [51] is derived and validated for a pressure of 0.1 MPa. Slight deviation for higher density/pressure conditions between model and LITA measurement are therefore expected. Nevertheless, the magnitude in deviation has be further examined.

One possible explanation can be seen in the pressure dependency of the internal relaxation time. The latter is assumed to be reciprocally dependent on pressure as discussed by Shields [94]. This leads to the nearly pressure independent volume viscosity model for dilute gases presented by Kustova et al. [51]. By considering molecular collisions and possible interdependencies with the internal degrees of freedom, the theoretical model predictions could be improved. The latter will be discussed in section 6.1.2. Moreover, the classical one–temperature model by Kustova et al. [51] does not consider the acoustic frequency related increase in acoustic attenuation, as observed in Fig. 5.7. The experimentally observed higher volume viscosities are therefore most likely a result of increases thermodynamic losses based on the excitation of vibrational and/or rotational degrees of freedom by the induced acoustic wave.

CHAPTER 6

Applying laser–induced thermal acoustics at extreme conditions

In the scope of this work laser–induced thermal acoustics is applied to investigate macroscopic fluid phenomena under extreme ambient conditions. First, the acoustic attenuation in pure carbon dioxide is examined in the gas and gas–like regime. Based on these studies volume viscosities and viscosity ratios for carbon dioxide under high pressure and temperature conditions are estimated. Note that experimental results for nitrogen and binary mixtures are presented in appendix B of this work. Second, to further characterise the probe volume of the high–speed laser–induced thermal acoustics arrangement and to investigate acoustic damping rates in gaseous mixture states, a jet mixing process of an argon jet in a nitrogen atmosphere under isothermal conditions is studied. At last, transient measurements in the wake of a free falling pre–heated acetone droplet evaporating in a nitrogen atmosphere at supercritical conditions are performed. The following chapter presents and discusses the results of these investigations together with their research objectives.

6.1 Principal investigations in sub- to supercritical fluids

Engineering processes, such as the Joule/Brayton cycle in gas turbines (Marchionni et al. [60]) or the application of methane for rocket propulsion (Pizzarelli et al. [78]), highlight the increasing importance of near- to supercritical fluid research. At conditions in the vicinity of the critical point the dynamic fluid response to perturbations is influenced by extrema in transport properties, such as thermal diffusivity and volume viscosity, see Fig 1.2. Especially the latter is of particular importance in numerical simulations, wherein Stokes' hypothesis is commonly applied. The assumption of negligible volume viscosity, which is assumed in Stokes' hypothesis, might no longer hold at near- to supercritical fluid conditions. Thus, its use has to be reconsidered. To assess the importance of volume viscosities, studies in carbon dioxide in its gas and gas–like states are conducted. CO_2 is selected based on its critical temperature $T_c = 304\,\mathrm{K}$ and pressure $p_c = 7.38\,\mathrm{MPa}$, as specified by Lemmon et al. [56]. Note that the sealing characteristics of the test rig have restricted measurements to the gas and gas–like regime of carbon dioxide as displayed in Fig. 1.1.

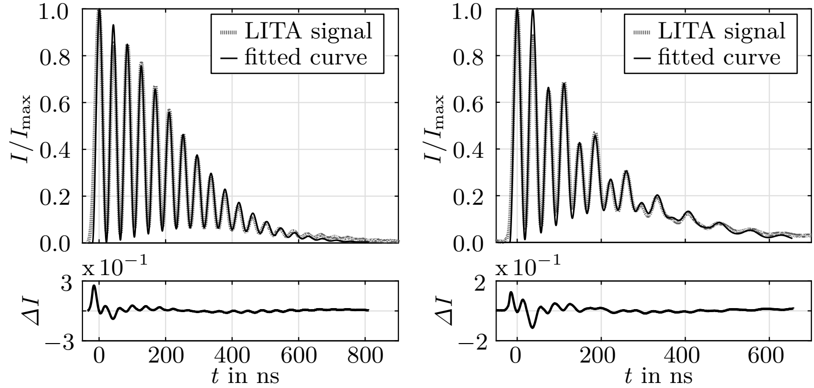

(a) Case 45, nitrogen: low frequency LITA setup with SM fibre; non–resonant fluid behaviour.

(b) Case 141, carbon dioxide: low frequency LITA setup with MM fibre; resonant fluid behaviour.

Figure 6.1: Curve fitting results and measured LITA signals in nitrogen and carbon dioxide. Fitting results are used to estimate speed of sound c_s and acoustic damping rate Γ. Operating conditions, input parameters, and results are listed in Tab. 6.1.

As an example, Figure 6.1 presents detected signals together with their curve fits recorded in a nitrogen and a carbon dioxide atmosphere. The operating conditions, curve fitting input parameters, and results are listed in Tab. 6.1.

Table 6.1: Overview of operating conditions, input parameters, and curve fitting results for nitrogen and carbon dioxide shown in Fig. 6.1. Curve fitting is used to estimate speed of sound c_s and acoustic damping rate $\mathit{\Gamma}$. Uncertainties are listed using a 68% confidence interval.

	operating conditions				input parameters	
Case	fluid	p_{ch} in MPa	T_{ch} in K	o	ω_{cal} in µm	$\mathit{\Lambda}_{\mathrm{cal}}$ in µm
45	N_2	6 ± 0.05	295 ± 0.7	11751	131 ± 40	30.68 ± 0.05
141	CO_2	4 ± 0.05	608 ± 5.3	5349	226 ± 4	29.47 ± 0.05

	input parameters		curve fitting results		
Case	σ_{th} in µm	model	$\lvert\mathcal{U}_\Theta/\mathcal{U}_{eP}\rvert$	$c_{s,\mathrm{LITA}}$ in $\mathrm{m\,s^{-1}}$	$\mathit{\Gamma}_{\mathrm{LITA}}$ in $\mathrm{mm^2\,s^{-1}}$
45	151 ± 16	small detector limit	0	365 ± 1	13.57 ± 5.4
141	151 ± 16	large detector limit	0.05	397 ± 1	54.26 ± 1.6

Note that the carbon dioxide signal is detected using a MM fibre, whereas the nitrogen measurement is performed with a SM fibre. While the SM fibre is generally superior to the MM fibre, strong beam steering effects caused by thermal fluctuations in the CO_2 case made a measurement with a MM fibre inevitable. In case of the carbon dioxide atmosphere, a resonant fluid behaviour is observed. As previously discussed, this is most likely a result of residual moisture in the peripheral pipe system. However, due to the low modulation depth of the thermal grating compared to the electrostrictive grating, $\lvert\mathcal{U}_\Theta/\mathcal{U}_{eP}\rvert < 0.05$, the resonant contribution of the fluid response is weak. The fitted thermal diffusivity does therefore not reveal physically reasonable results. Hence, it is not listed in Tab. 6.1.

An overview of the operating conditions' fluid states are presented in the reduced pressure p_r, reduced density ϱ_r diagram depicted in Fig. 6.2. The temperature is hereby indicated by colour. While most of the investigations are conducted in the gaseous state, three measurements are performed in the gas–like fluid regime. Note that the different fluid regimes are hereby based on microscopic investigations and sound dispersion measurements presented in Fig.1.1.

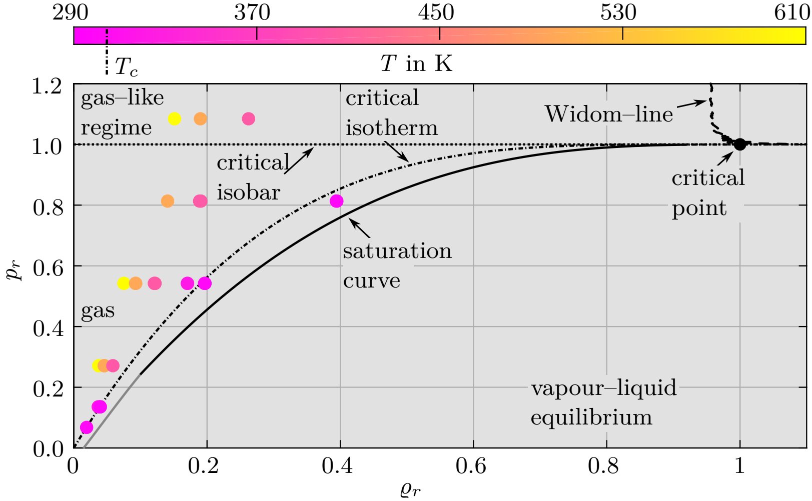

Figure 6.2: Thermodynamic fluid states of the operating conditions used for principal investigations in CO_2. Reduced pressure: $p_r = p/p_c$; reduced density: $\varrho_r = \varrho/\varrho_c$. Widom–line: line of maxima in c_p. Saturation curve: calculated values (black), visual extrapolation (grey). Thermodynamic data are taken from Lemmon et al. [56].

6.1.1 Acoustic absorption in carbon dioxide at dense gas conditions

In the previous chapter additional acoustic losses due to the acoustic excitation of the degrees of freedom in complex fluids are discussed and validated for measurements at dilute gas conditions. Note that the acoustic attenuation depends on the frequency of the acoustic wave per pressure. Figure. 6.3 shows the acoustical absorption coefficient per wavelength α_λ over the angular acoustical wave frequency per pressure $2\pi\nu_a/p$ for carbon dioxide at dilute to dense gas conditions. The absorption coefficient α_λ is hereby calculated with equation (2.17) by the LITA extracted acoustic damping rates Γ_{LITA}. Results presented by Shields [94, 95], which have been processed by Arima et al. [3], are indicated as triangles, while the data extracted from LITA signals by the curve fitting methodology are displayed as dots with error bars. The temperature of the probed atmosphere is shown as colour and measurement uncertainties of the LITA results are computed with a 95 % confidence interval. As suggested by Shields [94] the frequency axis is scaled logarithmically, leading to a bell–shaped attenuation spectrum for each temperature condition.

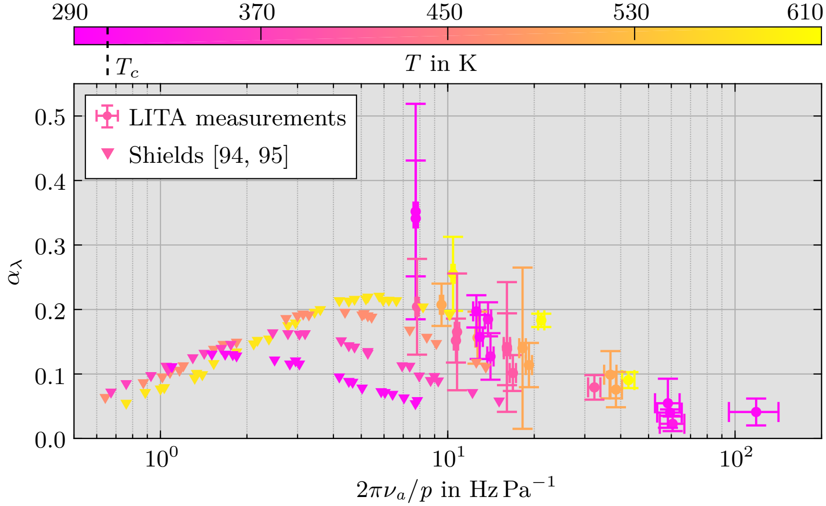

Figure 6.3: Acoustic absorption coefficient per wavelength α_λ over angular frequency of the acoustic wave per pressure $2\pi\nu_a/p$ for carbon dioxide. α_λ is calculated with equation (2.17) from LITA extracted acoustic damping rates Γ_{LITA}. Values are compared with results by Shields [94, 95]. Uncertainties are displayed using a 95 % confidence interval. Thermodynamic data are taken from Lemmon et al. [56].

In case of the LITA results it is important to emphasise that speed of sound c_s and, in case of a constant grid spacing, the acoustic frequency ν_a determined with equation (2.8) is almost independent of pressure. Concordantly, the changes in $2\pi\nu_a/p$ at constant temperature conditions of the LITA derived data are a consequence of variations in pressure rather than acoustic frequency. Note that based on the grid spacing the frequency of the induced acoustic sound waves are in the MHz–regime. In contrast, the investigations by Shields [94, 95] are conducted at atmospheric pressures with acoustic frequencies in the kHz range.

Comparison between the dilute gas results by Shields [94, 95] and the LITA measurements show an increase in acoustical absorption for high pressure conditions. Additionally, the qualitative temperature dependency for the dilute gas results by Shields [94, 95] is also visible in the dense gas LITA results. A sharp increase in α_λ is observed at 300 K for decreasing $2\pi\nu_a/p$, hence increasing pressure. Moreover, the measurements with the highest acoustic absorption coefficient of approximately 0.35 are recorded at $T_{\text{ch}} = 300\,\text{K}$ and

$p_{\mathrm{ch}} = 6\,\mathrm{MPa}$, which in reduced properties are $p_r = 0.81$ and $T_r = 0.98$. This increase in acoustical attenuation is therefore most likely related to the vicinity of the operating condition to the fluids critical point.

6.1.2 Volume viscosity in carbon dioxide at dense gas conditions

Experimental volume viscosities μ_v are estimated with equation (2.16) exploiting the difference between LITA extracted acoustic damping rates $\mathit{\Gamma}_{\mathrm{LITA}}$ and classical acoustic damping rates $\mathit{\Gamma}_{c,\mathrm{NIST}}$ calculated with values taken from the NIST database by Lemmon et al. [56]. The LITA extracted volume viscosities (dots) are plotted together with theoretical results computed with the model by Kustova et al. [51] (triangle) in Fig. 6.4 and Fig. 6.5a. Note that for clarity, measurement uncertainties in Fig. 6.5 are omitted, whereas in Fig. 6.4 uncertainties are displayed using a 95% confidence interval.

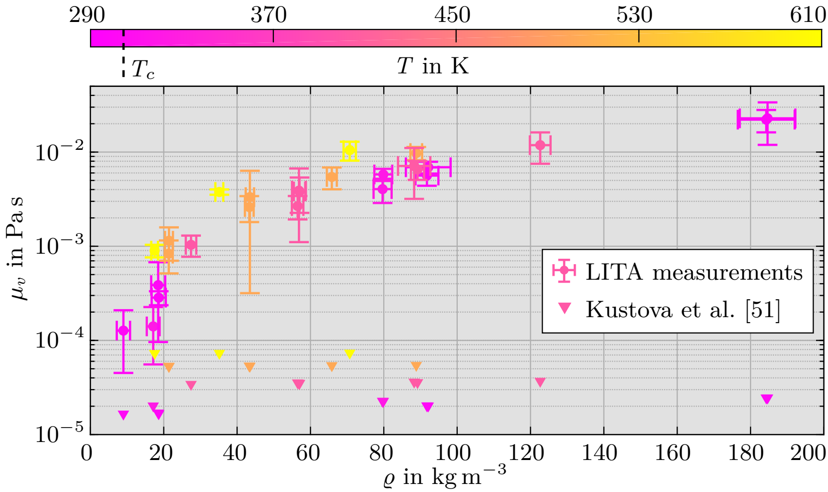

Figure 6.4: Theoretical and experimental volume viscosity μ_v over density ϱ for CO_2. Values are estimated with equation (2.16) from LITA extracted acoustic damping rates Γ_{LITA}. Values are compared with estimations based on the model for dilute gases by Kustova et al. [51]. Uncertainties are displayed using a 95% confidence interval. Necessary thermodynamic data are taken from Lemmon et al. [56].

For better comparison with all theoretical models presented in section 2.2, the viscosity ratio μ_v/μ_s is shown in Fig. 6.5b. The shear viscosity is hereby computed using the NIST database by Lemmon et al. [56]. In all graphs the temperature is indicated by colour.

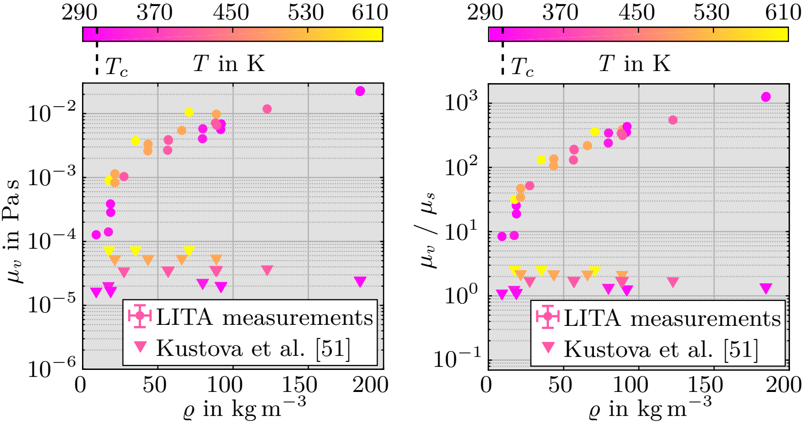

(a) Volume viscosity μ_v.

(b) Viscosity ratio μ_v/μ_s.

Figure 6.5: Theoretical and experimental volume viscosity μ_v and viscosity ratio μ_v/μ_s over density ϱ for CO_2. Values are calculated with equation (2.16) from the LITA extracted acoustic damping rates Γ_{LITA}. Results are compared to values based on the model for dilute gases by Kustova et al. [51]. Thermodynamic data are taken from Lemmon et al. [56].

As can be seen in Fig. 6.4 and Fig. 6.5, the LITA extracted volume viscosity rises rapidly with increasing pressure/density. Eventhough the investigated state at the highest density condition $\varrho = 185\,\mathrm{kg\,m^{-3}}$ is still subcritical ($p_r = 0.81$, $T_r = 0.98$, and $\varrho_r = 0.4$), the increase in volume viscosity clearly indicates its importance in the nearcritical fluid regime. Furthermore, both the theoretical values of the viscosity ratio based on the model for dilute gases by Kustova et al. [51] and the LITA measurements predict a volume viscosity with at least the same order of magnitude as the shear viscosity. This is even the case for measurements taken at low pressures conditions (0.5 MPa). Based on these values, Stokes' hypothesis to neglect volume viscosities compared to shear viscosities no longer holds. Hence, the consideration of volume viscosities in the derivation of stress tensor and entropy production becomes vital for reliable numerical results.

The comparison of theoretical and experimental results in Fig. 6.5 shows an increasing deviation between theoretical and experimental data for higher densities/pressures. However, the theoretical dependency on temperature discussed in section 2.2.2 is qualitatively correct. Since the volume viscosity model by Kustova et al. [51] assumes dilute gases, deviations are expected for elevated pressure/density conditions. Nevertheless, discrepancies with an order of nearly 3 magnitudes, cannot be solely explained by the dilute gas hypothesis. Whereas in the dilute gas model the energy distribution among the internal degrees of freedom contribute to the volume viscosity, dense gas effects are resulting mainly from elastic molecular collisions. Assuming a decoupled model, volume viscosities in dense gas conditions can be approximated by the sum of each contribution. This superposition is based on the approach used by Jaeger et al. [46]. However, examining the relative contributions of the volume viscosity solely due to elastic collisions presented in Fig 2.8, the theoretical considerations by Jaeger et al. [46] and Meier et al. [62] predict a ratio of $\mu_{v,\mathrm{coll}}/\mu_s < 1$ for the observed density regime. These investigations therefore only imply a moderate impact due to elastic collisions in the considered density range. Since the discrepancy between the LITA measurements and theoretical results by Kustova et al. [51] is much higher, as it can be explained by dense gas effects, the source of the strong deviation is not only a result of the dilute gas assumption. Note that while the Lennard–Jones model applied by Meier et al. [62] neglects the molecular structure and bonds in carbon dioxide, the EPM2 model proposed by Harris and Yung [40] used in the model by Jaeger et al. [46] considers the molecular structure by assuming rigid bond lengths with a flexible angular bond potential. However, since validation of the acoustic damping rate and acoustic absorption coefficient shows good agreement, see Fig 5.6 and Fig 5.7, the author is confident in the results of the conducted measurements.

Deviations between the one–temperature model for dilute gases by Kustova et al. [51] and LITA measurements in Fig. 6.5 could also occur due to the limited validity of the applied model. Note that the model by Kustova et al. [51] estimates the volume viscosity based on the deviation of the vibrational and rotational relaxation from its equilibrium state. Hence, it does not take additional acoustic losses due to an excitation of vibrational and/or rotational degrees of freedom into account. The latter are caused by the frequency of the induced acoustic wave ν_a, which is in a similar range as the vibrational relaxation times for the investigated temperatures shown in Fig. 2.6. As discussed in the previous chapter, another possible explanation for the models discrepancy lies in the pressure dependency of the internal relaxation time. The latter is, as discussed by Shields [94], approximately reciprocally dependent on pressure, which leads to a nearly pressure independent volume viscosity framework for dilute gases. A coupled model extension for dense gases would consider the dependency of dense gas effects, such as elastic collisions, on internal relaxation mechanisms and vice versa. The latter influences the dependency on pressure and could therefore lead to a better agreement between model and measurement results. In addition to the theoretical model by Kustova et al. [51] the LITA extracted values can be compared to the dilute gas model by Cramer [17] as well as to molecular simulations by Jaeger et al. [46], see Fig 2.9. Cramer [17] estimates a viscosity ratio of $\mu_v/\mu_s = 3957$ independent from pressure for a temperature of 300 K, whereas Jaeger et al. [46] predict values of approximately $\mu_v/\mu_s = 2200$ for densities above $\varrho > 66\,\mathrm{kg\,m^{-3}}$ at a temperature of 300 K. Note that since the dilute gas or kinetic model applied by Jaeger et al. [46] is based on the theoretical framework by Cramer [17] both models provide similar results. Hence, despite of the observed deviations the framework by Kustova et al. [51] provides the best agreement with the experimental data.

6.1.3 Outcome of the principal investigations in carbon dioxide

In conclusion, the importance of obtaining transport properties, such as the acoustic damping rate, at high pressure and temperature conditions is twofold. First, investigations in pure fluids in the vicinity of the critical point enable the assessment of the significance of volume viscosities at nearcritical fluid states. Moreover, as stated in section 2.2, with suitable models for speed of sound and acoustic damping rates, mixing states can be determined according to equation (2.13). However, modelling of acoustic damping rates is challenging due to the high pressure/density conditions, the necessary consideration of volume viscosities in complex fluids, and additional acoustic losses due to acoustic excitation of vibrational and/or rotational degrees of freedom in complex fluids. The latter is associated with a dependency of the acoustic absorption coefficient per wavelength α_λ on the acoustic frequency–pressure ratio. The above challenges are revealed by the LITA measurements in carbon dioxide. The peak in the attenuation spectrum is hereby located at a lower frequency–pressure ratio, out of scope of the herein investigated conditions. The LITA results are located at the right side of the bell–shaped attenuation spectrum of α_λ, see Fig. 6.3. Furthermore, at nearcritical conditions ($p_r = 0.81$, $T_r = 0.98$) a sharp increase in the acoustic absorption coefficient is observed. The latter is likely related to an increase in volume viscosity, which experiences a singularity in the critical point. Eventhough the deviation between the theoretical framework by Kustova et al. [51] and the LITA results are high, the model by Kustova et al. [51] shows the best agreement compared to the theoretical predictions by Cramer [17] and the simulations conducted by Jaeger et al. [46]. Two possible explanations for these discrepancies are given. First, the dilute gas model by Kustova et al. [51] is derived and validated for low pressure conditions up to 0.1 MPa and therefore does not account for dense gas effects. Second, the one–temperature approach chosen by Kustova et al. [51] to model the volume viscosity does not take additional losses due to acoustic excitation into account. Nevertheless the experimental and theoretical values presented in Fig. 6.5 clearly indicate the importance of the volume viscosity in carbon dioxide. Especially at near- to supercritical conditions the consideration of volume viscosities becomes vital for reliable numerical simulations as well as theoretical predictions. To study supercritical fluid phenomena and Widom–line transitions from liquid–like to gas–like states, further experiments in pure fluids in compressible liquid, liquid–like, and gas–like states are envisaged. A new pressure chamber with a copper based sealing concept has been design to facilitate the planned investigations.

6.2 Measurements in gaseous mixing processes

The research objective of the investigation on gaseous jet mixing is twofold. First, measurements are conducted to further characterise the size of the LITA probe volume of the high–speed LITA setup. This is done with the aim of analysing its effect on speed of sound investigations and detected mixture states. Note that the conservative, visual assessment in section 3.2.3, which takes the grating illumination by the interrogation beam into account, leads to a measurement volume with an ellipsoid shape approximately 4 mm in length, 246 µm in width and 80 µm in height. Second, based on the estimation of nitrogen mole fractions at various positions of the mixing jet, dependencies of extracted acoustic damping rates on the mixture composition are studied. The jet mixing studies are conducted in an argon jet released into a nitrogen atmosphere with a pressure of 4 MPa and a temperature of approximately 300 K. The jet is hereby generated using the expansion module presented in section 3.1.3. Visualisation of the mixing process is realised by the schlieren setup shown in Fig 3.14, while LITA is performed with the high–speed LITA setup. The BE is hereby adjusted for a small optical interference pattern and the signal beam is monitored by a SM fibre. Since the measurements are performed at room temperature without additional heating, isothermal mixing conditions are assumed. Note that the LITA measurement volume is placed approximately 1.4 mm downstream of the nozzle.

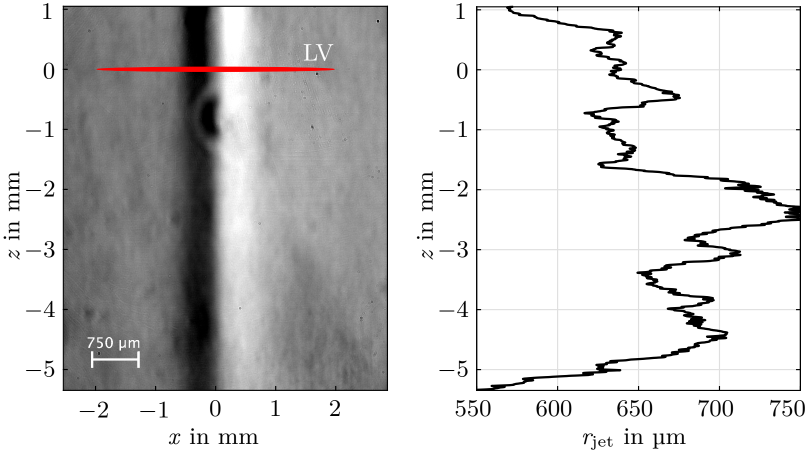

(a) Enhanced schlieren image.

(b) Jet radius over z–coordinate.

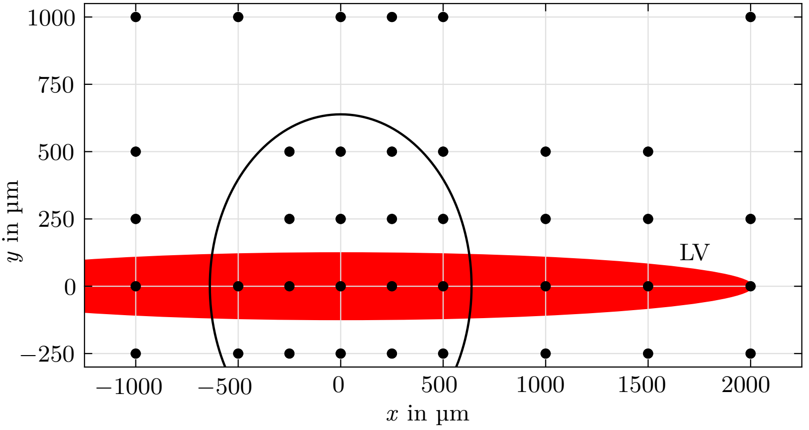

(c) LITA measurement positions in x and y–direction (dots). Outer jet contour at $z = 0\,\mathrm{mm}$ is indicated as a black line. The LITA measurement volume is exemplarily placed for $x = y = z = 0\,\mathrm{mm}$ in red. Note that due to scaling the jet is elongated in y–direction.

Figure 6.6: Characterisation and visualisation of the investigated gaseous jet mixing process. Position and size of the LITA measurement volume is indicated in red. Jet fluid: argon; atmospheric fluid: nitrogen; pressure: $p_{\mathrm{ch}} = 4\,\mathrm{MPa}$; temperature: $T_{\mathrm{ch}} = T_{\mathrm{jet}} \approx 300\,\mathrm{K}$; LV: LITA measurement volume.

A visualisation of the investigated argon jet is presented in form of a contrast enhanced schlieren image together with the contour based estimation of the jet radius in Fig. 6.6. Note that the deviation of the jet radius at $z = 2.5\,\mathrm{mm}$ in Fig. 6.6b results from the blurred right jet contour at this position and is most likely an error in measurement. The position and size of the LITA measurement volume located at the jets centre is hereby displayed in red. Its size, which takes the grating illumination by the interrogation beam into account, is based on the tomographic assessment in section 3.2.3. Investigations are performed at $z = 0\,\mathrm{mm}$, while x, y coordinates are explored by moving the chamber together with the schlieren setup, relative to the fixed LITA measurement volume. The jet radius at this position is $r_{z=0,\mathrm{jet}} = 639 \pm 14\,\mu\mathrm{m}$. The location of the LITA measurements in the x–y–plane are shown in Fig. 6.6c. The outer jet contour estimated based on the schlieren imaging is presented as a black line. Note that for clarity the axes are scaled differently resulting in a ellipsoid shape of the jet in Fig. 6.6c.

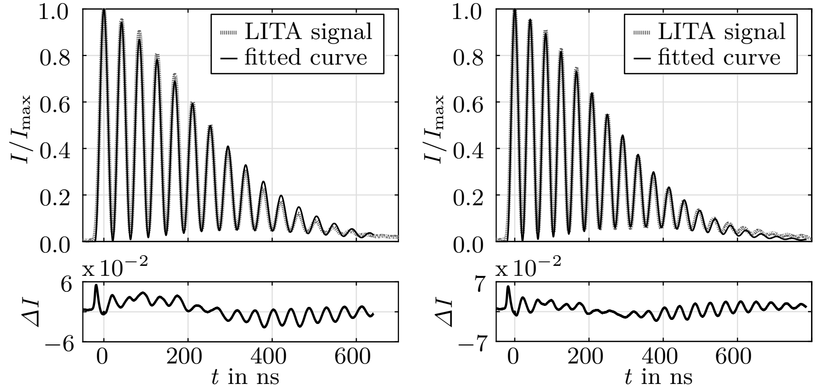

(a) $x = 0\,\mu\mathrm{m}$; $y = 0\,\mu\mathrm{m}$.

(b) $x = 2000\,\mu\mathrm{m}$; $y = 0\,\mu\mathrm{m}$.

Figure 6.7: Curve fitting results and measured LITA signals at two different x–positions in an argon jet mixing in a nitrogen atmosphere. Fitting results are used to estimate speed of sound c_s and acoustic damping rate Γ. Operating conditions, input parameters, and results are listed in Tab. 6.2.

Two recorded signals, detected at different positions, are presented together with their curve fits in Fig. 6.7. The operating conditions, input parameters, and results are listed in Tab. 6.2.

Table 6.2: Overview of operating conditions, input parameters, and curve fitting results for gaseous jet mixing investigations shown in Fig. 6.7. Uncertainties are listed using a 68% confidence interval.

		operating conditions			input parameters	
x in µm	y in µm	p_{ch} in MPa	T_{ch} in K	o	ω_{cal} in µm	Λ_{cal} in µm
0	0	4 ± 0.05	298 ± 0.6	2079	134 ± 40	29.43 ± 0.14
2000	0	4 ± 0.05	300 ± 0.7	1930	134 ± 40	29.43 ± 0.14

		input parameters		curve fitting results	
x in µm	y in µm	σ_{th} in µm	model	$c_{s,\mathrm{LITA}}$ in $\mathrm{m\,s^{-1}}$	Γ_{LITA} in $\mathrm{mm^2\,s^{-1}}$
0	0	151 ± 16	small detector limit	349 ± 2	9.56 ± 5.9
2000	0	151 ± 16	small detector limit	354 ± 1	6.25 ± 5.3

All signals show a non–resonant fluid behaviour. Note that measurements in the centre of the jet exhibit a lower speed of sound compared to the results in the jets far field at $x = 2000\,\mathrm{µm}$. Additionally, the acoustic damping rate in the jets centre is higher as the values detected in the far field. Both resulting from the jet mixing process leading to lower argon concentrations in the far field compared to the jet centre. In case of the speed of sound this is a result of the difference in speed of sound at operating conditions of argon $c_{s,\mathrm{NIST,Ar}} = 327\,\mathrm{m\,s^{-1}}$ compared to nitrogen $c_{s,\mathrm{NIST,N_2}} = 361\,\mathrm{m\,s^{-1}}$, values are taken from the NIST database by Lemmon et al. [56].

6.2.1 Speed of sound and concentration profile for gaseous jet mixing at high pressures

The speed of sound data for all measurement points presented in Fig. 6.6 are computed from recorded LITA signals using the frequency analysis presented in section 4.2. The grid spacing Λ is calibrated using measurements in pure nitrogen and argon prior to the jet investigations. Note that due to beam steering effects resulting from the jet mixing process, signals with non–physical beat frequencies are possible. Especially, measurements in front of the jet ($x < 0$) are challenging, since the scattered light of the signal beam passes through the jet. To ensure physically correct results, an additional signal filtering following the methodology presented in section 4.2.3 is performed. For this purpose, measurements with speed of sound data higher as the value of nitrogen are excluded from the results. The latter would lead to nitrogen mole fractions greater than one.

Based on the speed of sound data the nitrogen mole fractions $X_{\mathrm{N_2}}$ are calculated assuming ideal gas behaviour and an isothermal mixing process. The latter can be applied, since measurements are conducted at room temperature without additional heating. The ideal gas framework has been applied, since calculations with the implemented mixture model of the NIST database by Lemmon et al. [56] are not possible. However, the error made by the ideal gas assumption lies within the 68% confidence interval of the LITA measurements and the operating temperature of approximately 300 K is much higher as the critical values of argon ($T_{c,\mathrm{Ar}} = 151\,\mathrm{K}$) and nitrogen ($T_{c,\mathrm{N_2}} = 126\,\mathrm{K}$), values are taken from the NIST database by Lemmon et al. [56]. Consequently, the ideal gas framework is applicable. The nitrogen mole fraction $X_{\mathrm{N_2}}$ of the mixture is therefore computed by the set of equations presented in equation (6.1), referred by Stephan et al. [109]. The detected speed of sound $c_{s,\mathrm{LITA}}$, the molar masses of argon M_{Ar}, nitrogen $M_{\mathrm{N_2}}$, and the temperature of the mixing process T_{mix} are hereby input parameters. Note that the mixing temperature is approximated by $T_{\mathrm{mix}} = T_{\mathrm{ch}}$.

$$
\begin{aligned}
X_{\mathrm{N_2}} &= 1 - X_{\mathrm{Ar}} \\
Y_{\mathrm{Ar}} &= 1 - Y_{\mathrm{N_2}} \\
Y_{\mathrm{N_2}} &= \frac{M_{\mathrm{N_2}}}{M_{\mathrm{mix}}}\, X_{\mathrm{N_2}} \\
M_{\mathrm{mix}} &= X_{\mathrm{N_2}}\, M_{\mathrm{N_2}} + X_{\mathrm{Ar}}\, M_{\mathrm{Ar}} \\
c_{p,\mathrm{mix}} &= Y_{\mathrm{N_2}}\, c_{p,\mathrm{N_2}} + Y_{\mathrm{Ar}}\, c_{p,\mathrm{Ar}} \\
c_{v,\mathrm{mix}} &= Y_{\mathrm{N_2}}\, c_{v,\mathrm{N_2}} + Y_{\mathrm{Ar}}\, c_{v,\mathrm{Ar}} \\
R_{\mathrm{mix}} &= Y_{\mathrm{N_2}}\, R_{\mathrm{N_2}} + Y_{\mathrm{Ar}}\, R_{\mathrm{Ar}} \\
c_{s,\mathrm{LITA}} &= \sqrt{\frac{R_{\mathrm{mix}}\, T_{\mathrm{mix}}\, c_{p,\mathrm{mix}}}{c_{v,\mathrm{mix}}}}
\end{aligned}
\tag{6.1}
$$

The mass fraction in equation (6.1) is denoted with Y, while the mole fraction is X, the specific isobaric heat capacity is c_p, the specific isochoric heat capacity is c_v and the specific gas constant is R. The local state of the mixture is hereby indicated with the subscript $_{\mathrm{mix}}$, the fluid argon with $_{\mathrm{Ar}}$, and nitrogen with $_{\mathrm{N_2}}$.

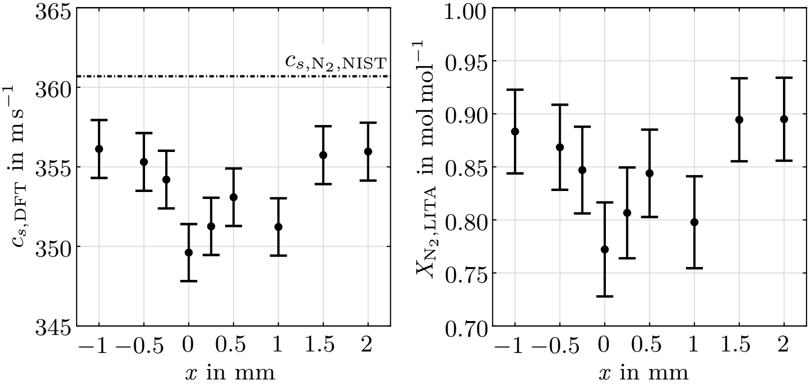

(a) c_s over x. (b) $X_{\mathrm{N_2}}$ over x.

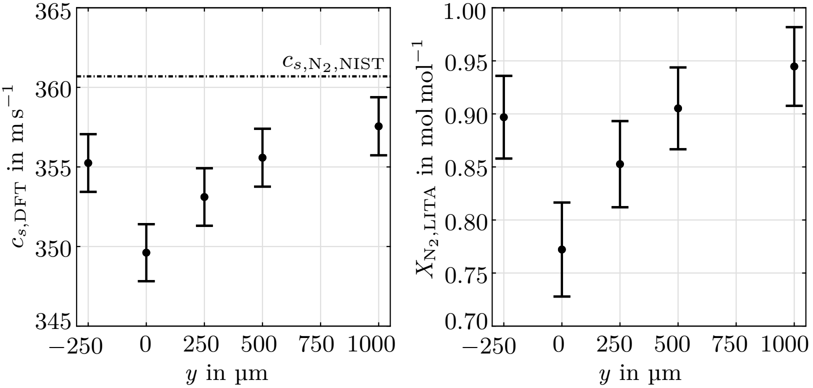

(c) c_s over y. (d) $X_{\mathrm{N_2}}$ over y.

Figure 6.8: Speed of sound $c_{s,\mathrm{DFT}}$ and nitrogen mole fraction $X_{\mathrm{N_2},\mathrm{LITA}}$ detected at various x and y–positions at $z = 0\,\mathrm{mm}$. For profiles in x-direction $y = 0\,\mathrm{\mu m}$, while for profiles in y-direction $x = 0\,\mathrm{\mu m}$. Speed of sound data are calculated using the frequency analysis presented in section 4.2. Nitrogen mole fractions are calculated with equation (6.1). Uncertainties are displayed using a 68% confidence interval. Thermodynamic data are taken from Lemmon et al. [56]. Jet fluid: argon; atmospheric fluid: nitrogen; pressure: $p_{\mathrm{ch}} = 4\,\mathrm{MPa}$; temperature: $T_{\mathrm{ch}} = T_{\mathrm{jet}} \approx 300\,\mathrm{K}$.

Figure 6.8a depicts the speed of sound and Fig. 6.8b the concentration profile detected at various x–positions with $y = 0\,\mu\text{m}$ and $z = 0\,\text{mm}$, while in Fig. 6.8c and Fig. 6.8d the profiles in y-direction with $x = 0\,\mu\text{m}$ and $z = 0\,\text{mm}$ are displayed. The theoretical speed of sound of nitrogen at the operating conditions taken from the NIST database by Lemmon et al. [56] is displayed as a dash-dotted line, while measurement uncertainties are presented using a 68% confidence interval.

Unfortunately, the speed of sound measurement at $x = 1\,\text{mm}$ presents itself as a weak outlier. The reason for the slight deviation lies in beam steering effects resulting from the argon jet. Additionally, measurements taken in front of the jets centre $x < 0$ display higher speed of sound values as behind the jet. A similar behaviour is observed for negative points in y. The author hypothesises that these deviations from rotational symmetry results from a slight misalignment between the jet and the LITA probe volume or come from a non–rotationally symmetric jet. Note that in the far field of the x–axis profile a N_2 mole fraction of $X_{N_2,\text{LITA}} = 0.89 \pm 0.05$ is estimated, whereas the far field in y–direction yields a mole fraction of $X_{N_2,\text{LITA}} = 0.94 \pm 0.05$. In the centre of the jet the mole fraction is $X_{N_2,\text{LITA}} = 0.77 \pm 0.05$.

LITA measurements are a weighted average of processes and fluids within its measurement volume. The visual characterisation in section 3.2.3 suggests a length of the ellipsoid probe volume in x–direction of 4 mm and a width in y–direction of 246 µm. Nevertheless, the concentration profiles in x–direction, shown in Fig. 6.8b, reveal a shape similar to the results in y–direction depicted in Fig. 6.8d. Both profiles agree qualitatively with each other as well as with the jet geometry. To further assess the influence of the weighted average of the probe volume on the speed of sound estimations, the far field concentrations in the x–axis and in the y–axis are compared. The latter is hereby the benchmark, since no interaction with the jet is possible. Indeed the mole fraction at ($x = 0\,\text{mm}$; $y = 1000\,\mu\text{m}$) is with $X_{N_2,\text{LITA}} = 0.94 \pm 0.05$ slightly higher as the result of $X_{N_2,\text{LITA}} = 0.89 \pm 0.05$ at ($x = 2\,\text{mm}$; $y = 0\,\mu\text{m}$). However, considering the uncertainties both measurements agree with each other in the scope of their confidence interval. Hence, the influence of the length of the probe volume on the extracted speed of sound data is small compared to the measurement uncertainty. In virtue of this fact, the effective size of the probe volume is smaller as the visual assessment suggests. Based on the radial speed of sound profiles presented by Baab et al. [6], their discussion in section 3.2.1, and the previous argumentation of the concentration profiles the author suggest an effective length smaller than the jet diameter of $d_\text{jet} = 1.3\,\text{mm}$. Hence the effective measurement volume of the high–speed LITA setup is an ellipsoid smaller than 1.3 mm in length, 246 µm in width and 80 µm in height.

6.2.2 Acoustic damping rates in gaseous jet mixing processes

Based on the curve fitting methodology presented in section 4.3 acoustic damping rates are computed from the time–domain of the recorded signals. The necessary Gaussian half–width of the excitation beam is calibrated using measurements in argon conducted prior to the jet investigations. In Fig. 6.9 the extracted acoustic damping rates Γ_{LITA} are displayed over their respective nitrogen mole fractions presented in the previous section. The acoustic damping rate detected prior to the jet investigation in pure nitrogen at operating conditions is additionally indicated (dash-dotted line). The measurement uncertainty is shown using a 68% confidence interval.

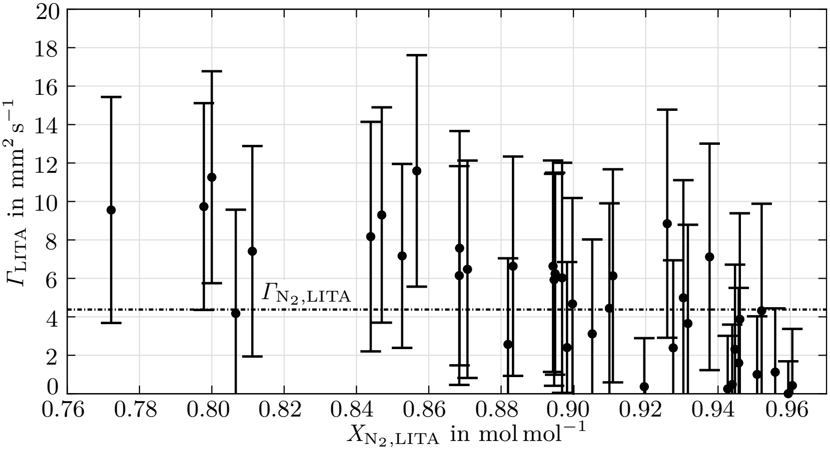

Figure 6.9: Extracted acoustic damping rate Γ_{LITA} over mole fractions of nitrogen $X_{\mathrm{N_2,LITA}}$. Acoustic damping rate is computed using the SDL model. Nitrogen mole fraction is calculated with equation (6.1). Uncertainties are displayed using a 68% confidence interval. Necessary thermodynamic data are taken from Lemmon et al. [56]. Jet fluid: argon; atmospheric fluid: nitrogen; pressure: $p_{\mathrm{ch}} = 4\,\mathrm{MPa}$; temperature: $T_{\mathrm{ch}} = T_{\mathrm{jet}} \approx 300\,\mathrm{K}$.

The acoustic damping rates show a counter–intuitive dependency on the nitrogen mole fraction. While the acoustic damping rate for argon at operating conditions is with $\Gamma_{\mathrm{Ar,NIST}} = 0.44\,\mathrm{mm^2\,s^{-1}}$ lower as for nitrogen with $\Gamma_{\mathrm{N_2,LITA}} = 4.38\,\mathrm{mm^2\,s^{-1}}$, the detected damping rates Γ_{LITA} increase with decreasing nitrogen mole fraction. This dependency is a result of acoustic absorption arising from the diffusion between the species. This effect has previously been observed for binary mixtures of atomic species by Li et al. [58], who have suggested to model the acoustic damping rate for mixtures $\mathit{\Gamma}_{\text{mix}}$ of atomic species according to

$$\mathit{\Gamma}_{\text{mix}} = \Gamma_{c,\text{mix}} + \Gamma_{\text{diff}} \ . \tag{6.2}$$

The classic acoustic damping rate of the mixture $\Gamma_{c,\text{mix}}$ is hereby defined by equation (2.15) using thermodynamic properties of the mixture state. The additional acoustic absorption due to diffusion is considered by Γ_{diff}. Since the model by Li et al. [58] neglects the influence of volume viscosities, it is only valid for atomic species and therefore not applicable in the presented jet measurements. Nevertheless, the contribution of the diffusion related acoustic absorption is clearly visible in the data shown in Fig. 6.9 and has to be considered in a mixture model for non–atomic species.

6.2.3 Outcome of the gaseous jet mixing investigations

In conclusion, investigations in argon jets injected into nitrogen atmosphere reveal two important insights. Based on the profile measurements conducted inside and in the far field of the jet mixing process, an extended characterisation of the size of the LITA measurement volume is possible. Since only a small influence of the length of the probe volume is observed in the speed of sound and concentration profiles, an effective length of the probe volume is determined. This results in an ellipsoid shaped measurement volume with an effective length of 1.3 mm, while width and height remain unchanged. Additionally, extracted acoustic damping rates at different mole fractions reveal the importance of the additional diffusion related acoustic absorption term in mixtures. The latter has been observed by Li et al. [58] in binary mixtures of atomic species. Hence, a model for the acoustic damping rate in mixtures of complex fluids at high pressure condition has to consider both, the volume viscosity and the acoustic absorption due to diffusion between species. Unfortunately, reliable models for complex fluids and fluid mixtures at high pressure conditions are sparse.

6.3 Transient studies in nearcritical evaporation processes

The primary objective of the time–resolved studies in a nearcritical evaporation process is to present the feasibility of time–resolved measurements using laser–induced thermal acoustics under complex flow conditions. Specifically, in this work, the application of high–speed LITA in the wake of an evaporating droplet is demonstrated. To the authors knowledge, this is the first–time that transient LITA measurements investigating macroscopic fluid phenomena are conducted. Secondary to the proof of feasibility is the investigation of an evaporation process in the vicinity of the critical point. The objective is to quantify mixture states, such as temperature, concentration and speed of sound, in the wake of a free falling droplet. These results can be used for validation of numerical codes, such as FS3D, applied in evaporation research. Note that, eventhough curve fitting of the recorded LITA signals is possible, an extraction of acoustic damping rates has not been feasible for the performed investigations. This is an unfortunate result due to staining of the quartz windows during the measurements, which as previously discussed influences the Gaussian half–width of the excitation and interrogation beam. The staining is a result from small satellite drops detaching from the capillary after the main droplet, which enter the LITA measurement volume. Unfortunate timing of the excitation laser pulse can then cause the satellite drops to explode, contaminating the inside surface of the quartz windows.

Transient investigations are conducted in the wake of a free falling acetone droplet in a nitrogen atmosphere with a pressure of $6 \pm 0.5\,\mathrm{MPa}$ and a temperature of $513 \pm 7.4\,\mathrm{K}$. Note that the uncertainty in temperature takes the distribution inside the chamber, as discussed in section 3.1.1, into account. In close proximity to the LITA measurement volume an uncertainty of $\pm 1\,\mathrm{K}$ is more accurate. Droplet generation and detachment is realised by the droplet generator presented in section 3.1.2. The detachment frequency is hereby set to $1\,\mathrm{Hz}$. Prior to droplet generation the liquid is preheated to a temperature of $T_{\mathrm{d}} = 453 \pm 1\,\mathrm{K}$. Regarding the critical values of acetone taken from the NIST database by Lemmon et al. [56] ($T_c = 508.1\,\mathrm{K}$, $p_c = 4.7\,\mathrm{MPa}$) this leads to the reduced conditions of $T_{r,\mathrm{d}} = 0.89$, $T_{r,\mathrm{N_2}} = 1.01$, and $p_{r,\mathrm{ch}} = 1.28$. These operating conditions and the droplet detachment frequency are selected for comparison with Raman scattering and LIFP investigations presented by Preusche [82]. The evaporation process is visualised by the shadowgraphy arrangement presented in Fig. 3.13. The setup for triggering the droplet detachment, excitation laser, light source, and high–speed camera is explained in section 3.3.1. Please note that preliminary results of these transient investigations have been published in form of a feasibility study by Steinhausen et al. [108].

In Fig. 6.10 shadowgrams of the evaporating free falling acetone droplet at eight different time steps are depicted. The time stamp on the left upper corner is hereby the time, synchronised with the LITA measurements, while size and position of the LITA measurement volume is presented in red. Unfortunately, the optical resolution of the shadowgraphy setup is not sufficient to detect changes in droplet diameter resulting from evaporation. This leads to an almost constant equivalent diameter of approximately 1.4 mm. This observation is consistent with experimental studies by Weckenmann et al. [115] under similar conditions.

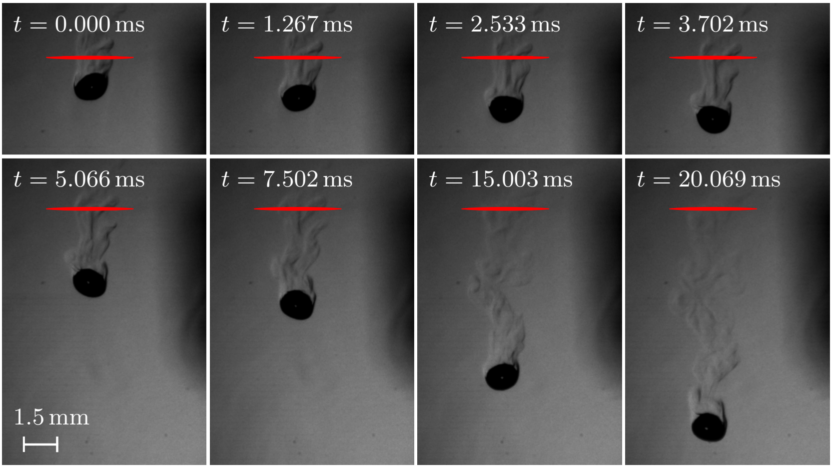

Figure 6.10: Shadowgrams of eight time steps of a free-falling acetone droplet evaporating in a nitrogen atmosphere. LITA measurement volume is indicated in red. The time stamp on the left upper corner is synchronised with the LITA measurements. Droplet radius: $r_\mathrm{d} = 0.7$ mm; reduced operating conditions: $T_{r,\mathrm{d}} = 0.89$; $T_{r,\mathrm{ch}} = 1.01$; $p_{r,\mathrm{ch}} = 1.28$.

The ligaments in the wake of the droplet as well as different shades of grey indicate a strong evaporation process. As previously discussed by Steinhausen et al. [104] and Lamanna et al. [53], the dark ligaments indicate the presence of a dense gaseous fluid region in the direct vicinity of the droplet, while the droplets core remains in the liquid state. The latter results from strong evaporative cooling, preventing the droplet from gasification by mitigating the heating of the droplet. At the LITA measurement position, the fluids experience strong changes in density gradients that weaken over time and distance to the evaporating droplet. After $t = 7.5\,\mathrm{ms}$, the shadowgrams indicate a similar behaviour over time at the probe volume of the LITA setup.

Time–resolved LITA measurements are performed with the high–speed LITA setup. The BE is adjusted for a small optical interference pattern, while the signal beam is monitored by a SM fibre. Note that this setup is equal to the one used in the jet mixing studies. The transient measurements are realised by detecting a signal, 100 ms in length, comprised of 1000 time–resolved LITA signals. The latter are distinguished using the data of the photo diode D2 in Fig 3.8, which is monitored and stored in addition to the LITA signal using a second time synchronised channel on the DAQ. Averaging of the LITA measurements is performed for each recorded time step using 40 independent droplet evaporation processes. Note that the number of recorded samples is limited due to the processing and saving time of both, the oscilloscope and the high–speed camera. Moreover, due to strong beam steering effects in the droplets wake less than 10 % of the recorded signals are valid.

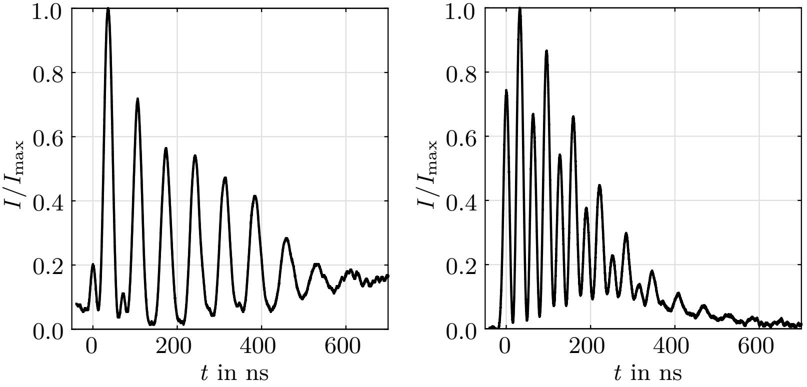

(a) $t = 0.974\,\mathrm{ms}$; Single shot signal.

(b) $t = 9.840\,\mathrm{ms}$; Signal is averaged over 4 single shot signals.

Figure 6.11: LITA signals obtained at two time steps in the wake of an acetone droplet evaporating in a nitrogen atmosphere. Signals are detected with the high–speed LITA setup by a SM fibres. Reduced operating conditions: $T_{r,\mathrm{d}} = 0.89$; $T_{r,\mathrm{ch}} = 1.01$; $p_{r,\mathrm{ch}} = 1.28$.

Two LITA signals detected at different time steps in the wake of the evaporating acetone droplet are exemplarily depicted in Fig. 6.11. The resonant fluid response shown by both signals is likely a result of residual moisture in the acetone supply line. As previously discussed for carbon dioxide in section 5.2.1, traces of solute water in acetone lead to a resonant fluid behaviour. Note that for earlier time steps beam steering effects and a stronger contribution of the thermal grating is observed. The latter is indicated by the dominating oscillating frequency of the signal in Fig. 6.11a compared to Fig. 6.11b. At early time steps the signal oscillates at the Brillouin frequency, while over time an oscillation with twice the Brillouin frequency. Both the beam steering and the thermal grating contribution are caused by a higher concentration of the droplet fluid in direct vicinity of the droplet.

6.3.1 Temporal evolution of speed of sound data in the droplets wake

Time–resolved speed of sound data are computed from the detected LITA signals using the frequency analysis presented in section 4.2. The grid spacing Λ is hereby calibrated with signals recorded in nitrogen at operating conditions prior to the droplet investigations. As for the jet investigation, one extra step is added to the filter methodology to exclude outliers due to beam steering effects. For this purpose, speed of sound data higher as the value of nitrogen at operating conditions are excluded from the results.

The temporal evolution of speed of sound in the droplets wake is shown in Fig. 6.12. The speed of sound for nitrogen is presented as a dash–dotted line, while measurement uncertainties are displayed using a 68% confidence interval. The speed of sound data support the observation made from the shadowgrams in Fig. 6.10 of stronger changes in density gradients at earlier time steps within the LITA measurement volume. At early time steps, the extracted speed of sound presents with significantly lower values as the speed of sound of nitrogen at operating conditions. The speed of sound then rises asymptotically with time until at approximately $t = 7.5\,\text{ms}$ a constant value slightly below the speed of sound of nitrogen is reached. This asymptotic behaviour in speed of sound is consistent with the shadowgraphy observations, which suggest a similar mixing process at time steps above 7.5 ms. The explanation for the temporal shape of the speed of sound measurements is twofold. First, speed of sound data depend on the concentration of the binary gaseous acetone–nitrogen mixture. Predictions with the NIST database by Lemmon et al. [56] for rising acetone mole fractions show a decreasing speed of sound for an increasing acetone concentration in the droplets wake. Second, since the speed of sound is proportional to the square root of the temperature, a lower temperature in the wake results in lower speed of sound values in vicinity of the droplet. The

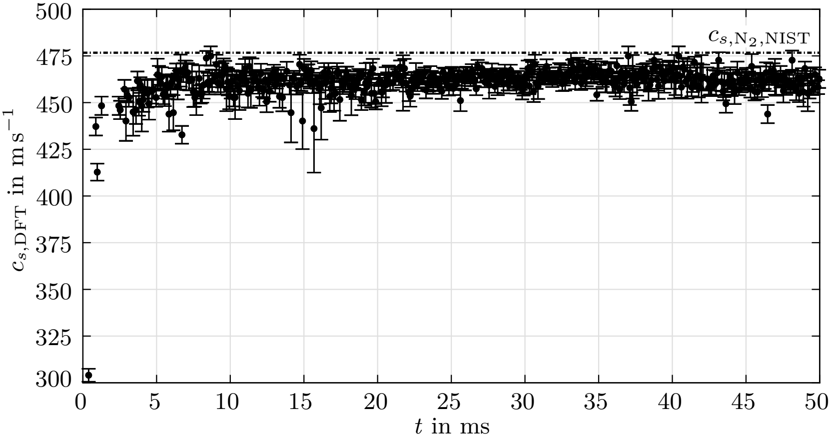

Figure 6.12: Transient speed of sound data in the wake of an evaporating acetone droplet in a nitrogen atmosphere. Speed of sound data are calculated using the frequency analysis presented in section 4.2. Uncertainties are displayed using a 68% confidence interval. Reduced operating conditions: $T_{r,\mathrm{d}} = 0.89$; $T_{r,\mathrm{ch}} = 1.01$; $p_{r,\mathrm{ch}} = 1.28$.

decrease in temperature results from evaporative cooling of the droplet. The temperature and concentration field in the droplet wake previously studied by Bork et al. [14] and Preusche et al. [81] support these observations.

6.3.2 Temporal evolution of the mixture state in the droplets wake

For non–isothermal processes, such as droplet evaporation, mixing temperature and concentration are not directly given by the speed of sound. This is because the latter depends on both temperature and concentration. Since an extraction of acoustic damping rates has not been possible and a reliable model for the acoustic damping rate for a nitrogen–acetone mixture is not available, an additional relation for temperature and mole fraction is necessary to compute mixing states based on the extracted speed of sound data. As previously discussed in section 2.3.1, as well as presented by Lamanna et al. [53] and Preusche et al. [81], the advection–governed mixing process in the wake of an evaporating droplet supports the application of an adiabatic mixing assumption within a small measurement volume. This adiabatic mixing framework inherently assumes a conservation of mass and energy within the probe volume for the duration of the laser pulse. The latter can be supported based on the length of the laser pulse ($\tau = 8.8\,\mathrm{ns}$) and the effective measurement volume ($0.1\,\mathrm{mm}^3$) of the high–speed LITA setup.

In case of the speed of sound measurement presented in Fig. 6.12 the adiabatic mixing assumption is applied to estimate mixture states. The latter is based on the Raman–scattering investigation for the evaporation of an acetone droplet under similar conditions presented by Preusche [82]. Raman scattering is hereby used to estimate the number density and the acetone mole fraction in the droplets wake. Based on these experimental findings the temperature–concentration relation is obtained by processing the data with the PC–SAFT EoS, referred by Gross and Sadowski [36], while assuming adiabatic mixing. Here, the local mole fraction as well as the local mixing temperature within the LITA measurement volume are estimated using the LITA extracted speed of sound data together with the PC–SAFT–based fit of the Raman scattering results presented in Fig. 2.12.

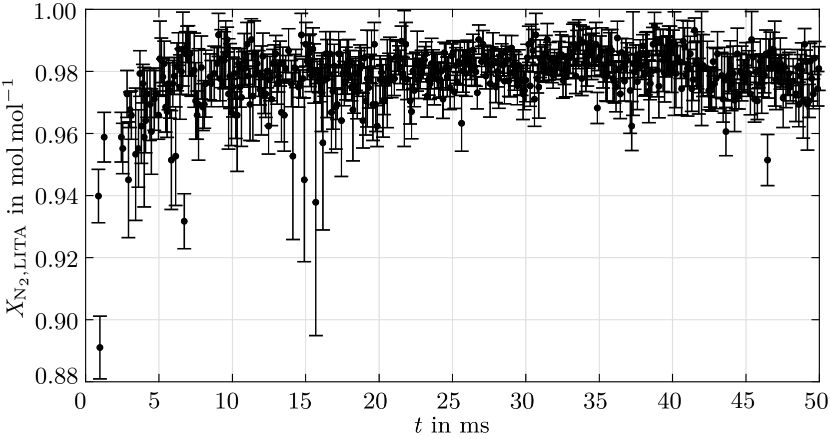

Figure 6.13: Local mole fraction of nitrogen $X_{\mathrm{N_2}}$ over time estimated in the wake of an evaporating acetone droplet in a nitrogen atmosphere. $X_{\mathrm{N_2}}$ is estimated using $c_{s,\mathrm{DFT}}$ assuming adiabatic mixing together with the PC–SAFT–based curve fit of Raman scattering results in Fig. 2.12. Uncertainties are shown with a 68% confidence interval. Reduced operating conditions: $T_{r,\mathrm{d}} = 0.89$; $T_{r,\mathrm{ch}} = 1.01$; $p_{r,\mathrm{ch}} = 1.28$.

The temporal evolution of the local mole fraction of nitrogen $X_{\mathrm{N_2,LITA}}$ over time t estimated in the wake of the acetone droplet is shown in Fig. 6.13. Measurement uncertainties are presented with a 68% confidence interval. As expected, the temporal evolution of the nitrogen mole fraction displays a similar shape as the speed of sound results. At early time steps the acetone concentration is high. However, even for the first valid time step, the acetone mole fraction does not exceed 11 %. The asymptote of the nitrogen mole fraction is with approximately 0.985 slightly lower as the far field concentration of $X_{\mathrm{N}_2} = 0.9949$ observed by Preusche [82]. This discrepancy results from differences in measurement technique and location. LITA measurements are taken in the axis of the droplet, whereas the far field concentration is computed based on planar two dimensional Raman scattering results with regions unaffected by the wake.

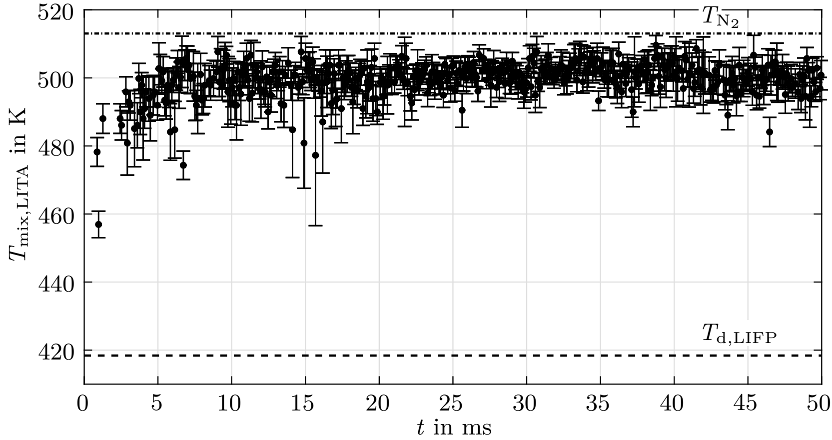

Figure 6.14: Local mixing temperature T_{mix} over time estimated in the wake of an evaporating acetone droplet in a nitrogen atmosphere. T_{mix} is estimated using $c_{s,\mathrm{DFT}}$ assuming adiabatic mixing together with the PC–SAFT–based curve fit Raman scattering results in Fig. 2.12. Uncertainties are shown with a 68% confidence interval. Reduced operating conditions: $T_{r,\mathrm{d}} = 0.89$; $T_{r,\mathrm{ch}} = 1.01$; $p_{r,\mathrm{ch}} = 1.28$.

Figure 6.14 depicts the local temperature of the mixture T_{mix} over time t estimated within the LITA probe volume. The temperature of the nitrogen atmosphere T_{N_2} is shown by the dash-dotted line, while the droplet temperature measured with LIFP $T_{\mathrm{d,LIFP}}$ by Preusche [82] at similar operating conditions is presented with a dashed line. As before, measurement uncertainties are displayed with a 68% confidence interval. The temporal evolution shows a sharp decrease in local mixing temperature in close vicinity to the droplet, which rises with time until at $t = 7.5\,\mathrm{ms}$ a constant temperature of 500 K is reached.

To determine the thermodynamic state of the mixing process in the droplets wake, it is important to emphasise that the critical conditions of the mixture are between $T_{c,\mathrm{mix}} = 168\,\mathrm{K}$, $p_{c,\mathrm{mix}} = 10\,\mathrm{MPa}$ at $X_{\mathrm{N}_2} = 0.89$ ($t = 0.974\,\mathrm{ms}$) and $T_{c,\mathrm{mix}} = 134\,\mathrm{K}$, $p_{c,\mathrm{mix}} = 4.8\,\mathrm{MPa}$ for $X_{\mathrm{N}_2} = 0.98$ ($t > 7.5\,\mathrm{ms}$), data are taken from the NIST database by Lemmon et al. [56]. Hence, with respect to the critical point of the mixture, the mixing process in the droplets wake is subcritical and superheated at early time steps and becomes supercritical over time due to the decrease in critical mixing pressure.

Based on the theoretical prediction with the evaporation model by Young [119] shown in Fig. 2.14 as well as the LIFP measurements by Preusche [82], presented in section 2.3, the evaporation process remains subcritical. Hence, at earlier time steps with measurements close to the droplet, both evaporation and the subsequent mixing process of acetone vapour in the wake remain subcritical, eventhough the droplet is injected and evaporating in a supercritical atmosphere with respect to the injected fluid. At later time steps and probe positions further away from the droplet, the mixing process becomes supercritical with respect to the mixtures critical point.

6.3.3 Outcome of time–resolved investigations

In conclusion, the time–resolved investigations in the wake of an evaporating acetone droplet in a nitrogen atmosphere present two main outcomes. First and foremost, the results proof the feasibility of transient laser–induced thermal acoustic measurements in macroscopic fluid phenomena. To the authors knowledge, this has been the first time that time–resolved LITA studies investigating complex fluid phenomena have been conducted. Second, the speed of sound investigations together with the presented adiabatic mixing assumption, enable the estimation of both, the local mole fraction and the local mixing temperature within the LITA probe volume. The temporal evolution indicates that following the subcritical evaporation of the droplet the observed mixing process of acetone vapour in the nitrogen atmosphere in the droplets wake remains also subcritical in close proximity to the droplet. This is in contradiction to the supercritical atmospheric conditions prior to droplet injection. However, with increasing distance the mixing process becomes supercritical due to the increasing nitrogen concentration in the wake. However, since the nitrogen atmosphere with $T_{r,\mathrm{ch}} = 1.01$ and $p_{r,\mathrm{ch}} = 1.28$ is only slightly supercritical, further investigations at higher atmospheric temperatures and/or pressures are necessary to assess and predict the mixing state in the wake of an evaporating droplet in a more general context.

CHAPTER 7

Conclusions and outlook

Within this thesis investigations of macroscopic nearcritical fluid phenomena have been conducted applying laser–induced thermal acoustics. The latter is a seedless, non–intrusive measurement technique based on stimulated Brillouin and Rayleigh scattering. LITA is capable of obtaining different fluid properties, such as speed of sound, acoustic damping rate, and thermal diffusivity, from a single point measurement. This makes LITA a valuable diagnostic tool for studies in evaporation and mixing processes as well as to assess dynamic fluid responses in order to characterise supercritical fluid regimes.

In the previous years LITA has been applied at ITLR in combustion, supersonic flow research, shock tube characterisation, and jet mixing processes. All these investigations have a frequency–based post–processing approach in common to determine speed of sound and flow velocities. On the basis of the existing LITA arrangement, the low–frequency setup has been optimised for application in a high–pressure and high–temperature environment to enable and monitor low energetic excitation beam pulses. The modifications resulted in an improved signal quality with reproducible excitation beam energies and sizes necessary for the time–based modelling approach developed in the scope of this work. Furthermore, a high–speed LITA arrangement has been built enabling transient LITA investigations with a temporal resolution of up to 15 kHz.

7.1 Summary and conclusions

For the investigation of macroscopic nearcritical fluid phenomena a new optically accessible experimental facility has been developed. In contrast to previous chambers the developed test rig operates as a continuous flow reactor and is designed to facilitate atmospheres with a pressure of up to 8 MPa at temperatures up to 773 K. Different top lid designs have been used for studies in pure atmospheres, predefined binary mixtures, gaseous jet mixing processes, and droplet evaporation at nearcritical conditions. For the generation and injection of isolated droplets, a previously developed droplet on demand generator has been applied. Simultaneously to the LITA measurements, the presented macroscopic fluid processes have been observed visually. The flow field visualisation of the gaseous jet mixing process and droplet evaporation has been realised by schlieren imaging and shadowgraphy, respectively. To synchronise LITA to the visual examination, a laser–based triggering system has been designed that coordinates both droplet detachment and time–resolved imaging with the LITA measurements.

In the framework of this thesis a new frequency–based processing routine has been developed to estimate speed of sound data as well as select valid single shot results for signal averaging. The presented analysis includes windowing and a FIR filter to ensure a robust signal evaluation and enable filtering of signals based on the frequency domain. Additionally, a time–based signal modelling methodology has been developed to extract transport properties, such as speed of sound, acoustic damping rate, and thermal diffusivity from the temporal shape of the LITA signal. For this purpose the signal model for finite beam sizes by Cummings et al. [21] and Schlamp et al. [89] has been simplified to ensure robust curve fitting. Prior to its application the developed frequency analysis was validated by measurements in pure fluids and predefined mixtures in a wide temperature and pressure range. The time–based signal modelling approach has been validated against LIGS studies at pressures up to 2.5 MPa by Li et al. [57] as well as thermal relaxation measurements using the tube method by Shields [94, 95] in carbon dioxide.

The validated LITA technique and post–processing approach has been employed to address for three major research objectives. First, investigations in carbon dioxide at gas and gas–like states have been conducted to study acoustic attenuation at nearcritical condition and assess the significance of volume viscosities in complex fluids at high–pressure/density conditions. Besides of a dependency of the acoustic attenuation on the acoustic frequency–pressure ratio, a sharp increase in the volume viscosity has been observed in the vicinity of the critical point. Both are related to an increase of acoustic losses. While the dependency on the acoustic frequency–pressure ratio is caused by a molecular excitation by the induced acoustic wave, the nearcritical increase is related to the singularity of the volume viscosity in the critical point. Furthermore, different theoretical volume viscosity models have been compared to the LITA measurements. Even though the approach by Kustova et al. [51] presents deviations up to three orders of magnitude, it shows the best agreement to the LITA results. The origin of the deviation is assumed to be the molecular excitation by the induced acoustic wave inherent to the LITA technique. Nevertheless, both theoretical and experimental results reveal a significant influence of the volume viscosity at high pressure conditions. Based on these observations, the author concludes that the Stokes' hypothesis to neglect volume viscosities compared to shear viscosities no longer holds. Concordantly, consideration of volume viscosities in the derivation of stress tensor and entropy production becomes vital in numerical simulations and theoretical predictions.

Second, LITA based speed of sound and concentration studies in two radial directions of an argon jet injected into a nitrogen atmosphere show two major results. In addition to a visual characterisation of the length of the LITA probe volume with a beam profiler camera, radial concentration profiles have been used to assess the effective length of the LITA measurement volume. The latter results in a volume of ellipsoid shape smaller than 1.3 mm in length, 246 µm in width and 80 µm in height. Moreover, extracted acoustic damping rates show a dependency on mole fraction, which results from sound absorption due to the diffusion among species. Hence, a well–suited model for acoustic damping rates in mixtures has to consider both the volume viscosity and the additional diffusion related acoustic absorption.

Third, time–resolved LITA studies in the wake of a free falling acetone droplet evaporating in a nitrogen atmosphere at nearcritical conditions have been performed. To the authors knowledge this is the first–time transient LITA measurements have been conducted for the investigation of complex macroscopic fluid phenomena. Since the evaporation and subsequent mixing process is advection dominated, an adiabatic mixing assumption has been applied to evaluate the LITA based speed of sound data. This results in the temporal evolution of both the local nitrogen mole fraction as well as the local mixing temperature. The latter indicates that following the subcritical evaporation of the droplet the observed mixing process of acetone vapour in the nitrogen atmosphere remains subcritical in the vicinity of the droplet .

7.2 Outlook

While the framework of this thesis presents the capability of the LITA technique to simultaneously determine transient speed of sound data and acoustic damping rates, it poses a new challenge for the investigation of mixtures of complex fluids. To determine local mixing states from speed of sound data and acoustic damping rates, a thermodynamic model for both properties is necessary. However, since the acoustic damping rate of a mixture depends on both sound absorption due to species diffusion and the volume viscosity, modelling is challenging. Especially for volume viscosities, models for gases or even mixtures at dense gas conditions are rare. Molecular simulations might have the potential to close this gap. However due to fewer particle interactions the auto–correlation functions decay much slower, leading to simulations with high computational costs. Additionally, depending on the fluid, further losses due to a molecular excitation might occur within the operating acoustic wave frequency–pressure ratio. In such a case, its influence on the modelling approach has to be determined. To further assess supercritical fluid phenomena, Widom–line transition from liquid–like to gas–like states and to provide a database for comparison with molecular simulations, experiments in carbon dioxide or methane in compressible liquid, liquid–like, and gas–like states are envisaged. For this purpose a new pressure chamber with a copper based sealing concept has been built.

Future prospects in transient fluid injection include droplet evaporation and jet disintegration studies at higher temperature conditions. For this purpose an additional top lid has been designed for the integration of a heated fluid injector in the pressure chamber. Additionally, a new bath thermostat was purchased, capable to facilitate investigations with fluid temperature up to 573 K. Regarding droplet evaporation, this enables investigations to examine the state of the mixing process in the wake at higher temperature conditions and make a prediction about the onset of supercritical fluid mixing.

Bibliography

[1] Abernethy, R. B., Benedict, R. P., and Dowdell, R. B.: ASME measurement uncertainty. *Journal of Fluids Engineering*, 1985, 107 (2), pp. 161–164. doi: `10.1115/1.3242450`.

[2] Abramzon, B. and Sirignano, W. A.: Droplet vaporization model for spray combustion calculations. *International Journal of Heat and Mass Transfer*, 1989, 32 (9), pp. 1605–1618. doi: `10.1016/0017-9310(89)90043-4`.

[3] Arima, T., Ruggeri, T., and Sugiyama, M.: Rational extended thermodynamics of a rarefied polyatomic gas with molecular relaxation processes. *Physical Review E*, 2017, 96 (4-1), p. 042143. doi: `10.1103/PhysRevE.96.042143`.

[4] Austin, B. T. and Sumathy, K.: Transcritical carbon dioxide heat pump systems: A review. *Renewable and Sustainable Energy Reviews*, 2011, 15 (8), pp. 4013–4029. doi: `10.1016/j.rser.2011.07.021`.

[5] Baab, S., Förster, F. J., Lamanna, G., and Weigand, B.: Speed of sound measurements and mixing characterization of underexpanded fuel jets with supercritical reservoir condition using laser-induced thermal acoustics. *Experiments in Fluids*, 2016, 57 (11), p. 3068. doi: `10.1007/s00348-016-2252-3`.

[6] Baab, S., Steinhausen, C., Lamanna, G., Weigand, B., and Förster, F. J.: A quantitative speed of sound database for multi-component jet mixing at high pressure. *Fuel*, 2018, 233, pp. 918–925. doi: `10.1016/j.fuel.2017.12.080`.

[7] Banuti, D. T.: Crossing the Widom-line – supercritical pseudo-boiling. *The Journal of Supercritical Fluids*, 2015, 98, pp. 12–16. doi: `10.1016/j.supflu.2014.12.019`.

[8] Banuti, D. T., Raju, M., Ma, P. C., Ihme, M., and Hickey, J.-P.: Seven questions about supercritical fluids - towards a new fluid state diagram. *Proceedings 55th AIAA Aerospace Sciences Meeting: 9 - 13 January 2017, Grapevine, Texas, USA*, 2017, pp. 1–15.

[9] Banuti, D. T., Raju, M., and Ihme, M.: Between supercritical liquids and gases – reconciling dynamic and thermodynamic state transitions. *The Journal of Supercritical Fluids*, 2020, 165 (1). doi: `10.1016/j.supflu.2020.104895`.

[10] Bencivenga, F., Cunsolo, A., Krisch, M., Monaco, G., Ruocco, G., and Sette, F.: High frequency dynamics in liquids and supercritical fluids: A comparative inelastic x-ray scattering study. *The Journal of Chemical Physics*, 2009, 130 (6), p. 064501. doi: `10.1063/1.3073039`.

[11] Boon, J. P. and Yip, S.: Molecular hydrodynamics. New York: Dover Publications, 1991.

[12] Borgelt, P., Hoheisel, C., and Stell, G.: Exact molecular dynamics and kinetic theory results for thermal transport coefficients of the Lennard-Jones argon fluid in a wide region of states. *Physical Review A*, 1990, 42 (2), pp. 789–794.

[13] Bork, B.: Tropfenverdampfung in transkritischer Umgebung: Untersuchung mit laserspektroskopischen Methoden. Ph.D.-Thesis. Darmstadt: Technical University of Darmstadt, 2017.

[14] Bork, B., Preusche, A., Weckenmann, F., Lamanna, G., and Dreizler, A.: Measurement of species concentration and estimation of temperature in the wake of evaporating n-heptane droplets at transcritical conditions. *Proceedings of the Combustion Institute*, 2017, 36 (2), pp. 2433–2440. doi: `10.1016/j.proci.2016.07.037`.

[15] Boyd, R. W.: Nonlinear optics. 3. Amsterdam and Heidelberg: Academic Press, 2008.

[16] Chatwell, R. S. and Vrabec, J.: Bulk viscosity of liquid noble gases. *The Journal of Chemical Physics*, 2020, 152 (9), pp. 094503-094503–9. doi: `10.1063/1.5142364`.

[17] Cramer, M. S.: Numerical estimates for the bulk viscosity of ideal gases. *Physics of Fluids*, 2012, 24 (6), p. 066102. doi: `10.1063/1.4729611`.

[18] Crua, C., Manin, J., and Pickett, L. M.: On the transcritical mixing of fuels at diesel engine conditions. *Fuel*, 2017, 208, pp. 535–548. doi: `10.1016/j.fuel.2017.06.091`.

[19] Cummings, E. B.: Laser-induced thermal acoustics: Simple accurate gas measurements. *Optics Letters*, 1994, 19 (17), pp. 1361–1363. doi: `10.1364/OL.19.001361`.

[20] Cummings, E. B.: Laser-induced thermal acoustics. Ph.D.-Thesis. Pasadena: California Institute of Technology, 1995.

[21] Cummings, E. B., Leyva, I. A., and Hornung, H. G.: Laser-induced thermal acoustics (LITA) signals from finite beams. *Applied Optics*, 1995, 34 (18), pp. 3290–3302. doi: `10.1364/AO.34.003290`.

[22] Dahms, R. N. and Oefelein, J. C.: On the transition between two-phase and single-phase interface dynamics in multicomponent fluids at supercritical pressures. *Physics of Fluids*, 2013, 25 (9), p. 092103. doi: `10.1063/1.4820346`.

[23] Dahms, R. N.: Understanding the breakdown of classic two-phase theory and spray atomization at engine-relevant conditions. *Physics of Fluids*, 2016, 28 (4), p. 042108. doi: `10.1063/1.4946000`.

[24] Demizu, M., Terazima, M., and Kimura, Y.: Transport properties of binary mixtures of carbon dioxide and 1-butyl-3-methylimidazolium hexafluorophosphate studied by transient grating spectroscopy. *Analytical Sciences*, 2008, 24, pp. 1329–1334.

[25] DIN EN 60751:2009-05: *Industrielle Platin-Widerstandsthermometer und Platin-Temperatursensoren (IEC 60751:2008): Deutsche Fassung EN 60751:2008*. Berlin, 2009-05.

[26] Eichler, H.-J., Günter P., and Pohl, D. W.: Laser induced dynamic gratings. Vol. 50. Springer Series in Optical Sciences. Berlin, Heidelberg, and New York: Springer-Verlag, 1986.

[27] Ejakov, S. G., Phillips, S., Dain, Y., Lueptow, R. M., and Visser, J. H.: Acoustic attenuation in gas mixtures with nitrogen: Experimental data and calculations. *The Journal of the Acoustical Society of America*, 2003, 113 (4 Pt 1), pp. 1871–1879. doi: `10.1121/1.1559177`.

[28] Falgout, Z., Rahm, M., Sedarsky, D., and Linne, M.: Gas/fuel jet interfaces under high pressures and temperatures. *Fuel*, 2016, 168, pp. 14–21. doi: `10.1016/j.fuel.2015.11.061`.

[29] Fernández, G. A., Vrabec, J., and Hasse, H.: A molecular simulation study of shear and bulk viscosity and thermal conductivity of simple real fluids. *Fluid Phase Equilibria*, 2004, 221 (1-2), pp. 157–163. doi: `10.1016/j.fluid.2004.05.011`.

[30] Förster, F. J.: Laser-induced thermal acoustics: Simultaneous velocimetry and thermometry for the study of compressible flows. Ph.D.-Thesis. Stuttgart: University of Stuttgart, 2016.

[31] Förster, F. J., Crua, C., Davy, M., and Ewart, P.: Time-resolved gas thermometry by laser-induced grating spectroscopy with a high-repetition rate laser system. *Experiments in Fluids*, 2017, 58 (7), pp. 1–8. doi: `10.1007/s00348-017-2370-6`.

[32] Förster, F. J., Baab, S., Steinhausen, C., Lamanna, G., Ewart, P., and Weigand, B.: Mixing characterization of highly underexpanded fluid jets with real gas expansion. *Experiments in Fluids*, 2018, 59 (3), p. 6247. doi: `10.1007/s00348-018-2488-1`.

[33] Gerber, V., Baab, S., Förster, F. J., Mandler, H., Weigand, B., and Lamanna, G.: Fluid injection with supercritical reservoir conditions: Overview on morphology and mixing. *The Journal of Supercritical Fluids*, 2021, 169, p. 105097. doi: `10.1016/j.supflu.2020.105097`.

[34] Gorelli, F. A., Santoro, M., Scopigno, T., Krisch, M., Bryk, T., Ruocco, G., and Ballerini, R.: Inelastic x-ray scattering from high pressure fluids in a diamond anvil cell. *Applied Physics Letters*, 2009, 94 (7), p. 074102. doi: `10.1063/1.3076123`.

[35] Gorelli, F. A., Bryk, T., Krisch, M., Ruocco, G., Santoro, M., and Scopigno, T.: Dynamics and thermodynamics beyond the critical point. *Scientific Reports*, 2013, 3, p. 1203. doi: `10.1038/srep01203`.

[36] Gross, J. and Sadowski, G.: Perturbed-Chain SAFT: An equation of state based on a perturbation theory for chain molecules. *Industrial & Engineering Chemistry Research*, 2001, 40 (4), pp. 1244–1260. doi: `10.1021/ie0003887`.

[37] Gu, Z. and Ubachs, W.: Temperature-dependent bulk viscosity of nitrogen gas determined from spontaneous Rayleigh–Brillouin scattering. *Optics Letters*, 2013, 38 (7), pp. 1110–1112.

[38] Gyarmathy, G.: The spherical droplet in gaseous carrier streams: Review and synthesis. *Multiphase Science and Technology*, 1982, 1 (1-4), pp. 99–279.

[39] Harris, F. J.: On the use of windows for harmonic analysis with the discrete Fourier transform. *Proceedings of the IEEE*, 1978, 66 (1), pp. 51–83. doi: `10.1109/PROC.1978.10837`.

[40] Harris, J. G. and Yung, K. H.: Carbon dioxide's liquid-vapor coexistence curve and critical properties as predicted by a simple molecular model. *The Journal of Physical Chemistry*, 1995, 99 (31), pp. 12021–12024. doi: `10.1021/j100031a034`.

[41] Hell, A.: Validierung der Lasermesstechnik Laser-induzierte Thermische Akustik für die Anwendung in turbulenten, chemisch reagierenden Überschallfreistrahlen. Ph.D.-Thesis. Stuttgart: University of Stuttgart, 2012.

[42] Hemmerling, B. and Kozlov, D. N.: Generation and temporally resolved detection of laser-induced gratings by a single, pulsed Nd:YAG laser. *Applied Optics*, 1999, 38 (6), p. 1001. doi: `10.1364/AO.38.001001`.

[43] Hemmerling, B. and Kozlov, D. N.: Collisional relaxation of singlet O2 in neat gas investigated by laser-induced grating technique. *Chemical Physics*, 2003, 291 (3), pp. 213–242. doi: `10.1016/S0301-0104(03)00226-X`.

[44] Herzfeld, K. F. and Litovitz, T. A.: Absorption and dispersion of ultrasonic waves. New York and London: Academic Press, 1959.

[45] ISO 1219-1:2012-06: *Fluid power systems and components - graphical symbols and circuit diagrams - part 1: Graphical symbols for conventional use and data-processing applications*. Berlin, 2012-06.

[46] Jaeger, F., Matar, O. K., and Müller, E. A.: Bulk viscosity of molecular fluids. *The Journal of Chemical Physics*, 2018, 148 (17), p. 174504. doi: `10.1063/1.5022752`.

[47] Joint Committee for Guides in Metrology: Evaluation of measurement data - guide to the expression of uncertainty in measurement: GUM 1995 with minor corrections. JCGM 100:2008, 2008.

[48] Kimura, Y., Kanda, D., Terazima, M., and Hirota, N.: Application of the transient grating method to the measurement of transport properties for high pressure fluids. *Physical Chemistry Chemical Physics*, 1995, 99 (2), pp. 196–203. doi: `10.1002/bbpc.19950990214`.

[49] Kimura, Y., Yamamoto, Y., Fujiwara, H., and Terazima, M.: Vibrational energy relaxation of azulene studied by the transient grating method. I. Supercritical fluids. *The Journal of Chemical Physics*, 2005, 123 (5), p. 054512. doi: `10.1063/1.1994847`.

[50] Kimura, Y., Yamamoto, Y., and Terazima, M.: Vibrational energy relaxation of azulene studied by the transient grating method. II. Liquid solvents. *The Journal of Chemical Physics*, 2005, 123 (5), p. 054513. doi: `10.1063/1.1994848`.

[51] Kustova, E., Mekhonoshina, M., and Kosareva, A.: Relaxation processes in carbon dioxide. *Physics of Fluids*, 2019, 31 (4), p. 046104. doi: `10.1063/1.5093141`.

[52] Lamanna, G., Steinhausen, C., Weigand, B., Preusche, A., Bork, B., Dreizler, A., Stierle, R., and Gross, J.: On the importance of non-equilibrium models for describing the coupling of heat and mass transfer at high pressure. *International Communications in Heat and Mass Transfer*, 2018, 98, pp. 49–58. doi: `10.1016/j.icheatmasstransfer.2018.07.012`.

[53] Lamanna, G., Steinhausen, C., Weckenmann, F., Weigand, B., Bork, B., Preusche, A., Dreizler, A., Stierle, R., and Gross, J.: Laboratory experiments of high-pressure fluid drops: Chapter 2. *American Institute of Aeronautics and Astronautics (Hg.) – High-Pressure Flows for Propulsion Applications*, 2020, pp. 49–109. doi: `10.2514/5.9781624105814.0049.0110`.

[54] Lamanna, G.: Supercritical fluids: Properties and applications. World Scientific Series on Emerging Technologies: Volume 5. Singapur: World Scientific Publishing, to appear in 2023. doi: `10.1142/13262`.

[55] Latzel, H. and Dreier, T.: Sound velocity, heat conduction and virial coefficients of gaseous mixtures at high pressure from NIR laser-induced grating experiments. *Physical Chemistry Chemical Physics*, 2000, 2 (17), pp. 3819–3824. doi: `10.1039/b003271i`.

[56] Lemmon, E. W., Bell, I. H., Huber, M. L., and McLinden, M. O.: *NIST standard reference database 23: Reference fluid thermodynamic and transport properties-REFPROP, version 10.0, National Institute of Standards and Technology.* 2018. doi: `10.18434/T4JS3C`.

[57] Li, Y., Roberts, W. L., and Brown, M. S.: Investigation of gaseous acoustic damping rates by transient grating spectroscopy. *AIAA Journal*, 2002, 40 (6), pp. 1071–1077. doi: `10.2514/2.1790`.

[58] Li, Y., Roberts, W. L., Brown, M. S., and Gord, J. R.: Acoustic damping rate measurements in binary mixtures of atomic species via transient-grating spectroscopy. *Experiments in Fluids*, 2005, 39 (4), pp. 687–693. doi: `10.1007/s00348-005-1012-6`.

[59] Malbrunot, P., Boyer, A., Charles, E., and Abachi, H.: Experimental bulk viscosities of argon, krypton, and xenon near their triple point. *Physical Review A*, 1983, 27 (3), pp. 1523–1534. doi: `10.1103/PhysRevA.27.1523`.

[60] Marchionni, M., Bianchi, G., and Tassou, S. A.: Review of supercritical carbon dioxide (sCO2) technologies for high-grade waste heat to power conversion. *SN Applied Sciences*, 2020, 2 (4). doi: `10.1007/s42452-020-2116-6`.

[61] MATLAB: 9.4.0.813654 (R2018a). Natick: The MathWorks Inc., 2018.

[62] Meier, K., Laesecke, A., and Kabelac, S.: Transport coefficients of the Lennard-Jones model fluid. III. Bulk viscosity. *The Journal of Chemical Physics*, 2005, 122 (1), p. 14513. doi: `10.1063/1.1828040`.

[63] Mo, G. and Qiao, L.: A molecular dynamics investigation of n-alkanes vaporizing into nitrogen: Transition from subcritical to supercritical. *Combustion and Flame*, 2017, 176, pp. 60–71.

[64] Moffat, R. J.: Describing the uncertainties in experimental results. *Experimental Thermal and Fluid Science*, 1988, 1 (1), pp. 3–17. doi: `10.1016/0894-1777(88)90043-X`.

[65] Müller, H., Niedermeier, C. A., Matheis, J., Pfitzner, M., and Hickel, S.: Large-eddy simulation of nitrogen injection at trans- and supercritical conditions. *Physics of Fluids*, 2016, 28 (1), p. 015102. doi: `10.1063/1.4937948`.

[66] Mysik, S. V.: Analyzing the acoustic spectra of sound velocity and absorption in amphiphilic liquids. *St. Petersburg Polytechnical University Journal: Physics and Mathematics*, 2015, 1 (3), pp. 325–331. doi: `10.1016/j.spjpm.2015.12.003`.

[67] Naugle, D. G., Lunsford, J. H., and Singer, J. R.: Volume viscosity in liquid argon at high pressures. *The Journal of Chemical Physics*, 1966, 45 (12), pp. 4669–4676. doi: `10.1063/1.1727553`.

[68] Nomura, H., Nakaya, S., and Tsue, M.: Microgravity research on quasi-steady and unsteady combustion of fuel droplet at high pressures: Chapter 1. *American Institute of Aeronautics and Astronautics (Hg.) – High-Pressure Flows for Propulsion Applications*, 2020, pp. 1–47. doi: `10.2514/5.9781624105814.0001.0048`.

[69] Oldenhof, E., Weckenmann, F., Lamanna, G., Weigand, B., Bork, B., and Dreizler, A.: Experimental investigation of isolated acetone droplets at ambient and near-critical conditions, injected in a nitrogen atmosphere. *Progress in Propulsion Physics: 4-8 July 2011, St. Petersburg, Russian*, 2013, Volume 4, pp. 257–270. doi: `10.1051/eucass/201304257`.

[70] Oppenheim, A. V., Schafer, R. W., and Buck, J. R.: Discrete-time signal processing. 2nd. ed. Upper Saddle River: Prentice-Hall, 1999.

[71] Oschwald, M., Smith, J. J., Branam, R., Hussong, J., Schik, A., Chehroudi, B., and Talley, D.: Injection of fluids into supercritical environments. *Combustion Science and Technology*, 2006, 178 (1-3), pp. 49–100. doi: `10.1080/00102200500292464`.

[72] Ouedraogo, Y., Gjonaj, E., Weiland, T., Gersem, H. de, Steinhausen, C., Lamanna, G., Weigand, B., Preusche, A., Dreizler, A., and Schremb, M.: Electrohydrodynamic simulation of electrically controlled droplet generation. *International Journal of Heat and Fluid Flow*, 2017, 64, pp. 120–128. doi: `10.1016/j.ijheatfluidflow.2017.02.007`.

[73] Palmetshofer, P., Steinhausen, C., Preusche, A., Dreizler, A., Weigand, B., and Lamanna, G.: Comparison of diffusion models for application in low- to high-pressure droplet evaporation problems. *Proceedings ICLASS 2018, 14th Triennial International Conference on Liquid Atomization and Spray Systems: July 22-26 2018, Chicago, IL, USA*, 2018.

[74] Paschotta, R.: Encyclopedia of laser physics and technology: Volume A – M. Weinheim: WILEY-VCH, 2008.

[75] Pecnik, R., Rinaldi, E., and Colonna, P.: Computational fluid dynamics of a radial compressor operating with supercritical CO2. *Journal of Engineering for Gas Turbines and Power*, 2012, 134 (12). doi: `10.1115/1.4007196`.

[76] Pinheiro, A. P. and Vedovoto, J. M.: Evaluation of droplet evaporation models and the incorporation of natural convection effects. *Flow, Turbulence and Combustion*, 2019, 102 (3), pp. 537–558. doi: `10.1007/s10494-018-9973-8`.

[77] Pizzarelli, M., Nasuti, F., and Onofri, M.: CFD analysis of transcritical methane in rocket engine cooling channels. *The Journal of Supercritical Fluids*, 2012, 62, pp. 79–87. doi: `10.1016/j.supflu.2011.10.014`.

[78] Pizzarelli, M., Nasuti, F., Onofri, M., Roncioni, P., Votta, R., and Battista, F.: Heat transfer modeling for supercritical methane flowing in rocket engine cooling channels. *Applied Thermal Engineering*, 2015, 75, pp. 600–607. doi: `10.1016/j.applthermaleng.2014.10.008`.

[79] Pizzarelli, M.: The status of the research on the heat transfer deterioration in supercritical fluids: A review. *International Communications in Heat and Mass Transfer*, 2018, 95, pp. 132–138. doi: `10.1016/j.icheatmasstransfer.2018.04.006`.

[80] Powers, P. E.: Field guide to nonlinear optics. Vol. FG29. SPIE field guide series. Bellingham: SPIE Press, 2013.

[81] Preusche, A., Dreizler, A., Steinhausen, C., Lamanna, G., and Stierle, R.: Non-invasive, spatially averaged temperature measurements of falling acetone droplets in nitrogen atmosphere at elevated pressures and temperatures. *The Journal of Supercritical Fluids*, 2020, 166, p. 105025. doi: `10.1016/j.supflu.2020.105025`.

[82] Preusche, A.: Non-invasive thermometry and wake mixture fraction determination of evaporating droplets at elevated pressures using laser spectroscopy. Ph.D.-Thesis. Darmstadt: Technical University of Darmstadt, 2021.

[83] Qiao, L., Jain, S., and Mo, G.: Molecular simulations to research supercritical fuel properties: Chapter 10. *American Institute of Aeronautics and Astronautics (Hg.) – High-Pressure Flows for Propulsion Applications*, 2020, pp. 409–460. doi: `10.2514/5.9781624105814.0409.0460`.

[84] Qiu, L. and Reitz, R. D.: An investigation of thermodynamic states during high-pressure fuel injection using equilibrium thermodynamics. *International Journal of Multiphase Flow*, 2015, 72, pp. 24–38. doi: `10.1016/j.ijmultiphaseflow.2015.01.011`.

[85] Richter, J., Mayer, J., and Weigand, B.: Accuracy of non-resonant laser-induced thermal acoustics (LITA) in a convergent–divergent nozzle flow. *Applied Physics B: Lasers and Optics*, 2018, 124 (2), p. 235. doi: `10.1007/s00340-017-6885-6`.

[86] Rozouvan, S. and Dreier, T.: Polarization-dependent laser-induced grating measurements. *Optics Letters*, 1999, 24 (22), pp. 1596–1598. doi: `10.1364/ol.24.001596`.

[87] Santoro, M. and Gorelli, F. A.: Structural changes in supercritical fluids at high pressures. *Physical Review B*, 2008, 77 (21). doi: `10.1103/PhysRevB.77.212103`.

[88] Schaumäker, A.: Inbetriebnahme und Charakterisierung der Hochdruck-Hochtemperatur-Tropfenkammer. Bachelor-Thesis. Stuttgart: University of Stuttgart, 2018.

[89] Schlamp, S., Cummings, E. B., and Hornung, H. G.: Beam misalignments and fluid velocities in laser-induced thermal acoustics. *Applied Optics*, 1999, 38 (27), pp. 5724–5733. doi: `10.1364/AO.38.005724`.

[90] Settles, G. S.: Schlieren and shadowgraph techniques: Visualizing phenomena in transparent media. Engineering online library. Berlin, Heidelberg, and New York: Springer-Verlag, 2001.

[91] Shang, J., Wu, T., Wang, H., Yang, C., Ye, C., Hu, R., Tao, J., and He, X.: Measurement of temperature-dependent bulk viscosities of nitrogen, oxygen and air from spontaneous Rayleigh-Brillouin scattering. *IEEE Access*, 2019, 7, pp. 136439–136451. doi: `10.1109/ACCESS.2019.2942219`.

[92] Shang, J., Wu, T., Wang, H., Xu, W., Ye, C., Hu, R., Tao, J., and He, X.: Measurement of bulk viscosity of CO2 based on spontaneous Rayleigh-Brillouin scattering. *IEEE Access*, 2020, 8, pp. 40909–40917. doi: `10.1109/ACCESS.2020.2976883`.

[93] Sharma, B. and Kumar, R.: Estimation of bulk viscosity of dilute gases using a nonequilibrium molecular dynamics approach. *Physical Review E*, 2019, 100 (1-1), p. 013309. doi: `10.1103/PhysRevE.100.013309`.

[94] Shields, F. D.: Thermal relaxation in carbon dioxide as a function of temperature. *The Journal of the Acoustical Society of America*, 1957, 29 (4), pp. 450–454. doi: `10.1121/1.1908924`.

[95] Shields, F. D.: Measurements of thermal relaxation in CO2 extended to 300°C. *The Journal of the Acoustical Society of America*, 1959, 31, pp. 248–249. doi: `10.1121/1.1907705`.

[96] Shields, F. D.: Sound absorption in the halogen gases. *The Journal of the Acoustical Society of America*, 1960, 32 (2), pp. 180–185. doi: `10.1121/1.1908006`.

[97] Siegman, A. E.: Bragg diffraction of a Gaussian beam by a crossed–Gaussian volume grating. *Journal of the Optical Society of America*, 1977, 67 (4), pp. 545–550.

[98] Simeoni, G. G., Bryk, T., Gorelli, F. A., Krisch, M., Ruocco, G., Santoro, M., and Scopigno, T.: The Widom line as the crossover between liquid-like and gas-like behaviour in supercritical fluids. *Nature Physics*, 2010, 6 (7), pp. 503–507. doi: `10.1038/nphys1683`.

[99] Stampanoni-Panariello, A., Hemmerling, B., and Hubschmid, W.: Electrostrictive generation of nonresonant gratings in the gas phase by multimode lasers. *Physical Review A*, 1995, 51 (1), pp. 655–662.

[100] Stampanoni-Panariello, A., Kozlov, D. N., Radi, P. P., and Hemmerling, B.: Gas phase diagnostics by laser-induced gratings I. Theory. *Applied Physics B*, 2005, 81 (1), pp. 101–111. doi: `10.1007/s00340-005-1852-z`.

[101] Stampanoni-Panariello, A., Kozlov, D. N., Radi, P. P., and Hemmerling, B.: Gas-phase diagnostics by laser-induced gratings II. Experiments. *Applied Physics B*, 2005, 81 (1), pp. 113–129. doi: `10.1007/s00340-005-1853-y`.

[102] Stein, M.: Validierung des LITA-Messsystems an der Hochdruck-Hochtemperaturkammer. Bachelor-Thesis. Stuttgart: University of Stuttgart, 2019.

[103] Steinhausen, C.: Definition und Anwendung des Datenanalyseprozesses für Wärmeübergangs- und Filmkühleffektivitätsmessungen am Large Scale Turbine Rig (LSTR). Master-Thesis. Darmstadt: Technical University of Darmstadt, 2015.

[104] Steinhausen, C., Lamanna, G., Weigand, B., Stierle, R., Gross, J., Preusche, A., and Dreizler, A.: Experimental investigation of droplet injections in the vicinity of the critical point: A comparison of different model approaches. *Proceedings ILASS–Europe 2017. 28th Conference on Liquid Atomization and Spray Systems: 6-8 September 2017, Valencia, Spain*, 2017. doi: `10.4995/ILASS2017.2017.4635`.

[105] Steinhausen, C., Lamanna, G., Weigand, B., Stierle, R., Gross, J., Preusche, A., Dreizler, A., and Sierra-Pallares, J.: On the influence of evaporation on the mixture formation of high pressure combustion. *Proceedings ICMF 2019, 10th International Conference on Multiphase Flow: May 19 – 24, 2019, Rio de Janeiro, Brazil*, 2019.

[106] Steinhausen, C., Reutzsch, J., Lamanna, G., Weigand, B., Stierle, R., Gross, J., Preusche, A., and Dreizler, A.: Droplet evaporation under high pressure and temperature conditions: A comparison of droplet evaporation under high pressure and temperature conditions. *Proceedings ILASS–Europe 2019, 29th Conference on Liquid Atomization and Spray Systems: 2-4 September 2019, Paris, France*, 2019.

[107] Steinhausen, C., Gerber, V., Preusche, A., Weigand, B., Dreizler, A., and Lamanna, G.: On the potential and challenges of laser-induced thermal acoustics for experimental investigation of macroscopic fluid phenomena. *Experiments in Fluids*, 2021, 62 (2). doi: `10.1007/s00348-020-03088-1`.

[108] Steinhausen, C., Gerber, V., Preusche, A., Dreizler, A., Weigand, B., and Lamanna, G.: Feasibility analysis on transient speed of sound investigations using laser–induced thermal acoustics in evaporating droplets. *Proceedings of the 20th International Symposium on Application of Laser and Imaging Techniques to Fluid Mechanics: 11-14 July 2022, Lisbon, Portugal*, 2022.

[109] Stephan, P., Schaber, K., Stephan, K., and Mayinger, F.: Thermodynamik: Grundlagen und technische Anwendungen Band 2: Mehrstoffsysteme und chemische Reaktionen. 15., neu bearb. Aufl. Heidelberg, Dordrecht, London, and New York: Springer, 2010.

[110] Stierle, R., Waibel, C., Gross, J., Steinhausen, C., Weigand, B., and Lamanna, G.: On the selection of boundary conditions for droplet evaporation and condensation at high pressure and temperature conditions from interfacial transport resistivities. *International Journal of Heat and Mass Transfer*, 2020, 151, p. 119450. doi: `10.1016/j.ijheatmasstransfer.2020.119450`.

[111] Still, T.: High frequency acoustics in colloid-based meso- and nanostructures by spontaneous Brillouin light scattering. Ph.D.-Thesis. Mainz: Johannes Gutenberg University Mainz, 2009.

[112] Tisza, L.: Supersonic absorption and Stokes' viscosity relation. *Physical Review*, 1942, 61, pp. 531–536. doi: `10.1103/PhysRev.61.531`.

[113] Wang, Y., Ubachs, W., and van de Water, W.: Bulk viscosity of CO2 from Rayleigh-Brillouin light scattering spectroscopy at 532 nm. *The Journal of Chemical Physics*, 2019, 150 (15), pp. 154502-154502–10. doi: `10.1063/1.5093541`.

[114] Weckenmann, F., Bork, B., Oldenhof, E., Lamanna, G., Weigand, B., Böhm, B., and Dreizler, A.: Single acetone droplets at supercritical pressure: Droplet generation and characterization of PLIFP. *Zeitschrift für Physikalische Chemie*, 2011, 225 (11-12), pp. 1417–1431.

[115] Weckenmann, F., Lamanna, G., Weigand, B., Bork, B., and Dreizler, A.: Experimental investigation of droplet injections in the vicinity of the critical point. *Proceedings 14th European Meeting on Supercritical Fluids: 18-21 May 2014, Marseille, France*, 2014.

[116] Weckenmann, F.: Experimental incestigation of isolated fluid particles under extreme conditions. Ph.D.-Thesis. Stuttgart: University of Stuttgart, 2019.

[117] Wilke, C. R. and Lee, C. Y.: Estimation of diffusion coefficients for gases and vapors. *Industrial & Engineering Chemistry*, 1955, 47 (6), pp. 1253–1257. doi: `10.1021/ie50546a056`.

[118] Willman, C., Le Page, L. M., Ewart, P., and Williams, B. A. O.: Pressure measurement in gas flows using laser-induced grating lifetime. *Applied Optics*, 2021, 60 (15), pp. C131–C141. doi: `10.1364/AO.419973`.

[119] Young, J. B.: The condensation and evaporation of liquid droplets at arbitrary Knudsen number in the presence of an inert gas. *International Journal of Heat and Mass Transfer*, 1993, 36 (11), pp. 2941–2956.

[120] Zierep, J.: Theory of flows in compressible media with heat addition. *AGARD*, 1974, Report AG 191.

APPENDIX A

Uncertainty analysis and error estimation

The uncertainty analysis applied in this work is performed following the guide to the expression of uncertainty in measurement (GUM) by the Joint Committee for Guides in Metrology [47]. One of the advantages of the GUM [47] compared to other regulations such as the study by Abernethy et al. [1] is the differentiation between statistical and systematical errors. The latter are considered independently from each other by Abernethy et al. [1] and then propagated and combined at the end of the uncertainty analysis. In contrast, such a distinction is avoided in the GUM [47], which circumvents ambiguities of the uncertainties in the error propagation. Instead, measurement uncertainties of the input quantities are divided into two types. Type A are uncertainties obtained by statistical analysis with a know probability distribution. In comparison, Type B uncertainties are not based on the statistical data analysis of the measurements and usually result from sensor or database uncertainties, discretisation, etcetera. Note that the probability density function might be unknown and has to be specified. In the following the methodology for the evaluation of measurement uncertainties used in this thesis is briefly summarised. Note that a similar summary has already been published in the authors Master thesis [103].

A.1 Measurement uncertainties of the input quantities

An overview of the measurement uncertainties of the input quantities is presented in Tab. A.1. The error types as well as the applied probability distributions are listed together with the sources and if possible the values.

Table A.1: Measurement uncertainties of the input parameters.

quantity	type	value	probability distribution	source
Δp_meas	A	N/A	Gauss	measurement
Δp_35XHTC	B	±0.05 MPa	Gauss	data sheet
ΔT_meas	A	N/A	Gauss	measurement
ΔT_PT100A	B	Eqn. (A.1)	equal	DIN EN 60751 [25]
$\Delta T_\mathrm{Agilent}$	B	±0.06 K	equal	data sheet
$\Delta \Omega_{j\,c_s}$	B	±78.3 kHz	equal	DFT discretisation
$\Delta\lambda_\mathrm{int}$	B	±2.37 fm	Gauss	data sheet
$\Delta\lambda_\mathrm{exc,lowFreq.}$	B	±0.06 nm	Gauss	data sheet
$\Delta\lambda_\mathrm{exc,Hi.Speed}$	B	±0.10 nm	Gauss	data sheet
$\Delta\sigma_0$	B	±112.5 µm	Gauss	data sheet
$\Delta c_{s,\mathrm{NIST,Ar,rel}}$	B	±1.0 %	Gauss	NIST Database [56]
$\Delta c_{s,\mathrm{NIST,N_2,rel}}$	B	±0.1 %	Gauss	NIST Database [56]
$\Delta D_{T,\mathrm{NIST,Ar,rel}}$	B	±2 %	Gauss	NIST Database [56]
$\Delta D_{T,\mathrm{NIST,N_2,rel}}$	B	±3 %	Gauss	NIST Database [56]
$\Delta D_{T,\mathrm{NIST,CO_2,rel}}$	B	±5 %	Gauss	NIST Database [56]
$\Delta c_{p,\mathrm{NIST,Ar,rel}}$	B	±0.30 %	Gauss	NIST Database [56]
$\Delta c_{p,\mathrm{NIST,N_2,rel}}$	B	±0.30 %	Gauss	NIST Database [56]
$\Delta c_{p,\mathrm{NIST,CO_2,rel}}$	B	±0.15 %	Gauss	NIST Database [56]
$\Delta k_\mathrm{NIST,Ar,rel}$	B	±2 %	Gauss	NIST Database [56]
$\Delta k_\mathrm{NIST,N_2,rel}$	B	±3 %	Gauss	NIST Database [56]
$\Delta k_\mathrm{NIST,CO_2,rel}$	B	±5 %	Gauss	NIST Database [56]
$\Delta\varrho_\mathrm{NIST,Ar,rel}$	B	±0.20 %	Gauss	NIST Database [56]
$\Delta\varrho_\mathrm{NIST,N_2,rel}$	B	±0.20 %	Gauss	NIST Database [56]
$\Delta\varrho_\mathrm{NIST,CO_2,rel}$	B	±0.05 %	Gauss	NIST Database [56]
$\Delta\mu_{s,\mathrm{NIST,Ar,rel}}$	B	±1 %	Gauss	NIST Database [56]
$\Delta\mu_{s,\mathrm{NIST,N_2,rel}}$	B	±2 %	Gauss	NIST Database [56]
$\Delta\mu_{s,\mathrm{NIST,CO_2,rel}}$	B	±3 %	Gauss	NIST Database [56]

As listed in Tab. A.1, three input quantities are necessary for the determination of the uncertainty of the temperature measurements. The uncertainty of the sensor electronic is denoted with $\Delta T_{\mathrm{Agilent}}$, while the uncertainty of the used resistance thermometers $\Delta T_{\mathrm{PT100A}}$ of type PT100A is calculated according to DIN EN 60751:2009-05 [25]. Since equation (A.1) specifies the error limit [25], an equal probability distribution within is assumed.

$$\Delta T_{\mathrm{PT100A}} = \pm \left(0.15 + 0.002 \left| \frac{T - 273.15\,\mathrm{K}}{\mathrm{K}} \right|\right) \mathrm{K} \tag{A.1}$$

Note that according to the GUM [47] the standard deviation of a Gaussian distribution can be computed from an equal probability distribution by dividing the error limits by $\sqrt{3}$. The discretisation in the frequency domain due to the DFT algorithm is considered by $\Delta \mathit{\Omega}_{j\,c_s}$, while the uncertainty of the pressure sensor is taken into account by $\Delta p_{\mathrm{35XHTC}}$.

A.2 Determination of the combined standard uncertainty

Following the GUM [47], the combined standard uncertainty $\epsilon\left(\delta_a\right)$ of an input quantity δ_a is defined by the positive square root of the combined squares of the uncertainty contributions. Note that all contributions have to assume a Gaussian probability distribution. When a computed value Υ depends on uncertain input values δ

$$\Upsilon = f\left(\delta_1,\ldots,\delta_a,\ldots,\delta_g\right) \ , \tag{A.2}$$

the uncertainty of the computed value $\Delta\Upsilon$ has to be determined via error propagation. For differentiable terms with independent input quantities the propagation of uncertainties is conducted using the Gaussian error propagation as suggested in the GUM [47]. The latter is defined by

$$\Delta\Upsilon = \left[\sum_{a=1}^{g} \left(\frac{\partial \Upsilon}{\partial \delta_a}\right)^2 \epsilon^2\left(\delta_a\right)\right]^{1/2} \ . \tag{A.3}$$

In case of non–differentiable dependencies, such as values taken from the NIST database [56] or curve fitting algorithms, the uncertainties of input parameters are propagated by applying sequential perturbation as suggested by Moffat [64] presented in equation (A.4). Note that by using the sequential perturbation method a Gaussian distribution is inherently assumed. Uncertainties of the NIST database by Lemmon et al. [56] or the presented curve fitting algorithms are considered following the combined standard uncertainty suggestion in the GUM [47].

$$\begin{aligned} \delta_{a,+} &= \left|\Upsilon\left(\delta_1,\ldots,\delta_a+\epsilon\left(\delta_a\right),\ldots,\delta_g\right)-\Upsilon\right| \\ \delta_{a,-} &= \left|\Upsilon\left(\delta_1,\ldots,\delta_a-\epsilon\left(\delta_a\right),\ldots,\delta_g\right)-\Upsilon\right| \\ \epsilon\left(\delta_a\right) &= \frac{1}{2}\left(\delta_{a,+}+\delta_{a,-}\right) \\ \Delta\Upsilon &= \left[\sum_{a=1}^{g}\epsilon^2\left(\delta_a\right)\right]^{1/2} \end{aligned} \tag{A.4}$$

A.3 Consideration of the temperature distribution

The overall chamber temperature is computed with a volume weighted average

$$T_{\mathrm{ch}} = 0.4\,T_{\mathrm{Top}} + 0.2\,T_{\mathrm{Middle}} + 0.4\,T_{\mathrm{Bottom}}\ . \tag{A.5}$$

To account for the temperature distribution the resulting uncertainty contribution ΔT_{dist} is approximated as

$$\begin{aligned} \left[\Delta T_{\mathrm{dist}}\right]^2 =& 0.4\left(T_{\mathrm{Top}}-T_{\mathrm{ch}}\right)^2+0.2\left(T_{\mathrm{Middle}}-T_{\mathrm{ch}}\right)^2+ \\ & 0.4\left(T_{\mathrm{Bottom}}-T_{\mathrm{ch}}\right)^2\ . \end{aligned} \tag{A.6}$$

The measurement uncertainty for the temperature is then estimated by applying the Gaussian error propagation of equation (A.3) to equation (A.5) and considering the contribution ΔT_{dist} with the combined standard uncertainty approach. To ensure the measurement uncertainty accounts for large distributions a 99% confidence interval is used.

APPENDIX B

Further acoustic damping results

In the following appendix, additional acoustic damping results in nitrogen and predefined binary mixtures are presented. Due to a lack in theoretical models a comparison of the LITA obtained results is not possible.

B.1 Acoustic damping results in binary mixtures

Figure B.1 exemplarily presents detected signals together with their curve fits recorded in an argon–helium mixture and a nitrogen–carbon dioxide mixture. The operating conditions, concentrations, curve fitting input parameters, and results are listed in Tab. B.1. Uncertainties are hereby listed using a 68% confidence interval. Both measurements are performed with a SM fibre. In case of the N_2–CO_2 mixture a resonant fluid behaviour is observed. As discussed previously, this is most likely a result of residual moisture in the peripheral pipe system. However, due to the low modulation depth of the thermal grating compared to the electrostrictive grating, $|\mathcal{U}_\Theta/\mathcal{U}_{eP}| < 0.01$, the resonant contribution of the fluid response is weak. The fitted thermal diffusivity does therefore not reveal physically reasonable results. Hence, it is not listed in Tab. B.1.

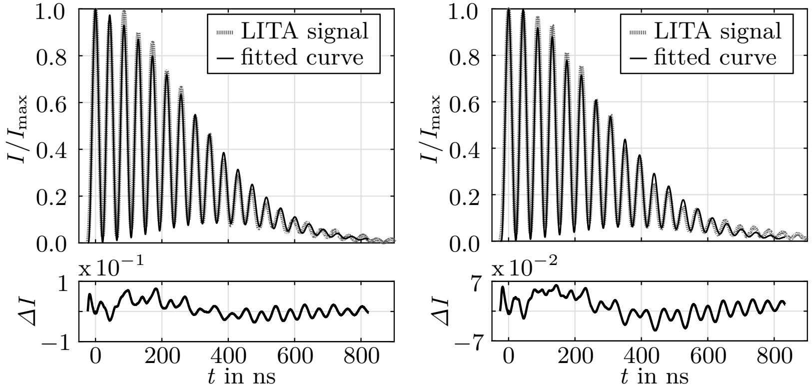

(a) Case 231; low frequency LITA setup with SM fibre; non–resonant fluid behaviour.

(b) Case 304; low frequency LITA setup with SM fibre; resonant fluid behaviour.

Figure B.1: Curve fitting results and measured LITA signals in a Ar–He and N_2–CO_2 mixture. Fitting is used to estimate c_s and Γ. Operating conditions, input parameters, and results are listed in Tab. B.1.

Table B.1: Overview of operating conditions, input parameters, and curve fitting results for the binary mixture cases shown in Fig. B.1. Curve fitting is used to estimate c_s and Γ. Uncertainties are listed using a 68% confidence interval.

	operating conditions				input parameters	
Case	fluid	p_{ch} in MPa	T_{ch} in K	o	ω_{cal} in µm	Λ_{cal} in µm
231	Ar–He (0.9/0.1)	4 ± 0.05	301 ± 0.7	459	153 ± 33	29.47 ± 0.05
304	N_2–CO_2 (0.8/0.2)	4 ± 0.05	301 ± 0.6	2954	163 ± 32	29.47 ± 0.05

	input parameters		curve fitting results		
Case	σ_{th} in µm	model	$\lvert\mathcal{U}_{\Theta}/\mathcal{U}_{eP}\rvert$	$c_{s,\mathrm{LITA}}$ in $\mathrm{m\,s^{-1}}$	Γ_{LITA} in $\mathrm{mm^2\,s^{-1}}$
231	151 ± 16	small detector limit	0	343 ± 1	1.89 ± 3.3
304	151 ± 16	small detector limit	0.01	336 ± 1	3.55 ± 5.8

The ratio between acoustic damping rates obtained by LITA $\mathit{\Gamma}_{\mathrm{LITA}}$ and the classical acoustic damping rate $\mathit{\Gamma}_{c,\mathrm{NIST}}$ taken from the NIST database by Lemmon et al. [56] is presented in Fig. B.2 for investigations in the mixtures and their operating conditions presented in Tab. 5.3. Note that measurement uncertainties are omitted for clearity and points at similar pressure conditions indicate experiments, which were investigated on different days. Deviations between those points are caused by beam steering effects or are a result of staining of the quartz windows. The latter can influence the Gaussian beam width of the excitation beams without changing the beam crossing angle.

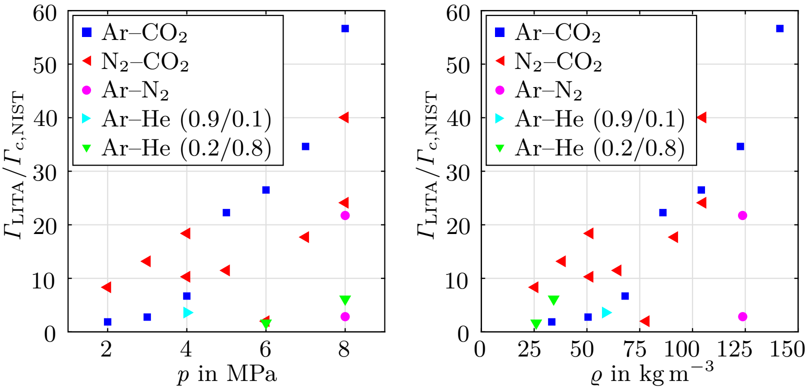

(a) $\mathit{\Gamma}/\mathit{\Gamma}_c$ over pressure.

(b) $\mathit{\Gamma}/\mathit{\Gamma}_c$ over density.

Figure B.2: Acoustic damping rate ratio over pressure and density for the predefined binary mixtures listed in Tab. 3.1 measured at $T_{\mathrm{ch}} = 301\,\mathrm{K}$. Values are computed using LITA extracted acoustic damping rates Γ_{LITA}. Thermodynamic data to compute $\mathit{\Gamma}_c$ are taken from Lemmon et al. [56].

B.2 Volume viscosity in nitrogen at dense gas conditions

Experimental volume viscosities μ_v for nitrogen are estimated with equation (2.16) exploiting the difference between LITA extracted acoustic damping rates $\mathit{\Gamma}_{\mathrm{LITA}}$ and classical acoustic damping rates $\mathit{\Gamma}_{c,\mathrm{NIST}}$ calculated with values taken from the NIST database by Lemmon et al. [56].

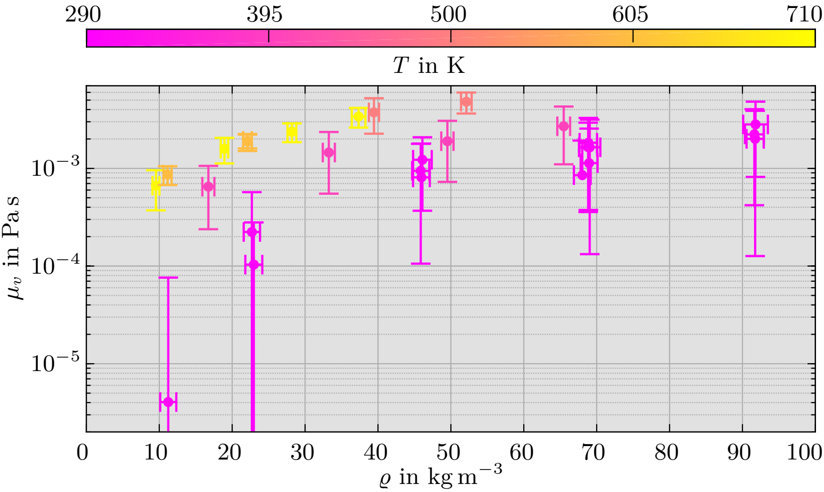

Figure B.3: Experimental volume viscosity μ_v over density ϱ for pure nitrogen. Experimental volume viscosities are computed with equation (2.16) using LITA extracted acoustic damping rates Γ_{LITA}. Uncertainties are displayed using a 95% confidence interval. Thermodynamic data of the binary mixtures are taken from Lemmon et al. [56].

The LITA extracted volume viscosities are plotted in Fig. B.3 and Fig. B.4a. Note that for clarity measurement uncertainties in Fig. B.4 are omitted, whereas in Fig. B.3 uncertainties are displayed using a 95% confidence interval. The viscosity ratio μ_v/μ_s is shown in Fig. B.4b. The shear viscosity is hereby computed using the NIST database by Lemmon et al. [56]. In all graphs the temperature is indicated by colour. As can be seen in Fig. B.3 and Fig. B.4, the LITA extracted volume viscosity rises rapidly with increasing pressure/density.

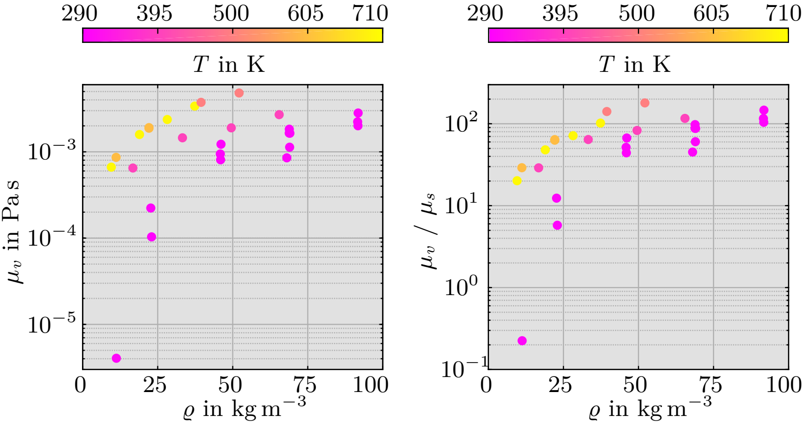

(a) Volume viscosity μ_v.

(b) Viscosity ratio μ_v/μ_s.

Figure B.4: Volume viscosity μ_v and viscosity ratio μ_v/μ_s over density ϱ for N_2. Values are calculated with equation (2.16) with extracted acoustic damping rates Γ_{LITA}. Thermodynamic data are taken from Lemmon et al. [56].